

AD-775 401

STUDY OF PHASE EQUILIBRIA IN THE SYSTEMS  
Tl-As-S and Tl-As-Se

G. W. Roland, et al

Westinghouse Research Laboratories

Prepared for:

Air Force Materials Laboratory  
Advanced Research Projects Agency

31 December 1973

DISTRIBUTED BY:

**NTIS**

National Technical Information Service  
U. S. DEPARTMENT OF COMMERCE  
5285 Port Royal Road, Springfield Va. 22151

REPORT DOCUMENTATION PAGE		READ INSTRUCTIONS BEFORE COMPLETING FORM
1. REPORT NUMBER AFML-TR-74-6	2. GOVT ACCESSION NO.	3. RECIPIENT'S CATALOG NUMBER AD 775 401
4. TITLE (and Subtitle) Study of Phase Equilibria in the Systems Tl-As-S and Tl-As-Se.		5. TYPE OF REPORT & PERIOD COVERED Final Technical Report 1 July 72 - 31 December 73
7. AUTHOR(s) G.W. Roland, J.F. Feichtner, J.P. McHugh		6. PERFORMING ORG. REPORT NUMBER
9. PERFORMING ORGANIZATION NAME AND ADDRESS Westinghouse Electric Corporation Research Laboratories Pittsburgh, PA 15235		8. CONTRACT OR GRANT NUMBER(s) F33615-72-C-1976
11. CONTROLLING OFFICE NAME AND ADDRESS Advanced Research Projects Agency 1400 Wilson Blvd Arlington, VA 22209		10. PROGRAM ELEMENT, PROJECT, TASK AREA & WORK UNIT NUMBERS PE 61101E ARPA Order 2071 WU# 20710CG1
14. MONITORING AGENCY NAME & ADDRESS (if different from Controlling Office) Air Force Materials Laboratory Air Force Systems Command Wright-Patterson AFB, OH 45433		12. REPORT DATE 31 December 1972
		13. NUMBER OF PAGES 110
		15. SECURITY CLASS. (of this report) UNCLASSIFIED
		15a. DECLASSIFICATION/DOWNGRADING SCHEDULE
16. DISTRIBUTION STATEMENT (of this Report)  Approved for Public Release; Distribution Unlimited.		
17. DISTRIBUTION STATEMENT (of the abstract entered in Block 20, if different from Report)		
18. SUPPLEMENTARY NOTES  Reproduced by NATIONAL TECHNICAL INFORMATION SERVICE U.S. Department of Commerce Springfield, VA 22151		
19. KEY WORDS (Continue on reverse side if necessary and identify by block number) Sulfosalts; Tl-As-S; Tl-As-Se; nonlinear optical materials; acousto-optical materials; phase equilibria; crystal growth, $Tl_3AsSe_3$ ; $Tl_3AsS_3$ ; $Tl_3AsS_4$ .		
20. ABSTRACT (Continue on reverse side if necessary and identify by block number) A phase diagram study was conducted to determine the melting relations in portions of the chemical systems Tl-As-S and Tl-As-Se. Particular attention was paid to composition joins such as $Tl_2S-As_2S_3$ , $Tl_2S-As_2S_5$ , $Tl_2Se-As_2Se_3$ and $Tl_2Se-As_2Se_5$ , joins which include the ternary compounds $Tl_3AsS_3$ , $Tl_3AsS_4$ , $Tl_3AsSe_3$ , and $Tl_3AsSe_4$ . These compounds melt congruently and are involved in pseudobinary phase relations along the above joins. The phase diagram data were used to develop optimized crystal-growth continued on reverse side 112		

UNCLASSIFIED

SECURITY CLASSIFICATION OF THIS PAGE (When Data Entered)

CONTINUATION OF BLOCK 20.

compositions for the important ternary compounds. Crystal quality of  $Tl_3AsSe_3$  and  $Tl_3AsS_4$  was significantly improved during the contract period and crystals of  $Tl_3AsS_3$  and  $Tl_3AsSe_4$  grown for the first time. Observed features of the crystal growth were explained in terms of the observed phase relations.

Optical and Acousto-optical properties were determined for  $Tl_3AsS_3$ ,  $Tl_3AsSe_3$ ,  $Tl_3AsS_4$ , and  $Tl_3AsSe_4$ , and it is shown that these compounds have considerable potential as elements in optical and acousto-optical devices.

11

UNCLASSIFIED

SECURITY CLASSIFICATION OF THIS PAGE (When Data Entered)

## TABLE OF CONTENTS

Section	Page
1. INTRODUCTION . . . . .	9
1.1 Objective . . . . .	9
1.2 Background Information . . . . .	9
1.3 General Approach . . . . .	14
1.4 Summary . . . . .	14
2. TECHNIQUES OF PHASE DIAGRAM STUDY AND CRYSTAL GROWTH . . . .	16
2.1 Techniques of Phase Diagram Study . . . . .	16
2.1.1 Quench Experiments . . . . .	16
2.1.2 Thermal Analysis Experiments . . . . .	17
2.2 Crystal Growth Techniques . . . . .	20
3. COMPOSITION AND CRYSTAL DATA FOR COMPOUNDS IN THE SYSTEMS Tl-As-Se and Tl-As-S . . . . .	24
3.1 Composition of Ternary Compounds . . . . .	24
3.2 Crystallographic Data . . . . .	26
3.2.1 $Tl_3AsSe_3$ . . . . .	26
3.2.2 $Tl_3AsS_3$ . . . . .	27
3.2.3 $Tl_3AsS_4$ . . . . .	28
3.2.4 $Tl_3AsSe_4$ . . . . .	28
3.2.5 $TlAsS_2$ and $TlAsSe_2$ . . . . .	29

Section	TABLE OF CONTENTS (continued)	Page
3.2.6	Phase A (unknown Tl-As-S phase) . . . . .	29
3.2.7	$\text{Tl}_4\text{As}_5\text{S}_5$ and $\text{Tl}_6\text{As}_4\text{S}_9$ . . . . .	31
4.	PHASE RELATIONS IN THE SYSTEMS Tl-As-Se AND Tl-As-S . . . .	33
4.1	Data in the Literature . . . . .	33
4.2	Phase Relations Determined in This Study . . . . .	35
4.2.1	Introduction . . . . .	35
4.2.2	The Join $\text{Tl}_2\text{Se}-\text{As}_2\text{Se}_3$ . . . . .	35
4.2.3	The $\text{Tl}_2\text{S}-\text{As}_2\text{S}_3$ Join . . . . .	40
4.2.4	The $\text{Tl}_2\text{S}-\text{As}_2\text{S}_5$ Join . . . . .	42
4.2.5	The $\text{Tl}_3\text{AsS}_3-\text{S}$ Join . . . . .	45
4.2.6	The $\text{Tl}_2\text{Se}-\text{As}_2\text{Se}_5$ and $\text{Tl}_3\text{AsSe}_3-\text{Tl}_3\text{AsSe}_4$ Joins .	46
4.2.7	Ternary Phase Relations . . . . .	47
5.	CRYSTAL GROWTH . . . . .	50
5.1	Introduction . . . . .	50
5.2	Crystal-Quality Evaluation . . . . .	50
5.3	Crystal Growth . . . . .	53
5.3.1	$\text{Tl}_3\text{AsSe}_3$ . . . . .	53
5.3.2	$\text{Tl}_3\text{AsS}_4$ . . . . .	57
5.3.3	$\text{Tl}_3\text{AsS}_3$ . . . . .	60
5.3.4	$\text{Tl}_3\text{AsSe}_4$ . . . . .	62
5.3.5	$\text{TlAsS}_2$ . . . . .	62
5.3.6	$\text{TlAsSe}_2$ . . . . .	63
5.3.7	$\text{Tl}_3\text{As}(\text{S},\text{Se})_3$ . . . . .	63

Section	TABLE OF CONTENTS (continued)	Page
6.	OPTICAL PROPERTIES OF Tl-As-S-Se COMPOUNDS . . . . .	64
6.1	$\text{Tl}_3\text{AsSe}_3$ . . . . .	64
6.2	$\text{Tl}_3\text{AsSe}_4$ . . . . .	69
6.3	$\text{Tl}_3\text{AsS}_3$ . . . . .	69
6.4	$\text{TlAsS}_2$ . . . . .	72
6.5	$\text{Tl}_3\text{AsS}_4$ . . . . .	72
7.	PIEZOELECTRIC, ACOUSTIC, AND ACOUSTO-OPTIC PROPERTIES . . .	74
7.1	$\text{Tl}_3\text{AsSe}_3$ . . . . .	74
7.2	$\text{Tl}_3\text{AsS}_3$ . . . . .	79
7.3	$\text{Tl}_3\text{AsS}_4$ . . . . .	80
8.	USEFULNESS OF Tl-As-S-Se COMPOUNDS IN OPTICAL AND ACOUSTO-OPTICAL DEVICES . . . . .	81
8.1	Introduction . . . . .	81
8.2	Optical Parametric Oscillation . . . . .	81
8.2.1	Desirability of a 2 $\mu\text{m}$ -Pumped Optical Parametric Oscillator System . . . . .	81
8.2.2	Comparison of Materials for 2 $\mu\text{m}$ -Pumped OPO Action; Advantages of $\text{Tl}_3\text{AsSe}_3$ . . . . .	83
8.2.2.1	Requirements . . . . .	83
8.2.2.2	Phase Matching Considerations . . . . .	88
(i)	chalcopyrites . . . . .	88
(ii)	CdSe . . . . .	92
(iii)	the sulfosalt materials . . . . .	92
(iv)	$\text{LiIO}_3$ . . . . .	94
8.2.2.3	Summary of Survey Results . . . . .	97

Section	TABLE OF CONTENTS (continued)	Page
8.3	Acousto-Optic Devices . . . . .	97
8.3.1	Acousto-Optic Modulators . . . . .	97
8.3.1.1	External Modulation at 1.06 $\mu\text{m}$ . . . . .	97
8.3.1.2	Internal Modulation and Q-Switching at 1.06 $\mu\text{m}$ . . . . .	99
8.3.2	Electronically Tunable Infrared Acousto-Optic Filters . . . . .	100
9.	CONCLUSIONS . . . . .	104
	REFERENCES . . . . .	105

# LIST OF ILLUSTRATIONS

<u>Figure</u>	<u>Title</u>	<u>Page</u>
1	Furnace arrangement for thermal analysis.	19
2	Furnaces used for crystal growing.	22
3	Phases in the system Tl-As-S.	25
4	Phases in the system Tl-As-Se.	25
5	Breakdown texture (X100) in previously homogeneous Phase A after storing at room temperature for 5 weeks.	30
6	Equilibrium diagram of the $\text{As}_2\text{Se}_3$ - $\text{Tl}_2\text{Se}$ system, according to Dembovskii et al. <sup>9</sup>	33
7	System $\text{Tl}_2\text{S}$ - $\text{As}_2\text{S}_3$ according to Cammeri and Fernandes. <sup>8</sup>	34
8	Phase relations along the join $\text{Tl}_2\text{Se}$ - $\text{As}_2\text{Se}_3$ according to this study.	36
9	Partial phase diagram for the $\text{Tl}_2\text{Se}$ - $\text{As}_2\text{Se}_3$ system. The points represent thermal arrests.	38
10	Partial phase diagram for the system $\text{Tl}_2\text{S}$ - $\text{As}_2\text{S}_3$ .	43
11	The $\text{Tl}_2\text{S}$ - $\text{As}_2\text{S}_3$ join.	44
12	A portion of the $\text{Tl}_3\text{AsS}_3$ -S join. The points represent arrests in thermal analysis experiments.	45
13	The Tl-As-S ternary system. The outlined portion is shown enlarged in Fig. 14.	48
14	Detail of Tl-As-S system in the region of $\text{Tl}_3\text{AsS}_3$ and $\text{Tl}_3\text{AsS}_4$ ; the x's correspond to eutectics on the pseudobinary joins.	49



<u>Figure</u>	LIST OF ILLUSTRATIONS (continued)	<u>Page</u>
15	Schematic diagram of optical quality scanning system for sulfosalt crystals.	52
16	Optical transmission at 2.1 $\mu\text{m}$ along an as-grown boule of $\text{Tl}_3\text{AsSe}_3$ .	54
17	Optical transmission at 2.1 $\mu\text{m}$ along an as-grown boule of $\text{Tl}_3\text{AsSe}_3$ , Crystal TASE-BR-3.	56
18	Optical transmission at 2.1 $\mu\text{m}$ along an as-grown boule of $\text{Tl}_3\text{AsSe}_3$ , Crystal TASE-LR-6.	56
19	The refractive indices of $\text{Tl}_3\text{AsSe}_3$ , Crystal TASE-BR-3.	65
20	Calculated phase match angle vs wavelength of fundamental for Type I phase-matched second harmonic generation in $\text{Tl}_3\text{AsSe}_3$ (Crystal #TASE-BR-3).	67
21	Phase matching curves (Type I) for optical parametric oscillation in $\text{Tl}_3\text{AsSe}_3$ .	68
22	Optical transmission of $\text{Tl}_3\text{AsSe}_4$ .	70
23	Optical transmission at 2.1 $\mu\text{m}$ along an as-grown boule of $\text{Tl}_3\text{AsSe}_3$ .	71
24	Optical transmission vs wavelength for single crystal $\text{Tl}_3\text{AsSe}_3$ . Sample thickness 3.82 mm. Curve uncorrected for reflection losses.	73
25	Optical parametric figure of merit, $d^2/n^3$ , and transparency region for nonlinear optical materials.	85
26	Three-frequency phase matching for $\text{ZnGeP}_2$ indicating $\nu_1$ and $\nu_2$ (or wavelength $\lambda_1$ and $\lambda_2$ ) vs the pump frequency $\nu_3$ (or wavelength $\lambda_3$ ). (Ref. 26)	89
27	Type-I ( $o + o + e$ ) three-frequency phase matching for $\text{AgGaS}_2$ , indicating $\nu_1$ and $\nu_2$ versus pump frequency $\nu_3$ (lower right) or $\lambda_1$ and $\lambda_2$ versus $\lambda_3$ (upper left). (Ref. 23)	89
28	Type-I ( $o + o + e$ ) three-frequency phase matching for $\text{AgGaSe}_2$ , indicating $\nu_1$ and $\nu_2$ versus pump frequency $\nu_3$ (lower right) or $\lambda_1$ and $\lambda_2$ versus $\lambda_3$ (upper left). (Ref. 24)	90

<u>Figure</u>	LIST OF ILLUSTRATIONS (continued)	<u>Page</u>
29	Type-2 ( $e + o + o$ ) three-frequency phase matching for $\text{AgGaSe}_2$ , indicating $\nu_1$ and $\nu_2$ versus pump frequency $\nu_3$ (lower right) and $\lambda_1$ and $\lambda_2$ versus $\lambda_3$ (upper left). (Ref. 24)	91
30	Theoretical tuning curve for optical parametric oscillation in $\text{CdSe}$ , for a pump wavelength $\lambda_p = 2.06 \mu\text{m}$ . (Ref. 27)	93
31	Theoretical tuning curves for optical parametric oscillation in proustite ( $\text{Ag}_3\text{AsS}_3$ ), pump wavelength $\lambda_p$ a parameter. (Ref. 27)	93
32	Theoretical tuning curves for optical parametric oscillation in $\text{LiIO}_3$ , pump wavelength $\lambda_p$ a parameter. (Ref. 27)	93

# LIST OF TABLES

	<u>Page</u>
Table 1 X-Ray Powder Data for $\text{Tl}_3\text{AsSe}_3$ .	27
Table 2 Low Temperature Annealing Experiments.	41
Table 3 Optical Loss Measurements on $\text{Tl}_3\text{AsSe}_3$ Boules.	55
Table 4 Crystal-Growth Experiments Conducted to Determine Optimum Growth Composition for $\text{Tl}_3\text{AsS}_4$ .	59
Table 5 Some Piezoelectric and Elastic Constants for $\text{Tl}_3\text{AsSe}_3$ at Room Temperature.	76
Table 6 Measured Acoustic Properties of $\text{Tl}_3\text{AsSe}_3$ .	77
Table 7 Calculated and Measured Acousto-Optic Figures of Merit, $M_2$ .	78
Table 8 Properties of Candidate Nonlinear Optical Materials for 2.1 $\mu\text{m}$ Pumped Parametric Oscillation in the 4 to 5 $\mu\text{m}$ Region.	96

## 1. INTRODUCTION

### 1.1 Objective

The objective of this program was to determine the phase equilibria in the systems Tl-As-S and Tl-As-Se and a portion of the quaternary system Tl-As-S-Se so as to optimize crystal growth of compounds in these systems, notably  $\text{Tl}_3\text{AsS}_3$ ,  $\text{Tl}_3\text{AsSe}_3$ , and  $\text{Tl}_3\text{AsS}_4$ . These compounds form promising nonlinear optical and acousto-optical crystals. Optical techniques were to be used to evaluate crystal quality and the optical properties of any new compounds encountered were to be investigated to determine their potential as useful optical materials.

### 1.2 Background Information

Increasing interest is being shown in nonlinear optical materials for harmonic generation and up-conversion applications in the infrared region of the spectrum. Sulfide-type materials are of special interest because they have a wide range of transparency and might be expected to transmit in the  $10\text{ }\mu\text{m}$  region where oxides are usually opaque and where high power gas lasers operate. Only a few such materials, notably proustite ( $\text{Ag}_3\text{AsS}_3$ ) and pyrargyrite ( $\text{Ag}_3\text{SbS}_3$ ) were available in good optical quality prior to the start of the present program.

These two materials suffer from residual absorption at 10.6  $\mu\text{m}$ , which causes deleterious heating effects when the high power densities at 10.6  $\mu\text{m}$  necessary for efficient frequency conversion are used. Cinnabar ( $\text{HgS}$ ) has suitably high nonlinear optical coefficients and a wide region of transparency (0.6 to 13  $\mu\text{m}$ ), but is very difficult to grow with good optical quality. Tellurium ( $\text{Te}$ ) and selenium ( $\text{Se}$ ) have been reported as nonlinear optical materials useful at 10.6  $\mu\text{m}$ , but they also have poor optical quality. In addition, tellurium has been reported to exhibit an induced loss in SHG efficiency at 10.6  $\mu\text{m}$  due to photoinduced carriers.

Sulfide-type materials are also of interest for acousto-optic applications. The technique of light deflection by acoustically generated gratings in solids or liquids is now well established, and many microwave and radio-frequency signal-processing devices have been constructed based on the acousto-optic interaction. The deflection efficiency of a material, or amount of light deflected from the incident beam for a given amount of acoustic power in the material is proportional to the so-called "acousto-optic figure of merit,"  $M_2 = \eta^2 p^2 / \rho v^3$ , where  $\eta$  is the refractive index of the material at the wavelength of the incident light,  $p$  is the photoelastic coefficient (which is roughly constant but may increase in regions of strong dispersion),  $\rho$  is the density, and  $v$  the acoustic velocity in the material.

It is evident that high refractive indices and low acoustic velocities are requirements for materials with large acousto-optic

figures of merit. Both are general properties of sulfide-type materials. Additional requirements on the usefulness of a given material are that it be optically transparent at the wavelength of light to be used in the application, and that it exhibit reasonably low acoustic loss at the acoustic frequencies to be used.

Prior to the inception of this contract the Westinghouse Research Laboratories had been actively searching for new sulfide-type materials for use as nonlinear and acousto-optic materials. Our experience in the area of nonlinear chalcogenides was derived from a thorough study<sup>1</sup> of the phase relations and crystal growth of proustite and pyrargyrite. As a result of this survey, we had synthesized several Tl-bearing chalcogenides that seemed promising for both nonlinear and acousto-optic applications. Of particular interest were the compounds  $\text{Tl}_3\text{AsS}_3$ ,  $\text{Tl}_3\text{AsSe}_3$ , and  $\text{Tl}_3\text{AsS}_4$ . These are close crystal-chemical relatives of  $\text{Ag}_3\text{AsS}_3$  and  $\text{Ag}_3\text{SbS}_3$  in that all belong to the sulfosalt class of chalcogenides.

Sulfosalts can be defined as having the general formula



where A represents a metal, usually Ag, Cu, Hg, Pb, Tl, or Zn; B represents As, Bi, or Sb; and C represents S, Se, or Te. The B and C atoms in the general sulfosalt formula  $\text{A}_m \text{B}_n \text{C}_p$  are almost always closely associated in the crystal structures, forming finite groups, rings, chains, or nets of  $\text{BC}_3$  trigonal pyramids or  $\text{BC}_4$  tetrahedra (with or

without additional C ions). Nowacki<sup>2</sup> classified all known sulfosalt minerals according to which of these structural units is present. Perhaps a more convenient (but related) classification is by  $\phi$  number, where

$$\phi = \frac{\text{Number of C atoms}}{\text{Number of B atoms}}$$

For  $\text{Ti}_3\text{AsSe}_3$ ,  $\phi = 3$ ; for  $\text{Ti}_3\text{AsS}_4$ ,  $\phi = 4$ , etc. The  $\phi$  number of a particular sulfosalt compound provides important information as to its crystal structure. For example, compounds with  $\phi = 3$  typically contain isolated  $\text{BC}_3$  tetrahedra as part of their structural makeup. Similarly, a crystal structure analysis will undoubtedly show this to be the case for  $\text{Ti}_3\text{AsS}_3$  and  $\text{Ti}_3\text{AsSe}_3$  as well.

We had obtained sufficient preliminary data on the melting relations of  $\text{Ti}_3\text{AsSe}_3$  and  $\text{Ti}_3\text{AsS}_4$  to show that both melted congruently, and crystals were grown using the techniques applied previously to  $\text{Ag}_3\text{AsS}_3$ . It was immediately evident that both were useful optical materials.

$\text{Ti}_3\text{AsSe}_3$  had several advantages. It had the expected wide transmission range (1.5 to 15  $\mu\text{m}$ ) and, moreover, had decreased absorption loss relative to proustite and pyrargyrite. The refractive indices were high, indicating a high figure of merit for nonlinear applications, and the birefringence was such as to allow phase matching for second-harmonic generation at 10.6  $\mu\text{m}$ . It appeared that, in addition to second-harmonic generation,  $\text{Ti}_3\text{AsSe}_3$  would also be useful

as a parametric oscillator pumped at wavelengths from 1.25 to beyond 10  $\mu\text{m}$ , and especially useful as a material for a 2  $\mu\text{m}$  pumped oscillator operating with outputs in the 3 to 5  $\mu\text{m}$  region.

Both  $\text{Tl}_3\text{AsSe}_3$  and  $\text{Tl}_3\text{AsS}_4$  were shown to be useful acousto-optic crystals. The acousto-optic figure of merit was measured, by direct comparison, for  $\text{Tl}_3\text{AsSe}_3$  at  $\lambda = 3.39 \mu\text{m}$ , relative to fused silica at  $\lambda = 0.6328 \mu\text{m}$ . The relative figure of merit was measured as 955. This figure of merit is about twice as large as the figure of merit for germanium, the material presently being used in acousto-optic devices in the infrared region of the spectrum. Likewise, measurements of the figure of merit for  $\text{Tl}_3\text{AsS}_4$  gave exceptionally high values at 0.6328  $\mu\text{m}$ , higher than any other known material.

It was also evident, however, that the crystal growth of these new materials would be difficult to optimize without a thorough knowledge of the melting relations in the applicable chemical systems. Only meager information was available for the ternary systems; in fact, many uncertainties and inconsistencies existed in the reported phase relations for the basic binary systems  $\text{Tl-S}$  and  $\text{Tl-Se}$ .

Our initial crystal growth efforts showed that the ideal chemical compositions were not the ideal growth compositions -- the crystals almost invariably contained second-phase inclusions and/or cracked excessively. The program to study the phase diagrams for the systems  $\text{Tl-As-S}$  and  $\text{Tl-As-Se}$  was undertaken to understand and optimize the crystal growth of these  $\text{Tl}$ -containing sulfosalts.



### 1.3 General Approach

The approach adopted in the present program was as follows. Approximately two thirds of the study was devoted to determining the melting relations of the important ternary compounds in the Tl-As-S and Tl-As-Se chemical systems. Particular attention was devoted to the detailed melting relations around the compounds  $\text{Tl}_3\text{AsS}_3$ ,  $\text{Tl}_3\text{AsSe}_3$ , and  $\text{Tl}_3\text{AsS}_4$ . These phase relations were determined both by quenching experiments and by thermal heating and cooling curves. The data from the phase diagram study were then used to understand and optimize the crystal growth of the useful ternary compounds. Techniques for the passive and active evaluation of crystal quality were developed and applied to the optical-quality determination of the newly-grown crystals. Significant improvement in crystal quality was demonstrated and the improved crystals were measured to determine their device properties.

### 1.4 Summary

As a result of this program, we now have available extensive knowledge of melting relations in the systems Tl-As-S and Tl-As-Se. Optimized growth compositions were determined for  $\text{Tl}_3\text{AsSe}_3$  and  $\text{Tl}_3\text{AsS}_4$  and crystals of improved optical quality were grown. Optical measurements were performed that demonstrate the device potential of these compounds. Crystals of  $\text{Tl}_3\text{AsS}_3$  and  $\text{Tl}_3\text{AsSe}_3$  were obtained showing considerable improvement over early growth efforts; we were not, however, able to obtain high quality crystals of  $\text{Tl}_3\text{AsS}_3$ . This is

explained on the basis of the determined phase diagrams. In the broader sense, data obtained in this study provide insight into the phase chemistry and crystal chemistry of this type of compound in general, information that should prove valuable in devising methods of approach leading to a thorough understanding of other potentially useful chemical systems.

## 2. TECHNIQUES OF PHASE DIAGRAM STUDY AND CRYSTAL GROWTH

### 2.1 Techniques of Phase Diagram Study

Two techniques have been used for phase diagram study:

(1) quench-type or silica-tube experiments and (2) thermal analysis experiments. Both types of experiments are conducted in sealed, initially-evacuated, silica glass containers, which are well-suited for reactions among sulfide-type compounds because they are inert and because they constitute sealed containers for the volatile components such as sulfur and selenium.

Spectrographically analyzed Tl, As, S, and Se (each > 99.999 wt % purity) were used directly as reactants for both quench and thermal analysis experiments. The oxide coating that forms on Tl and As was removed by boiling the Tl in water and heating the As fragments in the reducing portion of a Bunsen-burner flame.

#### 2.1.1 Quench Experiments

For quench-type experiments, reactant materials (typically 200 mg total weight) were carefully weighed in desired proportions, sealed in the containers, heated for lengths of time necessary to obtain equilibrium phase assemblages, and then chilled to room temperature. Phases were identified using standard microscope and x-ray techniques.

Some degree of experience is necessary to identify the stable phase assemblages at the heating temperatures by examination of the quenched products. For example, the presence of liquid in an experiment was indicated by the globular appearance of the charge after heating and by texture relations in polished specimens. Liquids generally crystallized during the quench to polyphase masses in which the individual phases (often displaying dendritic habit) could only be identified using high-magnification microscope lenses. The rate of quench-crystallization of liquids to such intergrowths decreases toward the As-S or As-Se side of both systems and, in the  $\text{As}_2\text{S}_3$ -rich or  $\text{As}_2\text{Se}_3$ -rich portions, liquids could be chilled as glasses.

Many of the data presented below were obtained from melting point experiments. In a typical melting point determination, a portion of presynthesized compound (e.g.,  $\text{Tl}_3\text{AsSe}_3$ ) or a mixture of compounds (e.g.,  $\text{Tl}_2\text{Se} + \text{Tl}_3\text{AsSe}_3$ ) was heated at successively higher temperatures until melting occurred. The run was maintained above the melting point for up to 8 hours then quenched and the charge examined to determine the stable phase assemblage at the final annealing temperature.

### 2.1.2 Thermal Analysis Experiments

The experimental system used for obtaining cooling curves consists of a Marshall furnace mounted vertically, a temperature control system, and a L&N AZAR strip chart recorder which produces a direct plot of sample temperature as a function of time (the cooling curve). The recorder is calibrated to record the desired temperature

interval by means of a L&N K-3 potentiometer. The recorder is normally set to record over a temperature interval of about 100°C. A calibrate-record selector switch permits rapid recalibration to the next desired temperature interval so that data may be recorded over as wide a temperature range as desired. The furnace control system is equipped with a motor drive, so that the cooling rate may be controlled. However, the temperatures involved in these systems are sufficiently low that satisfactory cooling rates are obtained by simply turning off the heavily insulated furnace and letting it cool at its natural rate.

The quartz sample containers include a thermocouple well which permits the chromel-alumel thermocouple bead to be positioned so that it is surrounded by the sample, but isolated from it. The furnace and sample arrangement is shown in Fig. 1.

A typical run proceeds as follows. The sample tubes are first cleaned by lightly etching with diluted (50-50) hydrofluoric acid. After thorough rinsing, the tubes are baked at 800°C. The inside surfaces of the tubes are then coated with carbon by the pyrolysis of acetone. These preparatory operations are carried out on the sample tubes in order to prevent tube cracking during the melting and freezing reactions which the samples undergo during the thermal cycle. This tube cracking problem did not arise in the case of the selenium compositions, but uncoated tubes used with the sulfur compositions frequently cracked when the charges crystallized. Since the adoption of the carbon coating procedure, however, tube cracking has ceased to be a problem.

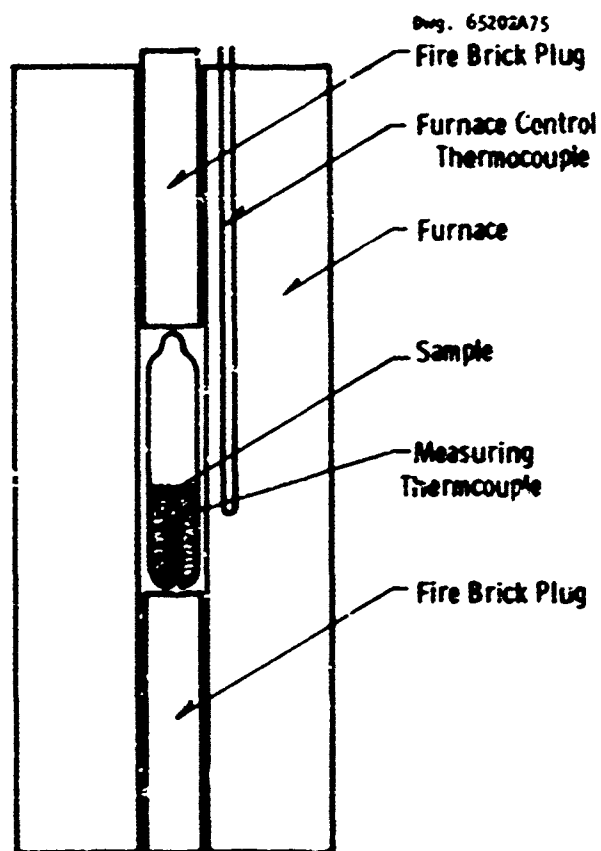


Figure 1 -- Furnace arrangement for thermal analysis.

The required amounts of 99.999<sup>+</sup>% pure elements (from ASARCO) are weighed and loaded into the sample tubes, which are then evacuated and sealed off. The sample tube is placed horizontally in a cold split furnace and the temperature raised over a period of several hours to 750-800°C. The sample is shaken several times, and soaked at the high temperature overnight to insure homogenization. The furnace power is then cut and the sample allowed to cool in the furnace.

A chromel-alumel thermocouple is positioned in the thermocouple well, and the leads passed along the sample tube and tied to the ampoule with nichrome wire. The sample is placed in the furnace as shown in Fig. 1, with the thermocouple leads passing through a groove in the upper plug and out the top of the furnace. The thermocouple cold junction is placed in an ice bath.

The sample is then heated to a temperature at least 50°C above the estimated liquidus temperature, then allowed to cool while recording sample temperature as a function of time (the cooling curve).

The sample may be reheated and cooled several times in order to verify the location (temperature) and shape of thermal arrests. Sample temperature is recorded continuously as a function of time so that heating as well as cooling data are obtained.

## 2.2 Crystal Growth Techniques

Our experience has shown that the essential features of a crystal-growth technique for congruently-melting sulfosalt materials are: (1) carefully prepared reactant material that precisely matches the congruently-melting composition of the desired crystal, (2) a slow growth rate (10 to 20 mm/day), and (3) a steep (5 to 15°C/mm) temperature gradient at the solid-liquid interface in the crystal growing furnace. Growth facilities were optimized to provide the necessary steep temperature profiles and slow growth rates.

Reactant material for crystal growth is prepared directly from the de-oxidized high-purity elements Tl, As, S, and Se. These

are weighed in desired proportions and sealed under vacuum in a quartz ampoule. Typically, a reactant charge weighs 50 grams. The elemental mixture is heated at a low temperature (200 to 400°C) to react the most volatile component (S or Se) with the metallic elements -- a reaction step that is taken to minimize the vapor pressure in the tubes at elevated temperatures. The charge is then heated to 700 to 800°C; the liquid is mixed by vigorously shaking the quartz container several times, and the liquid is allowed to crystallize slowly by shutting off power to the furnace. After opening the tube, the crystalline reactant is stored at room temperature in a vacuum desiccator.

For crystal growth, portions of the prepared reactant are sealed under about 0.8 atm pressure of pure argon into quartz "crystal-growing" tubes which contain a necked-in portion near the bottom of the tube. The neck in the tube serves exactly the same purpose as a neck in a Czochralski crystal -- to initiate single-crystal growth from a polycrystalline boule. The argon pressure in the tubes suppresses the presence of vapor during a growth run.

Figure 2 shows the quartz-tube furnaces used for crystal growth. Each furnace consists of two heated zones separately controlled by variacs: an upper high-temperature zone and a lower low-temperature zone. The temperature gradient at the solid-liquid interface can be varied by adjusting the voltages to the two windings. As the crystal-growth tubes containing melt drop slowly through the furnace, the melts



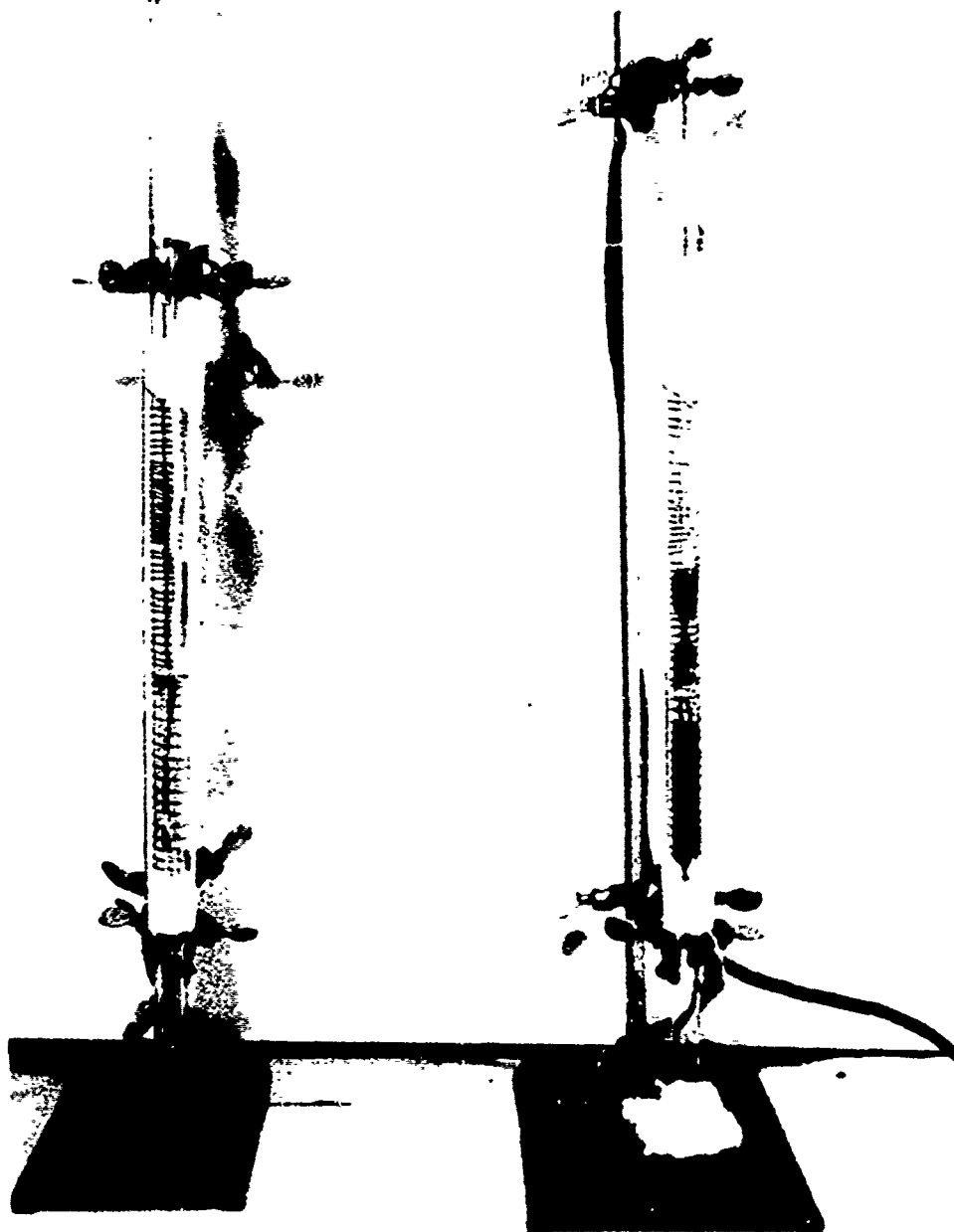


Figure 2 -- Furnaces used for crystal growing.

crystallize when the temperature reaches that of the solidification (melting) point. The grown crystal is allowed to anneal at the temperature of the lower furnace (usually set at about half the melting temperature) and then cooled to room temperature over two to three days.

### 3. COMPOSITION AND CRYSTAL DATA FOR COMPOUNDS IN THE SYSTEMS Tl-As-Se AND Tl-As-S

#### 3.1 Composition of Ternary Compounds

The compositions of known compounds in the systems Tl-As-S and Tl-As-Se can best be described in terms of the three-component diagram for each system (Figs. 3 and 4). On each diagram are plotted the compositions of the known binary compounds and the compositions of the ternary compounds known from this study. The following points are germane to this discussion:

- There are several binary Tl-S and Tl-Se phases<sup>3-5</sup> whose exact compositions and phase relations are not precisely defined. Except for  $\text{Tl}_2\text{S}$  and  $\text{Tl}_2\text{Se}$ , they do not appear to be involved in the liquidus relations of the important ternary compounds (this point is further discussed in the description of the ternary phase relations). No further data were derived from the present study to clarify the binary phase diagrams.
- The ternary compounds lie on composition joins from  $\text{Tl}_2\text{S}$  to  $\text{As}_2\text{S}_3$  and  $\text{As}_2\text{S}_5$ , and from  $\text{Tl}_2\text{Se}$  to  $\text{As}_2\text{Se}_3$  and  $\text{As}_2\text{Se}_5$ . This feature is characteristic of many related systems such as Ag-As-S in which such joins are often pseudobinary.

Three additional ternary phases were studied which are not shown on Figs. 3 and 4. These are the phases  $\text{Tl}_4\text{As}_2\text{S}_5$  and  $\text{Tl}_6\text{As}_4\text{S}_9$

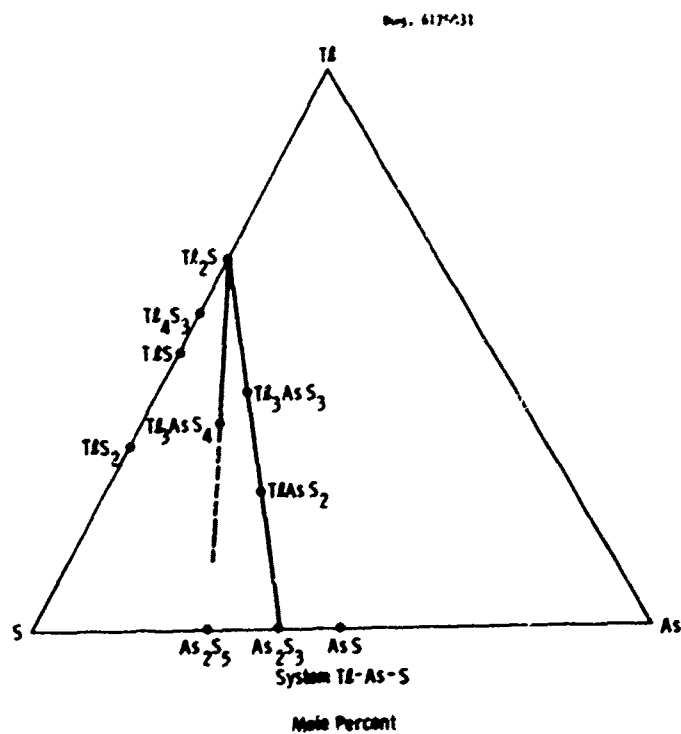


Figure 3 — Phases in the system Tl-As-S.

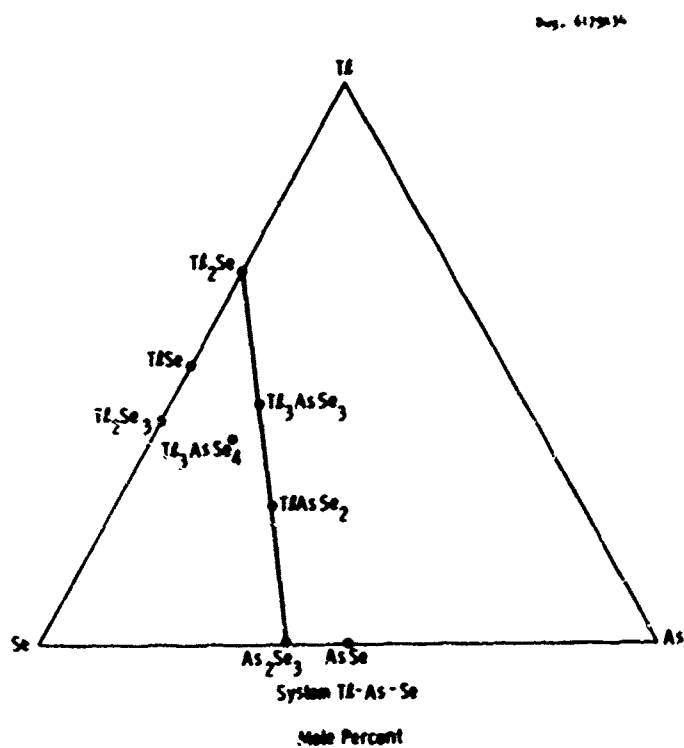


Figure 4 — Phases in the system Tl-As-Se.

previously reported in the literature (and which we could not verify), and a previously unrecognized phase (Phase A) which we believe to be metastable. These phases are discussed in the following section, Crystallographic Data.

### 3.2 Crystallographic Data

Samples of the ternary compounds have been examined by x-ray powder diffraction methods and small single crystals of  $\text{Ti}_3\text{AsSe}_3$  and  $\text{Ti}_3\text{AsS}_4$  have been studied in detail with a Buerger precession camera. The latter technique provides a relatively rapid means of determining crystal symmetry (diffraction aspect) and cell dimensions. The available crystallographic data are described in the following sections.

#### 3.2.1 $\text{Ti}_3\text{AsSe}_3$

The single crystal study of this material indicates that it belongs to Laue Class  $\bar{3}2/m$ . The diffraction aspect is  $R^{**}$  so that the crystal system is hexagonal (rhombohedral). Our observations show that  $\text{Ti}_3\text{AsSe}_3$  is strongly piezoelectric (indicating an acentric structure), and the space group must be either  $R32$  or  $R3m$ . Optical activity was not detected, and crystal class  $3m$  is therefore indicated, i.e., the space group is  $R3m$ . The measured cell dimensions are  $a = 9.90 \text{ \AA}$  and  $c = 7.13 \text{ \AA}$ . Indexed powder diffraction data are reported in Table 1. The measured density is 7.83 grams/cc, which gives a cell content of  $\text{Ti}_9\text{As}_3\text{Se}_9$  ( $D_{\text{calc.}} = 7.82 \text{ grams/cc}$ ).

$\text{Ti}_3\text{AsSe}_3$  has rhombohedral cleavage.

TABLE 1. X-Ray Powder Data for  $\text{Tl}_3\text{AsSe}_3$ 

Indexed for $a = 9.80 \text{ \AA}$ , $c = 7.08 \text{ \AA}$			
$d_{\text{obs}}$ ( $\text{\AA}$ )	$I/I_0$ (estimated)	$d_{\text{calc}}$ ( $\text{\AA}$ )	hk·l
3.63	0.3	3.64	13.1
3.25	0.8	3.23	20.2
2.93	0.2	2.93	33.0
2.83	0.4	2.80	05.1
2.72	1.0	2.73	31.2
2.45	0.1	2.44	25.0
2.38	0.4	2.38	00.3
2.36	0.3	2.36	43.1
1.96	0.1	1.95	61.2

Pattern limited to  $d \geq 1.82 \text{ \AA}$ .

### 3.2.2 $\text{Tl}_3\text{AsS}_3$

The x-ray powder data for  $\text{Tl}_3\text{AsS}_3$  show sufficient similarity to those for  $\text{Tl}_3\text{AsSe}_3$  reported in Table 1 so as to indicate that the two are isostructural. The cell dimensions, although not precisely measured, are slightly less than those for  $\text{Tl}_3\text{AsSe}_3$ , as is to be expected from the relative ionic sizes of  $\text{S}^{2-}$  and  $\text{Se}^{2-}$ . We have not, however, been able to obtain a small perfect crystal for single-crystal investigation; every crystal we have investigated has given streaked and/or multiple diffraction spots indicating polycrystallinity.

or strain. Likewise, Laue photographs of a grown boule indicated very imperfect crystalline quality. We conclude that the two compounds are probably isostructural but the necessary proof from single-crystal x-ray photographs is not available.

### 3.2.3 $\text{Tl}_3\text{AsS}_4$

Single crystal x-ray studies of  $\text{Tl}_3\text{AsS}_4$  were undertaken using the Buerger camera.  $\text{Tl}_3\text{AsS}_4$  is orthorhombic with cell dimensions of  $a = 8.98 \text{ \AA}$ ,  $b = 10.8 \text{ \AA}$ , and  $c = 8.86 \text{ \AA}$ . The systematic absence of reflections define the diffraction aspect as  $\underline{P} \underline{c} * \underline{n} \underline{3c}$  that the space group is either  $\underline{P} \underline{c} \underline{m} \underline{n}$  (centric, class  $\underline{m} \underline{m} \underline{m}$ ) or  $\underline{P} \underline{c} \underline{2} \underline{n}$  (acentric, class  $\underline{m} \underline{2} \underline{m}$ ). In the non-centric space group  $\underline{P} \underline{c} \underline{2} \underline{n}$ , the  $b$  axis would be the unique or polar axis. Tests for piezoelectricity were negative, and second-harmonic generation at  $10.6 \text{ \mu m}$  was not observed in a single crystal specimen oriented on the phase-matching direction for  $10.6 \text{ \mu m}$  radiation. These negative tests indicate the centric space group  $\underline{P} \underline{c} \underline{m} \underline{n}$ . The measured density is  $6.20 \pm 0.04 \text{ grams/cm}^3$ , which gives a cell content of  $4(\text{Tl}_3\text{AsS}_4)$ .

### 3.2.4 $\text{Tl}_3\text{AsSe}_4$

X-ray powder diffraction data indicate that  $\text{Tl}_3\text{AsSe}_4$  is isostructural with  $\text{Tl}_3\text{AsS}_4$ , i.e., this compound has a centric orthorhombic crystal structure. Unfortunately, large single crystals of this material were obtained late in the program, and no single-crystal x-ray precession photographs were taken. Study of this material will be continued during the coming year.

### 3.2.5 $\text{TlAsS}_2$ and $\text{TlAsSe}_2$

The compound  $\text{TlAsS}_2$  is well known as the monoclinic mineral lorandite<sup>6</sup>. Its space group is either  $\underline{P2}_1/\underline{x}$  or  $\underline{P2}_1/\underline{x}$  and the cell parameters are  $\underline{a} = 12.25$ ,  $\underline{b} = 11.32$ ,  $\underline{c} = 6.10 \text{ \AA}$ ,  $\beta = 104^\circ 12'$ . The compound  $\text{TlAsSe}_2$  is not known naturally; the x-ray powder data are quite similar to those of  $\text{TlAsS}_2$  so that there is little doubt that this compound too is one of low symmetry. Several crystal growth attempts for  $\text{TlAsS}_2$  and  $\text{TlAsSe}_2$  (see Sec. 5.3.5 and 5.3.6) were not successful, and no further attention was devoted to their crystallography since their low symmetry would make them doubtful candidates for useful optical applications.

### 3.2.6 Phase A (unknown Tl-As-S Phase)

A previously unknown Tl-As-S phase was obtained in melts of composition  $\text{Tl}_3\text{AsS}_3 + 1 \text{ mol } \% \text{As}_2\text{S}_3$  crystallized by slowly cooling the charge to room temperature. These melts crystallized to a mass of crystals showing bladed habit. Small crystals were separated for microscope examination -- they are birefringent in both transmitted and reflected light and transmit in the red portion of the visible spectrum. They have parallel extinction and at least two excellent cleavages -- one parallel and one normal the length of the crystals. The x-ray pattern is complex and quite unlike the patterns of the other phases in the system. Our observations concerning the composition and stability of this phase (Phase A) are summarized below:



- 1) Phase A has only been identified in runs containing 26 mol %  $\text{As}_2\text{S}_3$  ( $\text{Tl}_3\text{AsS}_3 + 1$  mol %  $\text{As}_2\text{S}_3$ ). Runs containing 30 and 33.3 mol % ( $\text{Tl}_3\text{AsS}_3 + 5$  and 8.3 mol %) showed  $\text{Tl}_3\text{AsS}_3$  as the primary phase to crystallize.
- 2) We have never obtained pure Phase A — always there is some second phase present.
- 3) Phase A was never obtained at  $\text{Tl}_3\text{AsS}_3$  composition, either when  $\text{Tl}_3\text{AsS}_3$  melts are slowly cooled or when such melts were rapidly chilled in ice water.
- 4) A crystal growth run prepared with a reactant containing 26 mol %  $\text{As}_2\text{S}_3$  resulted in a polycrystalline boule of  $\text{Tl}_3\text{AsS}_3$ .
- 5) Phase A appears to be unstable at room temperature because we observed a distinct breakdown texture (Fig. 5) forming in samples

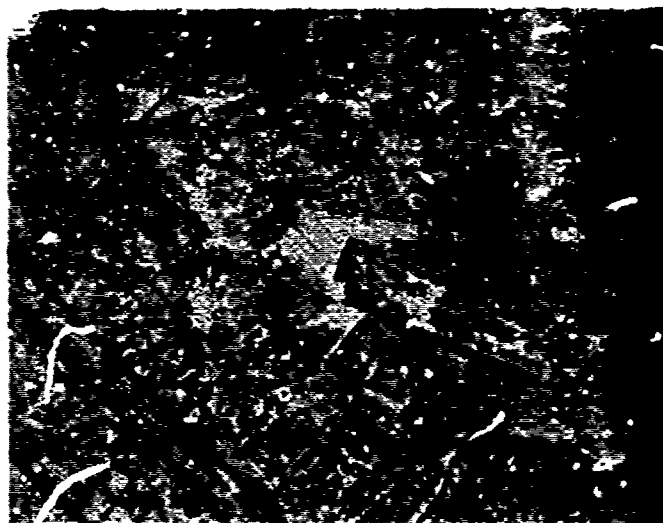


Fig. 5 -- Breakdown texture (X100) in previously-homogeneous Phase A after storing at room temperature for 5 weeks.

kept at room temperature for a few weeks. X-ray powder patterns are different than for the original material but still complex.

- 6) Portions of previously-synthesized Phase A heated at 240°C, 275°C, and 298°C quickly (4 hours) decomposed to  $Tl_3AsS_3$ .
- 7) There was no evidence for the existence of such a compound in any of our thermal analysis experiments.

We believe that our observations on Phase A are consistent with a hypothesis that this compound is a metastable phase which forms only within a very restricted temperature and compositional range; its occurrence probably also depends on the preparation technique. Metastable phases of this type are relatively common in sulfide systems, e.g. in the system Cu-Sb-S.<sup>7</sup>

We separated several small (sub-millimeter) crystals to determine the crystal symmetry by single-crystal x-ray studies. All the fragments examined, however, showed severe distortion and cracking, probably caused by the unstable nature of Phase A at room temperature.

### 3.2.7 $Tl_4As_2S_5$ and $Tl_6As_4S_9$

Attempts were made to synthesize the compounds  $Tl_4As_2S_5$  and  $Tl_6As_4S_9$  reported by Canneri and Fernandes<sup>8</sup>. For  $Tl_4As_2S_5$ , a melt of  $Tl_4As_2S_5$  composition was prepared by heating the required mixture of elements at 700°C for about 16 hours. The charge was cooled to room temperature and examined by x-ray and microscope polished section -- the charge was polyphase, with  $Tl_3AsS_3$  being the primary phase to

crystallize as demonstrated by its dendritic habit. Portions of this charge were heated at successively higher temperatures until melting occurred. Initial melting was observed in two separate runs at 228-232° and 228-233° which corresponds to the  $231 \pm 3^\circ\text{C}$  temperature we find for the eutectic temperature between  $\text{TlAsS}_2$  and  $\text{Tl}_3\text{AsS}_3$  (See Sec. 4.2.3). Similar results were obtained for  $\text{Tl}_6\text{As}_4\text{S}_9$ , whose reported composition is very nearly that of the  $\text{Tl}_3\text{AsS}_3$ - $\text{TlAsS}_2$  eutectic composition.

#### 4. PHASE RELATIONS IN THE SYSTEMS $\text{Tl-As-Se}$ AND $\text{Tl-As-S}$

##### 4.3 Data in the Literature

A pseudobinary phase diagram for the system  $\text{Tl}_2\text{Se-As}_2\text{Se}_3$  was reported by Dembovskii, Kirilenko, and Khvorostenko<sup>9</sup>. Their diagram, reproduced in Fig. 6, shows only two intermediate compounds,

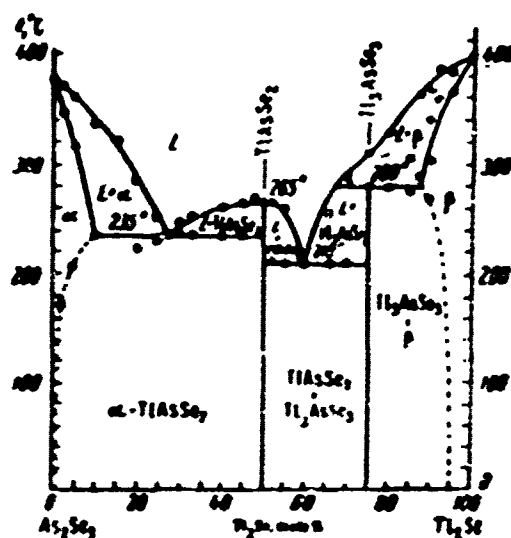


Fig. 6 — Equilibrium diagram of the  $\text{As}_2\text{Se}_3\text{-Tl}_2\text{Se}$  system, according to Dembovskii et al.<sup>9</sup>

$\text{Tl}_3\text{AsSe}_3$  and  $\text{TlAsSe}_2$ , between the two components. Their diagram is quite similar to the diagram we report below in Sec. 4.2 except for one notable discrepancy — the compound  $\text{Tl}_3\text{AsSe}_3$  is shown to melt

incongruently at 280°C whereas we find congruent melting at 311°C. The diagrams are compared and the discrepancies discussed in the next section.

A previous diagram for the system  $\text{Tl}_2\text{S}-\text{As}_2\text{S}_3$  reported by Canneri and Fernandes<sup>8</sup> bears little resemblance to that reported here. According to their diagram (Fig. 7), there are four pseudobinary phases:  $\text{Tl}_3\text{AsS}_3$ ,  $\text{Tl}_4\text{As}_2\text{S}_5$  (mistakenly shown as  $\text{Tl}_4\text{As}_2\text{S}_3$ ),  $\text{Tl}_5\text{As}_4\text{S}_9$ , and  $\text{TlAsS}_2$ . Of these, we find only  $\text{Tl}_3\text{AsS}_3$  and  $\text{TlAsS}_2$  to be stable

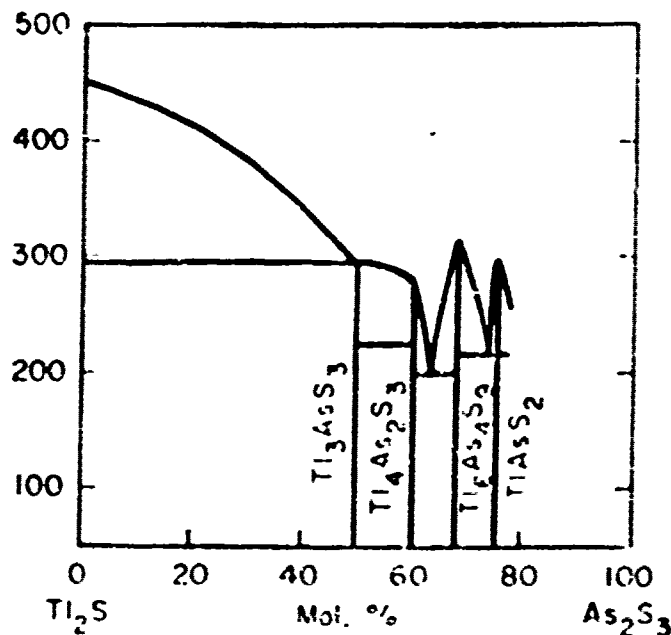


Fig. 7 -- System  $\text{Tl}_2\text{S}-\text{As}_2\text{S}_3$  according to Canneri and Fernandes.<sup>8</sup>

phases in this system (see Sec. 3.2.7). The phase diagram by Canneri and Fernandes is based solely on thermal arrest experiments;

we find that thermal data are notably unreliable in the  $\text{As}_2\text{S}_3$ -rich portion of the  $\text{Tl}_2\text{S}-\text{As}_2\text{S}_3$  system because of supercooling and metastability phenomenon. Such problems, as well as the impure reactant materials used by Canneri and Fernandes, probably account for the errors in their diagram.

#### 4.2 Phase Relations Determined in this Study

##### 4.2.1 Introduction

As noted in Sec. 3.1, the important ternary compounds in the systems  $\text{Tl}-\text{As}-\text{Se}$  and  $\text{Tl}-\text{As}-\text{S}$  lie on composition joins such as  $\text{Tl}_2\text{Se}-\text{As}_2\text{Se}_3$  and  $\text{Tl}_2\text{S}-\text{As}_2\text{S}_3$ . The approach used in the phase diagram study was to determine the melting relations along these joins using both quench-type and thermal analysis experiments. In most cases the joins are pseudobinary, or nearly so, so that they can be treated as two-component systems, remembering, however, that phases such as the vapor phase (always present in a rigid container) have compositions that lie off the joins.

##### 4.2.2 The Join $\text{Tl}_2\text{Se}-\text{As}_2\text{Se}_3$

This join (Fig. 8) is perhaps the most important join in the  $\text{Tl}-\text{As}-\text{S}-\text{Se}$  system from a device standpoint because it contains the nonlinear compound  $\text{Tl}_3\text{AsSe}_3$ . There are two pseudobinary compounds,  $\text{Tl}_3\text{AsSe}_3$  and  $\text{TlAsSe}_2$ , with intermediate pseudobinary eutectics. Both phases have narrow solubility limits, probably less than 1 mole %

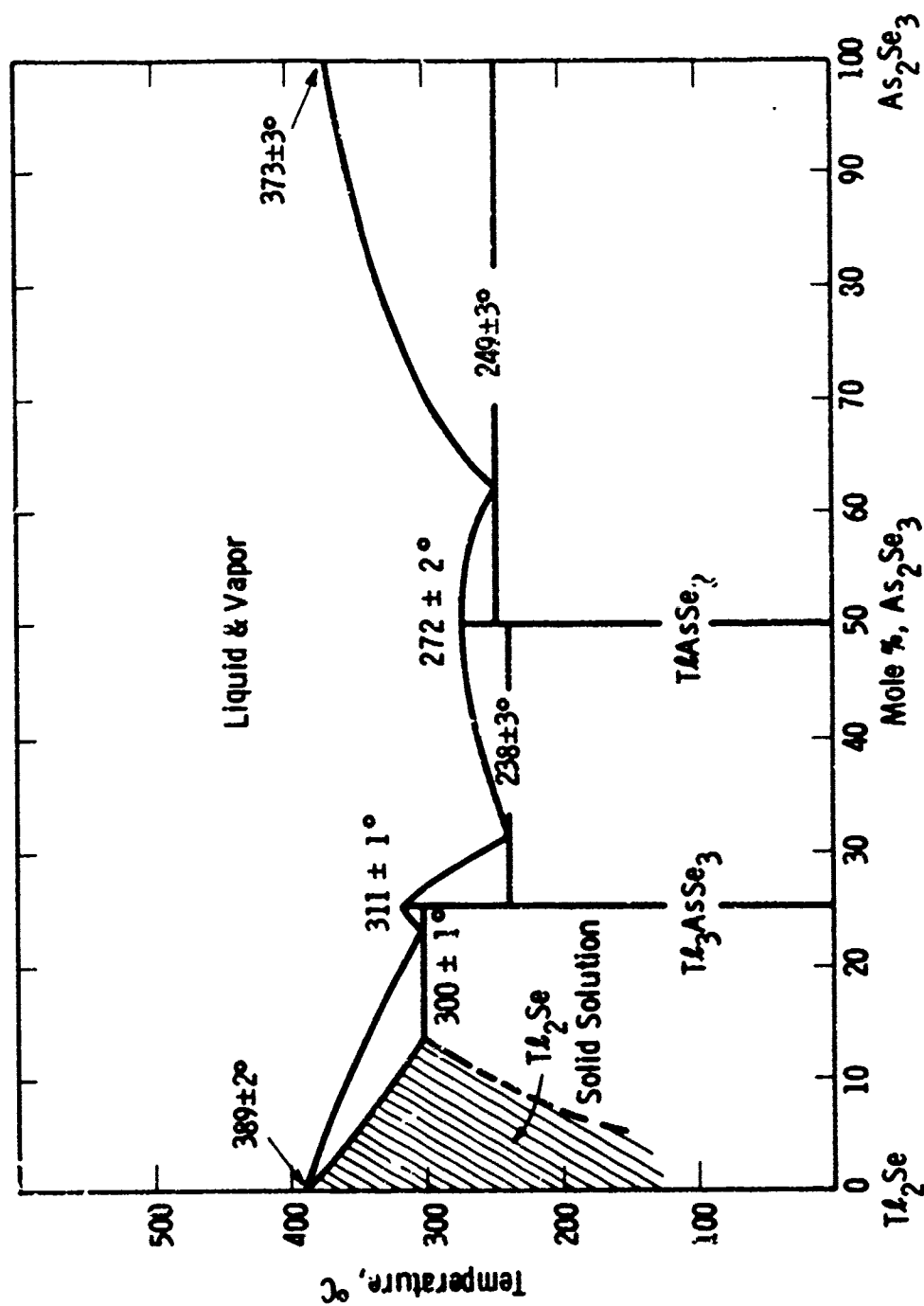


Fig. 8 — Phase relations along the join  $\text{Tl}_2\text{Se}-\text{As}_2\text{Se}_3$  according to this study.

toward  $\text{Tl}_2\text{Se}$  or  $\text{As}_2\text{Se}_3$ , as demonstrated both by appearance of phase experiments and by the very small shifts in x-ray line positions on powder photographs. There is, however, a surprisingly large solid solution of  $\text{Tl}_2\text{Se}$  toward  $\text{As}_2\text{Se}_3$ : 10 mole % or more at  $300^\circ\text{C}$ ; the solid solution limits were not precisely defined since they are of little importance to our crystal growth efforts.

Substantial effort was applied to determining the exact melting relations of  $\text{Tl}_3\text{AsSe}_3$  because these relations are crucial to  $\text{Tl}_3\text{AsSe}_3$  crystal growth. An expanded phase diagram for a portion of the  $\text{Tl}_2\text{Se}-\text{As}_2\text{Se}_3$  system is shown in Fig. 9. The maximum melting composition does not lie at the stoichiometric  $\text{Tl}_3\text{AsSe}_3$  composition, but at a point slightly toward  $\text{Tl}_2\text{Se}$  from ideal, at 24.625 mole %  $\text{As}_2\text{Se}_3$ . The freezing temperatures obtained from the cooling curves alone were not sufficient to locate the maximum melting composition this accurately. The presence or absence of the eutectic arrests at  $300^\circ\text{C}$  and  $240^\circ\text{C}$  permitted the maximum to be defined more precisely than the freezing temperatures taken alone. A 24.75 mole %  $\text{As}_2\text{Se}_3$  composition showed only the lower eutectic, indicating that this composition lies to the  $\text{As}_2\text{Se}_3$ -rich side of the maximum. A 24.5 mole %  $\text{As}_2\text{Se}_3$  composition showed only the upper eutectic, indicating that this composition lies to the  $\text{Tl}_2\text{Se}$ -rich side of the maximum. A 24.625 mole %  $\text{As}_2\text{Se}_3$  sample showed faint arrests corresponding to both eutectics. Of course, the maximum melting composition should ideally show neither eutectic; however, slight compositional inhomogeneities



Curve 652097-A

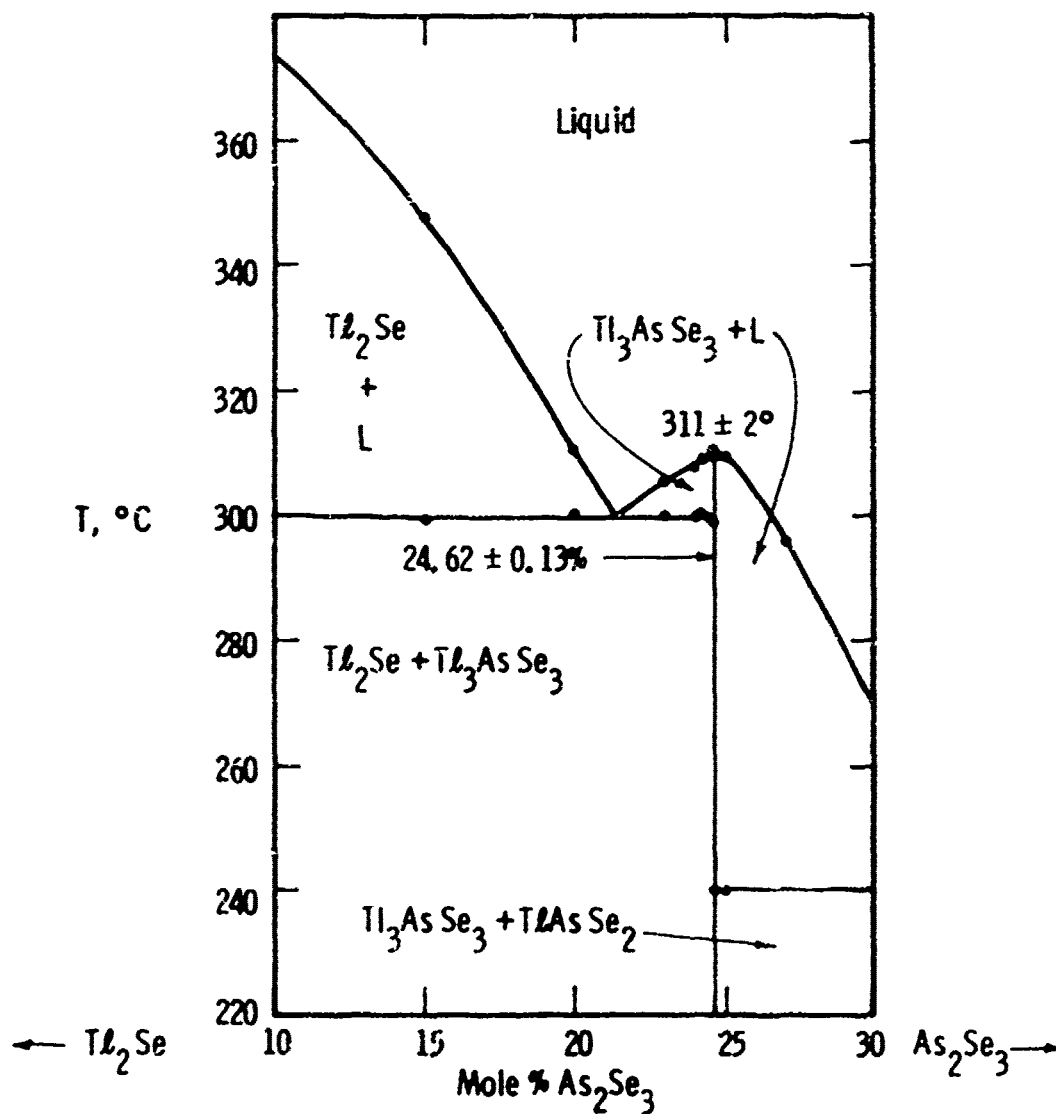


Fig. 9 --- Partial phase diagram for the  $\text{Tl}_2\text{Se}-\text{As}_2\text{Se}_3$  system. The points represent thermal arrests.

in the melt probably account for the appearance of both eutectics.

The implications of Fig. 9 for the crystal growth of  $\text{Tl}_3\text{AsSe}_3$  will be discussed in detail in Sec. 5.3.1; it is sufficient to note here, however, that there is a substantial improvement in crystals grown from melts containing 24.625 mol %  $\text{As}_2\text{S}_3$  over those grown from a stoichiometric  $\text{Tl}_3\text{AsSe}_3$  melt.

A comparison of Fig. 8 with Fig. 6 shows that our results agree with those of Demborskii et al.<sup>9</sup> in that the eutectic temperatures and the  $\text{TlAsSe}_2$  melting temperature are in fair agreement for the two studies. The major discrepancy deals with the melting relations of  $\text{Tl}_3\text{AsSe}_3$ ; according to Dembovskii et al.  $\text{Tl}_3\text{AsSe}_3$  melts incongruently at 280°C to a mixture of  $\text{Tl}_2\text{Se}$  (8) and liquid. Our experiments show that  $\text{Tl}_3\text{AsSe}_3$  melts congruently at 311°C. Several lines of evidence in addition to our thermal data indicate this to be correct:

- 1) We cannot detect any melting when small portions of  $\text{Tl}_3\text{AsSe}_3$  are heated in sealed tubes below 311°C. According to the Dembovskii et al. phase diagram, the equilibrium assemblage should be  $\text{Tl}_2\text{Se} + \text{L}$  between 280°C and ~ 316°C. The presence of liquid should be clearly visible in our experiments.
- 2) Rapidly-quenched charges of  $\text{Tl}_3\text{AsSe}_3$  liquid appear to be homogeneous  $\text{Tl}_3\text{AsSe}_3$  in polished section under the microscope. It is unlikely that that equilibrium would be maintained in such chilled samples so that incongruent melting would be indicated by polyphase products.

3) Slowly-cooled melts such as we use for crystal growth would initially crystallize to  $\text{Tl}_2\text{Se}$  according to the Dembovskii et al. diagram. We see no evidence of this in our crystal growth runs. Large single crystals of  $\text{Tl}_3\text{AsSe}_3$  would be an unlikely product if, in fact, the compound melted incongruently.

We thus feel that all the evidence supports our contention that  $\text{Tl}_3\text{AsSe}_3$  melts congruently rather than incongruently; we cannot, however, offer any explanation for the discrepancy.

Long-term annealing experiments conducted to determine whether there are other intermediate phases, besides  $\text{Tl}_3\text{AsSe}_3$  and  $\text{TlAsSe}_2$ , are summarized in Table 2. To aid the attainment of equilibrium, reactant material was either melted prior to use, or consisted of previously-synthesized compounds which were pressed into pellets to ensure intimate contact between the reactant phases. The only product phases identified by x-ray powder diffraction were  $\text{Tl}_2\text{Se}$ ,  $\text{Tl}_3\text{AsSe}_3$ ,  $\text{TlAsSe}_2$ , or  $\text{As}_2\text{Se}_3$ . We conclude that there are no intermediate phases in the system  $\text{Tl}_2\text{Se}-\text{As}_2\text{Se}_3$  at temperatures of  $150^\circ\text{C}$  or above.

#### 4.2.3 The $\text{Tl}_2\text{S}-\text{As}_2\text{S}_3$ Join

The partial phase diagram for the  $\text{Tl}_2\text{S}-\text{As}_2\text{Se}_3$  system is shown in Fig. 10. The eutectic horizontal at  $231^\circ\text{C}$  was obtained from heating curves and quenching. Cooling curve arrests corresponding to this eutectic were as much as  $45^\circ\text{C}$  low. No liquidus arrests were obtained for compositions containing 35 mol % or more  $\text{As}_2\text{S}_3$ , due to

TABLE 2

Low-Temperature Annealing Experiments

<u>Run No.</u>	<u>Reactant Key</u> <sup>*</sup>	<u>T, °C</u>	<u>Time</u>	<u>Products</u>
TAS 73	1	200°C	11 days	$\text{Tl}_2\text{Se} + \text{Tl}_3\text{AsSe}_3$
TAS 88	2	200°C	36 days	$\text{Tl}_3\text{AsSe}_3 + \text{TlAsSe}_2$
TAS 89	3	200°C	36 days	$\text{TlAsSe}_2 + \text{As}_2\text{Se}_3$
TAS 80	1	150°C	61 days	$\text{Tl}_2\text{Se} + \text{Tl}_3\text{AsSe}_3$
TAS 81	4	150°C	61 days	$\text{Tl}_3\text{AsSe}_3 + \text{TlAsSe}_2$
TAS 83	5	150°C	61 days	$\text{TlAsSe}_2 + \text{As}_2\text{Se}_3$

- \* 1) Composition 15 mol %  $\text{As}_2\text{Se}_3$ ; melted prior to annealing.  
 2) Pressed pellet of  $\text{Tl}_3\text{AsSe}_3 + \text{TlAsSe}_2$ .  
 3) Pressed pellet of  $\text{TlAsSe}_2 + \text{As}_2\text{Se}_3$ .  
 4) Composition 35 mol %  $\text{As}_2\text{Se}_3$ ; melted prior to annealing.  
 5) Composition 70 mol %  $\text{As}_2\text{Se}_3$ ; melted prior to annealing.

the formation of glasses on cooling. We did, however, do melting-point experiments on  $\text{TlAsS}_2$  and find that it melts congruently at  $286 \pm 3^\circ\text{C}$ .

Compositions lying on the  $\text{Tl}_2\text{S}-\text{As}_2\text{S}_3$  join yielded reliable data with great reluctance. The compositions tested lying on the  $\text{Tl}_2\text{S}$  rich side of the eutectic at about 22%  $\text{As}_2\text{S}_3$  did not define the liquidus in this region. When run in normal fashion, i.e., cooling the melt from  $50^\circ\text{C}$  or more above the estimated liquidus, compositions on the  $\text{As}_2\text{S}_3$ -rich side of the maximum yielded arrests corresponding to

the dotted curve. These compositions exhibited substantial supercooling (30°C or more). We also observed that the temperature rise following nucleation was sluggish. This system is clearly not "well-behaved" in a classical sense, so that the data obtained to this point raised more questions than they answered.

We hypothesized that there was some partial structure remaining in the liquid at temperatures slightly above the liquidus, which is broken up at the higher temperatures to which the melt is generally heated. On subsequent cooling from a high temperature, nucleation and growth occur with difficulty. We then reran several samples in an attempt to hold the maximum temperature of the melt within about 10°C of the liquidus arrest. The desired temperature was estimated from the heating curve, which indicated liquidus temperatures considerably higher than those obtained from the previous cooling curves. After some trial and error, we were able to obtain cooling curves with no supercooling. In fact, when the maximum melt temperature did not exceed 10°C above the liquidus, the arrests formed a smooth curve without the sharp break associated with sudden nucleation. These experiments yielded the solid curve on the  $\text{As}_2\text{S}_3$ -rich side of the maximum.

#### 4.2.4 The $\text{Tl}_2\text{S}$ - $\text{As}_2\text{S}_5$ Join

The composition join  $\text{Tl}_2\text{S}$ - $\text{As}_2\text{S}_5$  appears pseudobinary, at liquidus temperatures, over the range 0 to 35 mol %  $\text{As}_2\text{S}_5$ . The diagram is shown in Fig. 11. The group of points in the neighborhood of

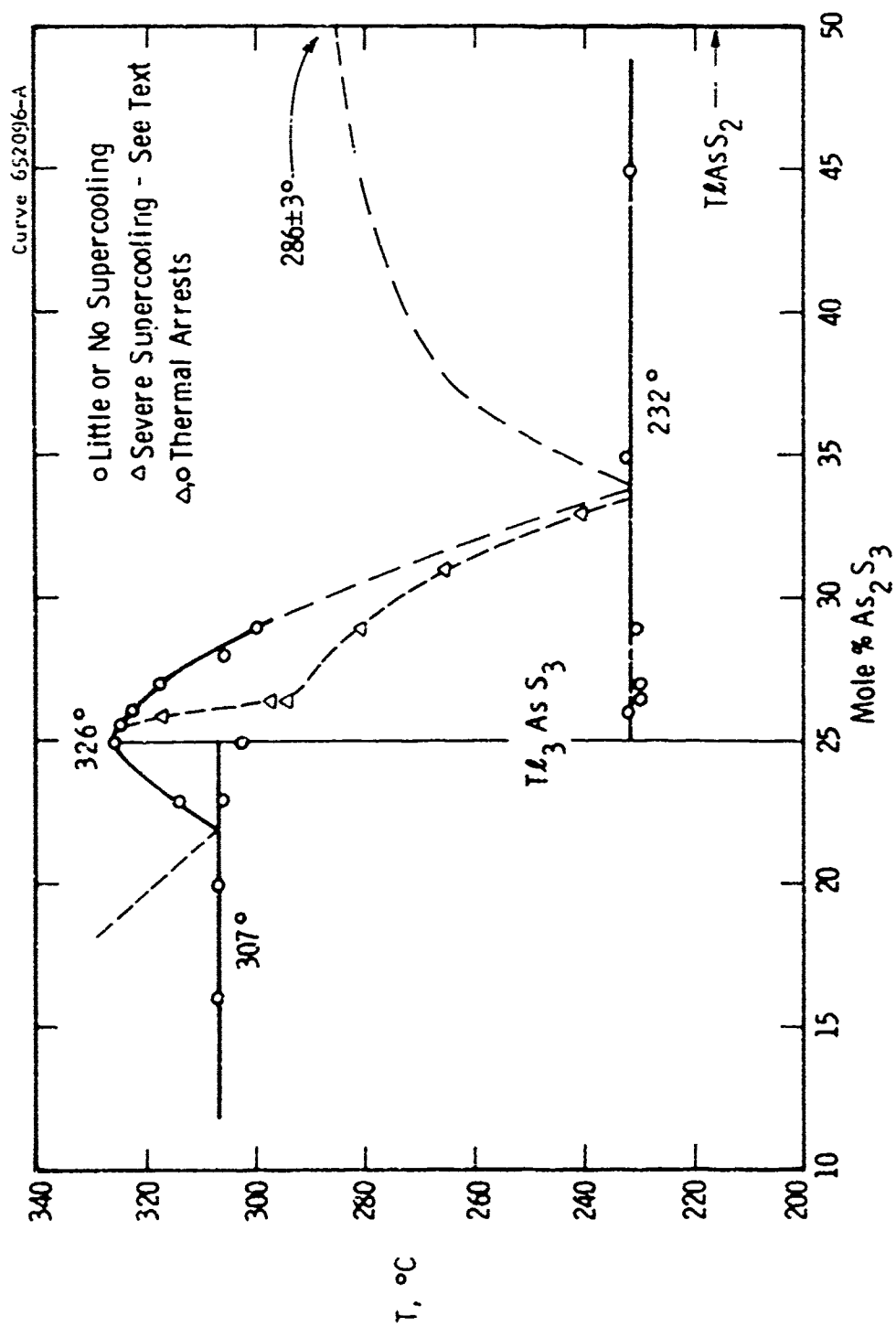


Fig. 10 -- Partial phase diagram for the system Tl<sub>2</sub>S-As<sub>2</sub>S<sub>3</sub>.

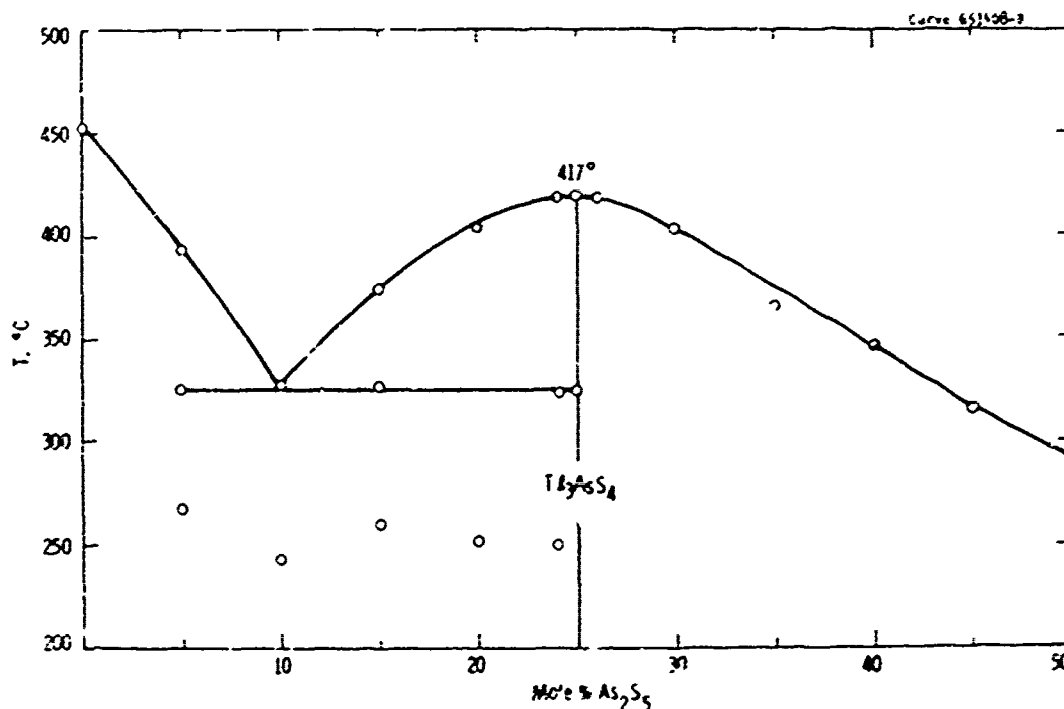


Fig. 1' -- The  $\text{Tl}_2\text{S}$ - $\text{As}_2\text{S}_5$  join.

250°C on the  $\text{Tl}_2\text{S}$ -rich side of  $\text{Tl}_3\text{AsS}_4$  corresponds to very small thermal arrests observed on cooling curves for all the compositions examined on that portion of the join. These points probably correspond to a single temperature, as it is not uncommon to observe some scatter in the temperature at which very small arrests occur in systems where the phases involved exhibit substantial supercooling. They probably represent the temperature of a ternary eutectic lying off the composition join, but their origin was not pursued. The maximum-melting  $\text{Tl}_3\text{AsS}_4$  composition appears to lie at 25 mol %  $\text{As}_2\text{S}_5$ , i.e., at least as viewed on this join, the compound is stoichiometric.

The  $\text{Tl}_3\text{AsS}_4$  liquidus surface on this join was studied to a composition 50 mol %  $\text{As}_2\text{S}_5$ ; the curve descends smoothly and there is no indication of additional congruently-melting compounds intersecting the liquidus surface.

#### 4.2.5 $\text{Tl}_3\text{AsS}_3$ -S Join

The composition join  $\text{Tl}_3\text{AsS}_3$ -S was studied, not only to define the melting relations of  $\text{Tl}_3\text{AsS}_3$ , but also those of  $\text{Tl}_3\text{AsS}_4$ . The phase diagram is shown in Fig. 12.

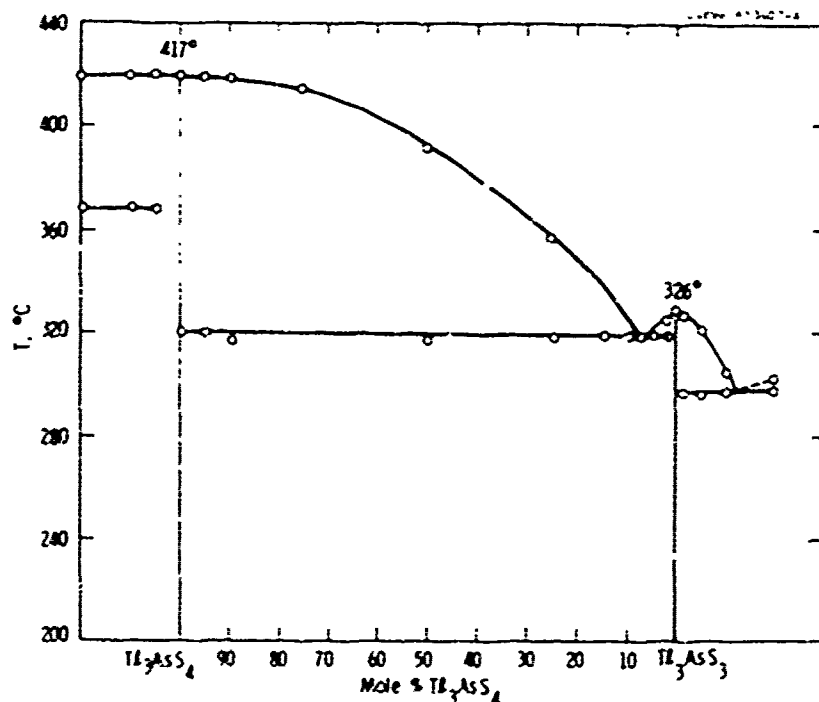


Fig. 12 -- A portion of the  $\text{Tl}_3\text{AsS}_3$ -S join. The points represent arrests in thermal analysis experiments.

An eutectic between  $\text{Tl}_3\text{AsS}_3$  and  $\text{Tl}_3\text{AsS}_4$  occurs at  $326^\circ\text{C}$  and at a composition very near  $\text{Tl}_3\text{AsS}_3$ . The close proximity of the



two eutectics to  $\text{Tl}_3\text{AsS}_3$  can be appreciated by noting that the difference in sulfur content between  $\text{Tl}_3\text{AsS}_3$  and  $\text{Tl}_3\text{AsS}_4$  is only about 3.4 wt %.

The liquidus surface for  $\text{Tl}_3\text{AsS}_4$  is very broad, as it was also on the  $\text{Tl}_2\text{S}-\text{As}_2\text{S}_5$  join. Repeated examination of the thermal data produced by stoichiometric  $\text{Tl}_3\text{AsS}_4$  show a small heating arrest at about  $320^\circ\text{C}$ , indicating that the true maximum-melting composition lies slightly off the stoichiometric composition, probably toward sulfur. This observation is discussed further with reference to the crystal growth of  $\text{Tl}_3\text{AsS}_4$ .

#### 4.2.6 $\text{Tl}_2\text{Se}-\text{As}_2\text{Se}_5$ and $\text{Tl}_3\text{AsSe}_3$ - $\text{Tl}_3\text{AsSe}_4$ Joins

The thermal analysis data did not yield clear results for the phase boundaries in the region of  $\text{Tl}_3\text{AsSe}_4$ . If there is indeed a maximum in the liquidus, it is very small, with an eutectic within one or two percent of the stoichiometric composition on the  $\text{Tl}_2\text{Se}$  side. Our data do not rule out a peritectic reaction, but if such is the case, the intersection of the peritectic horizontal with the liquidus must occur very near the equilibrium compound composition, based not only on the thermal data but also on our success in preparing good crystalline material with our normal crystal growth techniques.

The liquidus is rather broad from  $\text{Tl}_3\text{AsSe}_3$  toward  $\text{Tl}_3\text{AsSe}_4$ . However, for compositions richer in sulfur than  $\text{Tl}_3\text{AsSe}_{3.85}$ , the data again cannot be interpreted.

Thus, even though the exact phase relationships in the immediate vicinity of  $\text{Tl}_3\text{AsSe}_4$  are not well defined, the region of uncertainty occupies a very small composition region in the ternary system, and thus the region of exploration for crystal growth experiments is fairly well defined.

#### 4.2.7 Ternary Phase Relations

The results of the phase diagram work on the  $\text{Tl}_2\text{S}-\text{As}_2\text{S}_3$ ,  $\text{Tl}_2\text{S}-\text{As}_2\text{S}_5$  and  $\text{Tl}_3\text{AsS}_3-\text{Tl}_3\text{AsS}_4$  joins are brought together in Figs. 13 and 14. Figure 13 is an overview of the Tl-As-S ternary system which defines the three joins in terms of the elemental components and shows their mutual relationships. Figure 14 is a detailed view of the region of the ternary shown in Fig. 13 which contains  $\text{Tl}_3\text{AsS}_3$  and  $\text{Tl}_3\text{AsS}_4$ . The eutectics observed on the various joins are marked X in Fig. 14. Isotherms at 320°C and 400°C are shown as dashed curves. The 320°C isotherms intersect the eutectic closest to  $\text{Tl}_3\text{AsS}_3$  on the  $\text{Tl}_3\text{AsS}_3-\text{Tl}_3\text{AsS}_4$  join.

Figure 14 clearly illustrates the narrowness of the  $\text{Tl}_3\text{AsS}_3$  maximum and the broadness of the  $\text{Tl}_3\text{AsS}_4$  maximum in relation to nearby eutectics. These ternary relationships have a strong bearing on the growth of high quality single crystals, particularly of  $\text{Tl}_3\text{AsS}_3$ . The phase diagram data indicate that the maximum melting composition for  $\text{Tl}_3\text{AsS}_3$  is very close to stoichiometry. However, the close proximity of the eutectics surrounding  $\text{Tl}_3\text{AsS}_3$  will require the maximum melting composition to be known to an extreme degree of precision if high quality crystals are to be grown.

(Curve 653610-N)

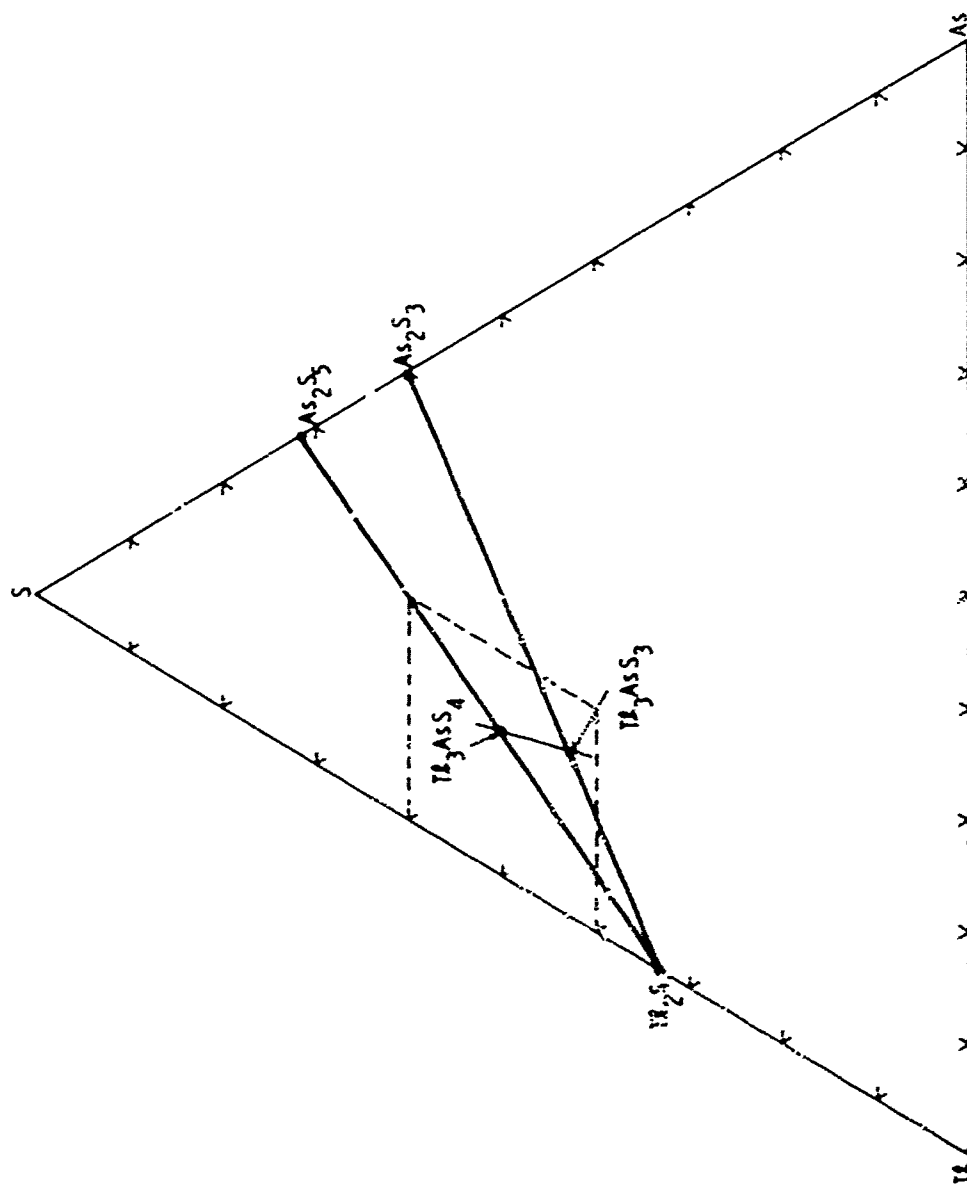


Fig. 13 -- The Ti-As-S Ternary System. The outlined portion is shown enlarged in Fig. 14.

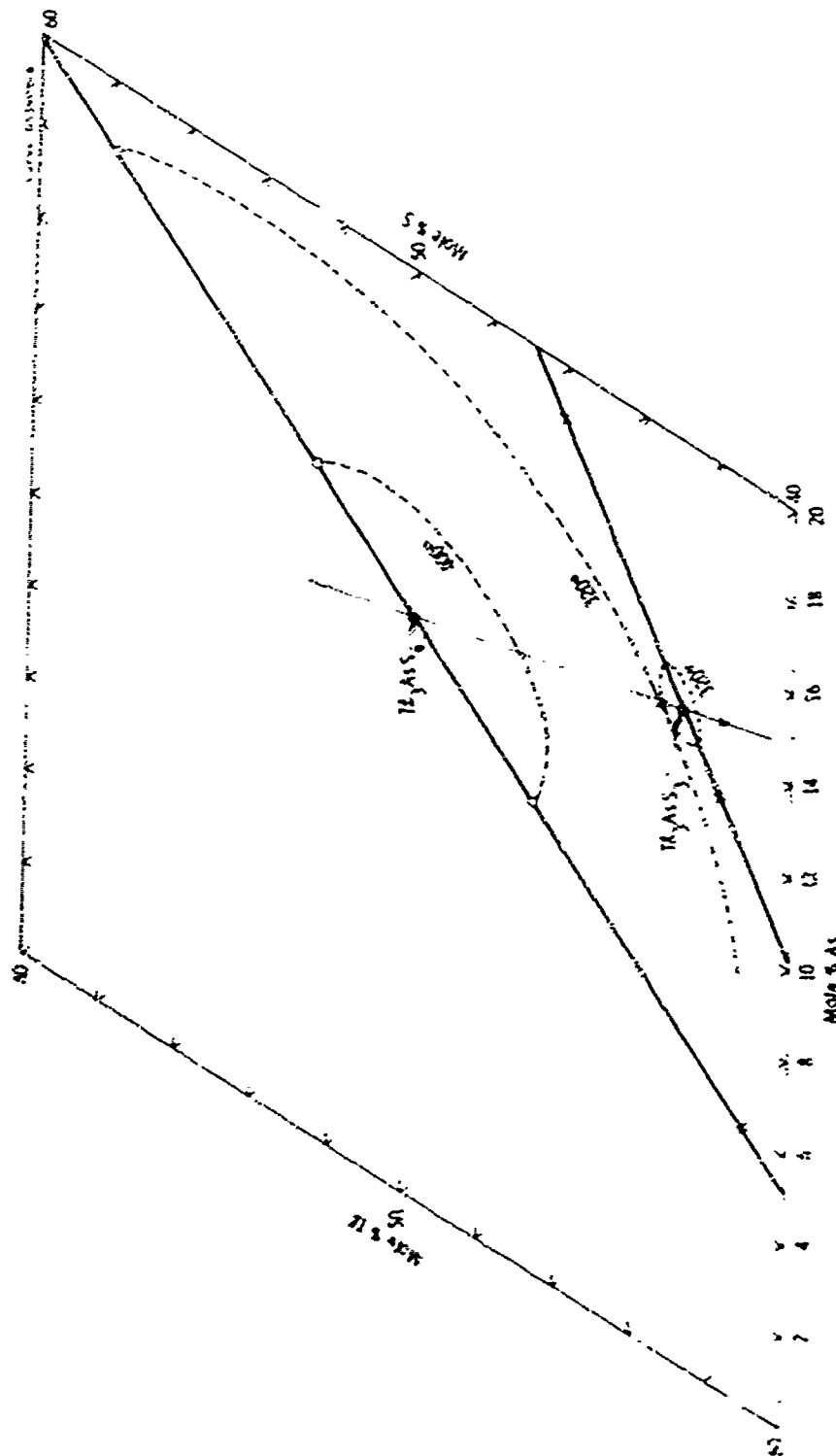


Fig. 14 -- Detail of Tl-As-S system in the region of Tl<sub>3</sub>AsS<sub>3</sub> and Tl<sub>3</sub>AsS<sub>4</sub>; the N's correspond to eutectics on the pseudobinary joins

## 5. CRYSTAL GROWTH

### 5.1 Introduction

The available data on phase relations have important implications for crystal growth of sulfosalt compounds. We have been able to grow high quality crystals of  $\text{Tl}_3\text{AsSe}_3$  and  $\text{Tl}_3\text{AsS}_4$ , but only fair quality crystals of  $\text{Tl}_3\text{AsS}_3$  and  $\text{Tl}_3\text{AsSe}_4$ . We believe the phase diagram study explains this observation. Our study revealed that these latter two compounds are surrounded by pseudobinary eutectics that are close in composition to the congruently melting compositions. Thus, crystal growth may well be hampered by "eutectic interference" of the type proposed to explain growth phenomena<sup>1</sup> in proustite,  $\text{Ag}_3\text{AsS}_3$ . In the case of the compounds  $\text{Tl}_3\text{AsSe}_3$  and  $\text{Tl}_3\text{AsS}_4$ , although pseudobinary eutectics are present, they lie at more distant compositions from the stoichiometric compounds and thus eutectic interference does not impede the growth of large crystals. Our methods of crystal-quality evaluation and crystal growth efforts for each compound studied are described below.

### 5.2 Crystal-Quality Evaluation

Of the crystals examined during this study, only  $\text{Tl}_3\text{AsS}_4$  was transparent in a portion of the visible wavelength spectrum. Thus,

the crystal quality of  $\text{Ti}_3\text{AsS}_4$  could be quickly determined by visual inspection (i.e., were cracks present?) and by illuminating the interior of the crystal with a He-Ne laser beam. This latter technique was particularly useful for detecting tiny light-scattering inclusions.

The band-edges of  $\text{Ti}_3\text{AsS}_3$ ,  $\text{Ti}_3\text{AsSe}_3$ , and  $\text{Ti}_3\text{AsSe}_4$  were in the near infrared and it was therefore impossible to inspect or measure the optical quality of bulk single crystals using visible radiation. Initially, we attempted to use an infrared image converter camera (Bofars MARK IRCD-1) with suitable infrared optics, to image crystal interiors at a wavelength of about  $1.5 \mu\text{m}$ . The resolution of this system was unsatisfactory, although with further work on the optics we believe it could be improved considerably.

A scanning technique for profiling the optical loss in single sulfosalt crystals has been set up, as shown in Fig. 15. An infrared laser beam is incident onto a  $\text{Ti}_3\text{AsSe}_3$  boule onto which plane parallel inspection faces have been ground and polished. The power transmitted through the crystal is recorded as the various portions of the crystal are translated through the beam, and the total optical loss is thus characterized as a function of crystal position. It should be noted that this measurement technique gives only the total loss through the crystal. To account accurately for reflection losses, the crystal refractive indices and its orientation relative to the polarization of the incident beam must be known. In addition, low angle scattering losses are not accounted for, because the power meter acceptance solid angle is relatively large, about  $2 \times 10^{-3}$  steradians.

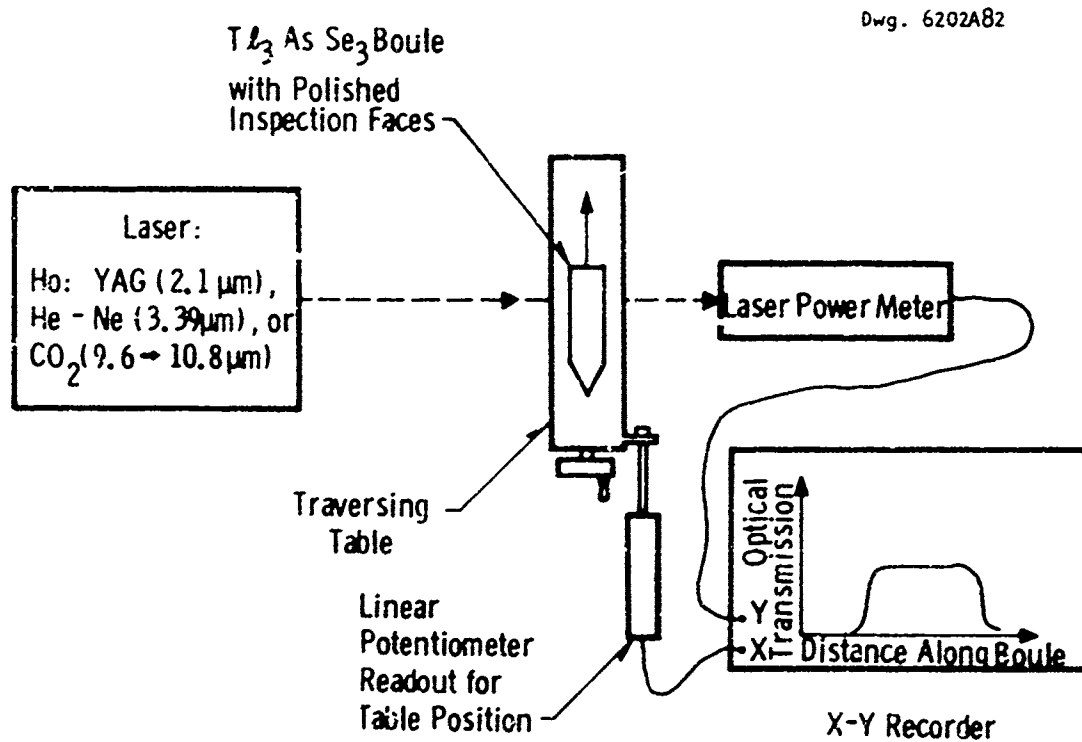


Fig. 15 -- Schematic diagram of optical quality scanning system for sulfosalt crystals.

In Fig. 16 is shown the result of a scan of a 4 cm long  $\text{Tl}_3\text{AsSe}_3$  crystal, TASE-BR-1, at  $2.1 \mu\text{m}$  (Ho:YAG laser). In this case, the seed end is of reasonably good quality, with total optical transmission within 5-10% of the maximum expected when reflection losses are taken into account. Total internal reflection at a cracked section about 2.5 cm from the tail end reduces the transmission to zero in that region; a very lossy region also extends from about 0.5 cm to 2 cm along the boule. Scans of this type were also used to evaluate the optical quality of  $\text{Tl}_3\text{AsS}_3$  and  $\text{Tl}_3\text{AsSe}_4$ .

### 5.3 Crystal Growth

#### 5.3.1 $\text{Tl}_3\text{AsSe}_3$

Crystals of  $\text{Tl}_3\text{AsSe}_3$  were grown at three compositions to determine the optimum growth composition: 1) stoichiometric  $\text{Tl}_3\text{AsSe}_3$ , which contains 25 mol %  $\text{As}_2\text{Se}_3$ ; 2) a composition  $(\text{Tl}_2\text{Se})_{0.75375}(\text{As}_2\text{Se}_3)_{0.24625}$ , and 3) a composition  $(\text{Tl}_2\text{Se})_{0.7525}(\text{As}_2\text{Se}_3)_{0.2475}$ . The latter two compositions lie on the  $\text{Tl}_2\text{Se}-\text{As}_2\text{Se}_3$  composition join but slightly more  $\text{Tl}_2\text{Se}$ -rich than stoichiometric  $\text{Tl}_3\text{AsSe}_3$ ; composition 2) corresponds to the maximum-melting composition as determined by the phase-diagram study. Eight crystal-growth experiments are described in Table 3.

The crystals we grew were examined using our scanning technique. With the total optical losses approaching only a few percent, it is very difficult to obtain accurate measurements of losses and to compare effects of stoichiometry and growth rate on crystal quality



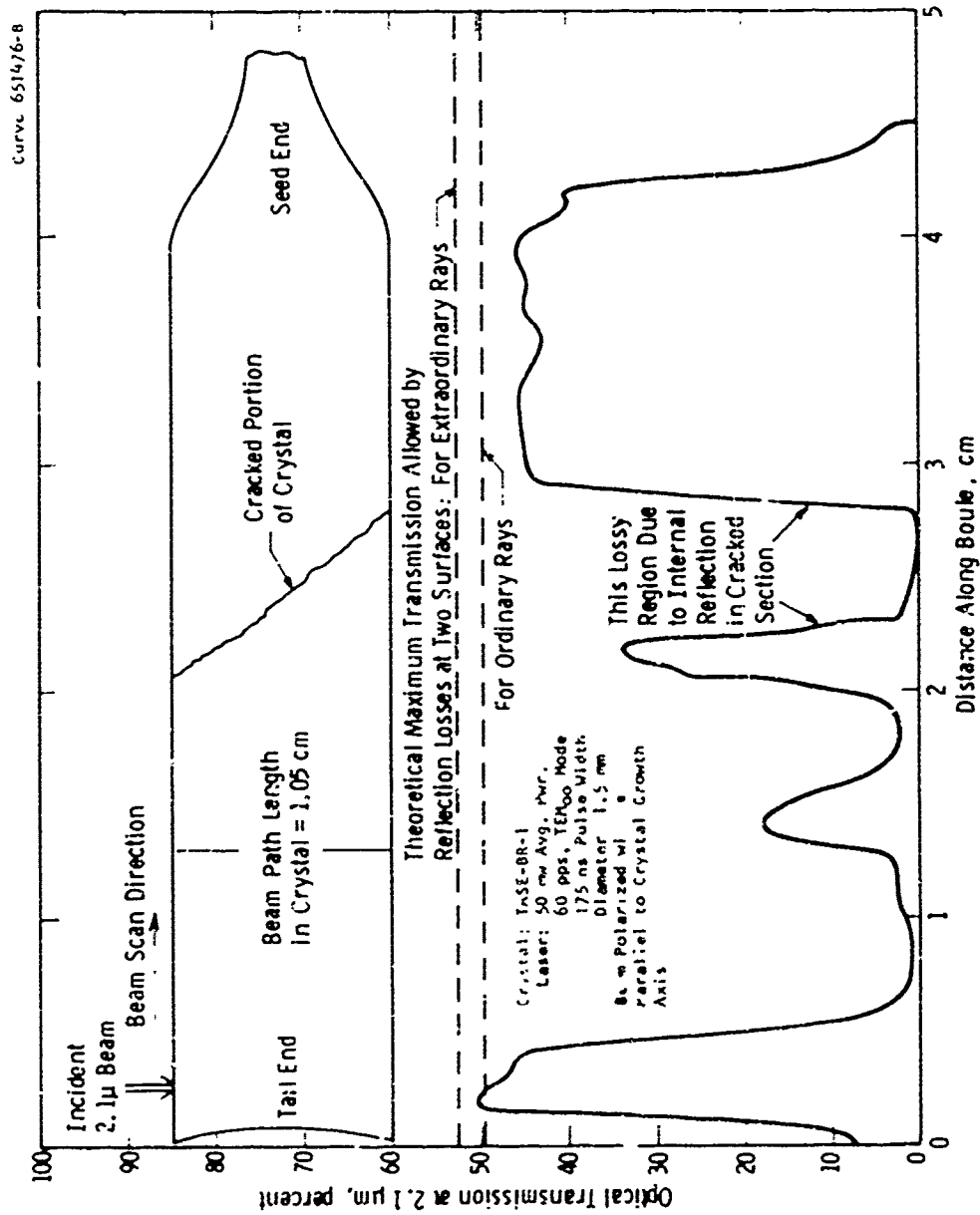


Fig. 16 -- Optical transmission at 2.1  $\mu$ m along an as-grown boule of Tl<sub>3</sub>AsSe<sub>3</sub>

using this transmission technique. This is, however, a useful method for finding the best sections in a particular boule.

In general, the results of Table 3 indicate that  $x = 0.75375$  to  $x = 0.7525$  and a growth rate of the order of 15 mm/day are optimum growth conditions for high quality  $\text{Ti}_3\text{AsSe}_3$ . This is dramatically illustrated by a comparison of crystals TASE-BR-3 and TASE-BR-6 (Figs. 17 and 18). Crystal TASE-BR-3 was grown from the maximum-melting composition; it exhibits large clear regions with bulk losses of nearly zero, at least within the accuracy of our

TABLE 3

Optical Loss Measurements on  $\text{Ti}_3\text{AsSe}_3$  Boules

Boule No.	Composition $(\text{Ti}_2\text{Se})_x(\text{As}_2\text{Se}_3)_{1-x}$	Growth Rate (mm/day)	Length of Best Section (cm)	Optical Loss in Best Section ( $\text{cm}^{-1}$ )
BR-1	(0.75375)(0.24625)	12.2	1.2	0.05 → 0.08
BR-2	(0.75250)(0.24750)	10.5	0.8	0.05 → 0.08
BR-3	(0.75375)(0.24625)	15.3	1.6	~ 0
BR-4	(0.75250)(0.24750)	15.0	1.0	0.02 → 0.04
BR-5	(0.75375)(0.24625)	15.8	2.2	0.03 → 0.06
BR-6	(0.75000)(0.25000)	15.0	2.2	0.03 → 0.06
BR-8	(0.75375)(0.24625)	15.4	1.2	0.02 → 0.04

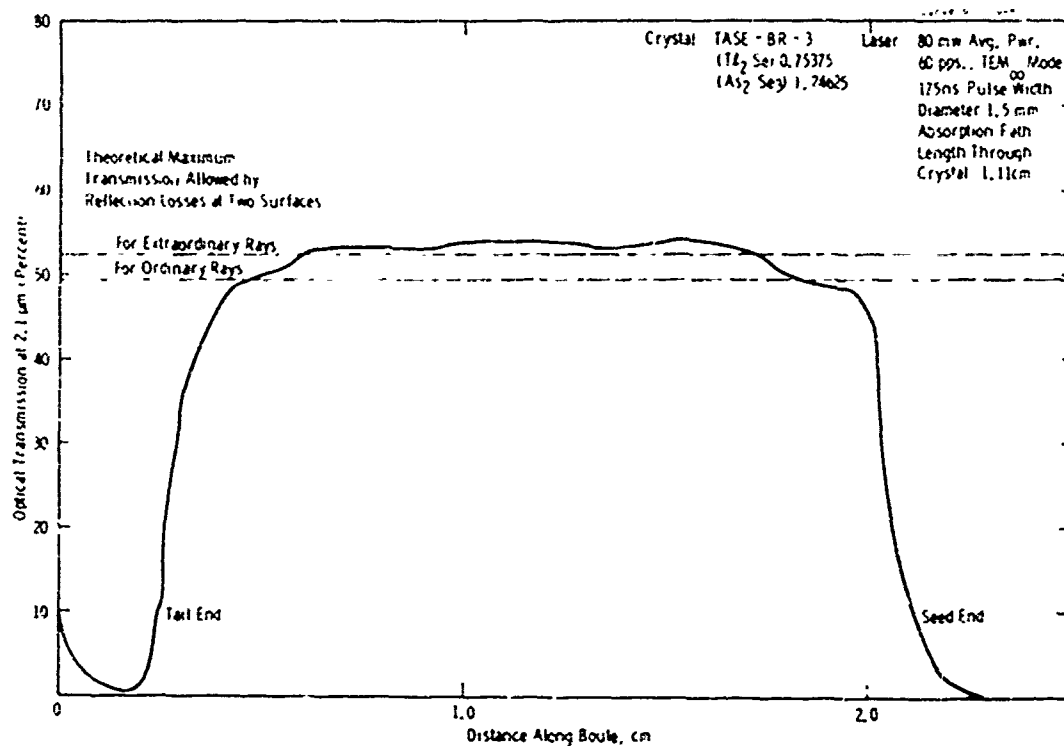


Fig. 17 -- Optical transmission at 2.1  $\mu\text{m}$  along an as-grown boule of  $\text{TL}_3\text{AsSe}_3$ , Crystal TASE-BR-3.

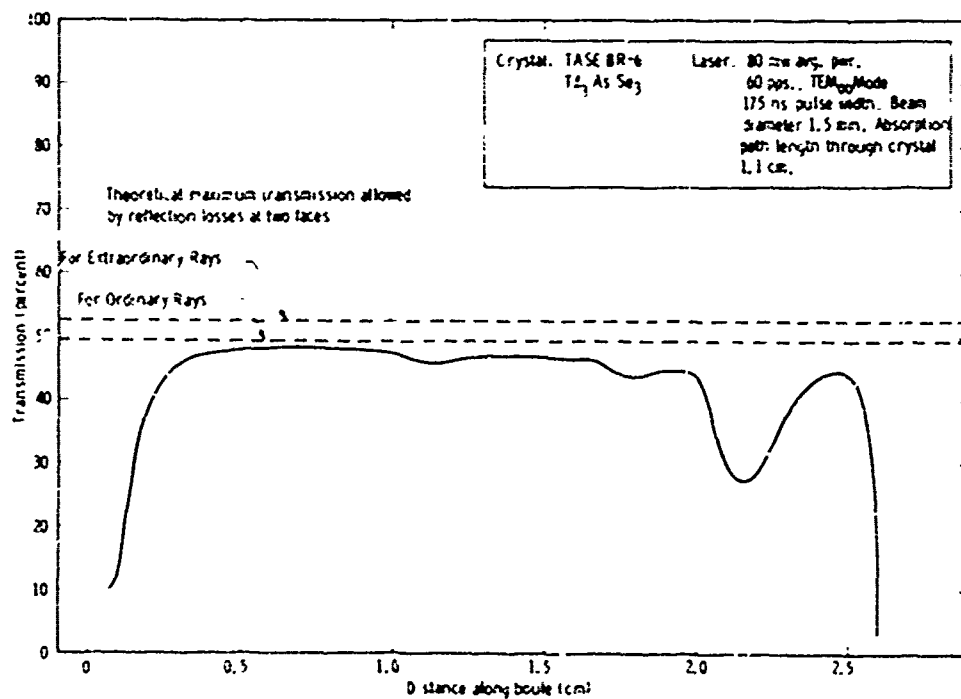


Fig. 18 -- Optical transmission at 2.1  $\mu\text{m}$  along an as-grown boule of  $\text{TL}_3\text{AsSe}_3$  (Crystal TASE-BR-6).

measurement technique. The transmission of BR-3 actually appears to exceed the theoretical maximum by a small amount; this is probably due to a slow fluctuation in the probe laser average power, which is continually monitored but fluctuates by about  $\pm 2\%$ . The actual losses in BR-3 appear to be approaching  $0.01 \text{ cm}^{-1}$  or less.

Crystals grown from stoichiometric  $\text{Tl}_3\text{AsSe}_3$  melts (e.g., TLSE-BR-6), on the other hand, have optical transmissions that do not attain theoretical maximum values (Fig. 18). Often such crystals have variable transmission along the length of the crystal and are also prone to have high-absorption bands, probably impurity bands. The differences are striking considering that only a few tenths of a mol % change in melt composition is involved.

#### 5.3.2 $\text{Tl}_3\text{AsS}_4$

The ternary melting relations determined for  $\text{Tl}_3\text{AsS}_4$  (see Fig. 14) show that there is a very broad liquidus surface surrounding the stoichiometric composition. Insofar as we can tell, the melting maximum on the join  $\text{Tl}_2\text{S}-\text{As}_2\text{S}_5$  occurs at the stoichiometric  $\text{Tl}_3\text{AsS}_4$  composition; because of the rather flat melting maximum on the join  $\text{Tl}_3\text{AsS}_3-\text{S}$ , however, there is uncertainty in the exact maximum-melting composition. For this reason, we conducted a series of crystal growth experiments along the join  $\text{Tl}_3\text{AsS}_3-\text{S}$  to determine the optimum  $\text{Tl}_3\text{AsS}_4$  growth composition empirically, i.e., by growing crystals from melts containing different amounts of S and comparing the crystals as to their optical quality.

Crystals were grown from four compositions:  $\text{Tl}_3\text{AsS}_{3.95}$ ,  $\text{Tl}_3\text{AsS}_4$ ,  $\text{Tl}_3\text{AsS}_{4.01}$  and  $\text{Tl}_3\text{AsS}_{4.025}$  (the experimental details are contained in Table 4). Two problems are evident -- crystal cracking and inclusions (best observed as light-scattering centers when crystals are illuminated with a He-Ne laser beam). In fact, however, these two problems are not independent -- crystals with a high inclusion content showed a strong proclivity to fracture on cooling.

The composition  $\text{Tl}_3\text{AsS}_{3.95}$  was chosen to evaluate crystal growth from melts slightly sulfur deficient from the ideal composition. Three separate growth runs were made to ensure reasonable statistics for the data and eliminate possible spurious results caused, for example, by accidentally misweighing reactants. The results clearly show that  $\text{Tl}_3\text{AsS}_{3.95}$  is not a preferred growth composition. Crystals were always severely cracked and, in two of the three runs, single-crystal growth broke down and polycrystalline material comprised several millimeters of the boule length at the end of the charge. In addition, there was a metallic-appearing coating on portions of the surface of the charge (and in all probability it was similar particles that occurred as scattering centers inside the boule). We tried to remove enough of the coating to obtain a powder-diffraction pattern but were not successful.

Similar problems to those described for  $\text{Tl}_3\text{AsS}_{3.95}$  were evident in growth runs on melts of  $\text{Tl}_3\text{AsS}_4$  composition but to a lesser extent. We were, in fact, able to obtain an uncracked boule at room

TABLE 4  
Crystal-Growth Experiments Conducted to Determine  
Optimum Growth Composition for  $\text{Ti}_3\text{AsS}_4$

Run Number	Melt Composition	Growth Rate mm/day	Results
203806-84	$\text{Ti}_3\text{AsS}_{3.95}$	15	Cracked, top of charge polycrystalline
203806-140	$\text{Ti}_3\text{AsS}_{3.95}$	15	Cracked, top of charge polycrystalline
203806-143	$\text{Ti}_3\text{AsS}_{3.95}$	14	Boule completely cracked
204849-34	$\text{Ti}_3\text{AsS}_4$	15	Boule badly cracked
204849-44	$\text{Ti}_3\text{AsS}_4$	15.5	Boule badly cracked
294849-98-1	$\text{Ti}_3\text{AsS}_4$	11.5	Boule cracked
294849-98-2*	$\text{Ti}_3\text{AsS}_4$	8	Uncracked boule obtained at room temperature; boule later cracked spontaneously. Contains inclusions.
206196-3	$\text{Ti}_3\text{AsS}_{4.01}$	18	2 cm of uncracked material (entire boule) inclusion content low.
206196-1	$\text{Ti}_3\text{AsS}_{4.025}$	15.5	1.5 cm of uncracked material; inclusion content low; excess sulfur present

\* A rerun of Boule 204849-98-1.

temperature (although it spontaneously cracked after a few weeks at room temperature) by regrowing a crystal at a slow growth rate (8 mm/day). This procedure in effect uses the first furnace pass as a zone refining step for subsequent crystal growth. Still, however, the crystal contained numerous inclusions. There is a marked diminishing of the metallic surface coating on going from melts of  $\text{Tl}_3\text{AsS}_{3.95}$  to melts of  $\text{Tl}_3\text{AsS}_4$  composition, which indicated that we were changing composition in the right direction, i.e., that the maximum-melting composition for this phase contains slightly more sulfur than indicated by the formula  $\text{Tl}_3\text{AsS}_4$ . Our observation of a thermal arrest at the  $\text{Tl}_3\text{AsS}_4$ - $\text{Tl}_3\text{AsS}_3$  eutectic temperature (320°C) in a melt of composition  $\text{Tl}_3\text{AsS}_4$  supported this conclusion.

Un-cracked crystal lengths exceeding 1 cm were obtained for crystals grown with sulfur in excess of the ideal  $\text{S}_4$  composition, and in fact the boule was crack-free for  $\text{Tl}_3\text{AsS}_{4.01}$ . Excess sulfur was present in the crystal-growth run from  $\text{Tl}_3\text{AsS}_{4.025}$  composition; it coated the tube as a sulfur-rich liquid during growth. These observations clearly substantiate our phase diagram interpretation that the maximum-melting  $\text{Tl}_3\text{AsS}_4$  composition lies slightly toward sulfur from the ideal formula.

### 5.3.3 $\text{Tl}_3\text{AsS}_3$

The phase diagrams show that the growth composition is critical for  $\text{Tl}_3\text{AsS}_3$  growth. This compound is surrounded on all

sides by eutectics, and even the slightest deviation from the maximum-melting point will quickly result in the melt reaching an eutectic composition at the growing interface. Although we do not yet know the optimum composition for growing  $\text{Ti}_3\text{AsS}_3$ , the techniques have been improved to an extent so that single crystal sizes are now available to allow the measurement of the material properties.

Boules grown from stoichiometric  $\text{Ti}_3\text{AsS}_3$  melts are invariably polycrystalline. Results of a scan at  $2.1 \mu\text{m}$  of a longitudinal slice from a recent boule indicate extremely high losses ( $\sim 10 \text{ cm}^{-1}$ ) near the seed end, but considerably lower losses ( $\sim 1.5$  to  $2 \text{ cm}^{-1}$ ) in a region near the tail end of the crystal. These losses are too high for practical applications. The surface of this crystal contained numerous bubbles that we interpreted as indicating the presence of excess sulfur during crystal growth. Therefore, the sulfur content was reduced and an attempt made to grow from a  $\text{Ti}_3\text{AsS}_{2.995}$  composition melt.

The boule contained from the sulfur-deficient melt had sections of much higher optical quality than any obtained before. A section of single crystal  $0.4 \text{ cm}$  in length and  $1 \text{ cm}$  in diameter was obtained with losses on the order of  $0.1$  to  $0.5 \text{ cm}^{-1}$ . Clearly, this optical quality is not sufficient for device use; we were, however, able to measure the optical transmission range for the first time (see Sec. 6.4).



#### 5.3.4 $\text{Ti}_3\text{AsSe}_4$

Three attempts were made to grow  $\text{Ti}_3\text{AsSe}_4$  crystals from melts having the stoichiometric composition. In the first two efforts, only polycrystalline material was obtained, but the third boule contained a section about 1 cm in length that showed relatively low optical absorption. This crystal was obtained late in the program so that the only optical data obtained were the wavelengths of optical transmission. The transmission range is reported in Sec. 6.3.

#### 5.3.5 $\text{TiAsS}_2$

Severe difficulties arise in attempts to grow crystals of  $\text{TiAsS}_2$  (and  $\text{TiAsSe}_2$ ) because of the propensity of these compounds to form a glassy phase. We tried to circumvent the glassy phase of  $\text{TiAsS}_2$  in the following manner. First, a  $\text{TiAsS}_2$  glass was prepared by rapidly chilling  $\text{TiAsS}_2$  liquid. Portions of this glass were then reloaded into a crystal-growing tube, the tube was sealed, and the charge remelted. The charge was then annealed for 17 hr at  $175^\circ\text{C}$ , during which time the  $\text{TiAsS}_2$  glass partly crystallized. During the positioning of the crystal-growth tube in the growth furnace, we were careful not to entirely melt the charge so that the crystalline nuclei present could act as seeds for further growth. Two growth runs were made on this charge at  $12^\circ\text{C/day}$ . In both cases the boule was polycrystalline. Large grains (1 to 3 mm in largest dimension) were present in the boule; the fact that such grains are never seen in

crystallized glass indicates that glass formation did not interfere with crystal growth. Single crystals could possibly be obtained by optimizing the related variables of growth rate and temperature gradient, but because of the low crystal symmetry, we did not continue efforts any further.

### 5.3.5 $\text{TiAsSe}_2$

The techniques discussed above for  $\text{TiAsS}_2$  growth were also tried for the crystal growth of  $\text{TiAsSe}_2$ . We found, however, that when glasses of  $\text{TiAsSe}_2$  were annealed in crystal-growth tubes the tube invariably cracks and shatters -- due apparently to expansion of the material upon solidification. Direct single crystal growth from a completely molten  $\text{TiAsSe}_2$  charge was tried but again the growth tube shattered when the boule was annealed in the lower furnace; the product was polycrystalline.

### 5.3.7 $\text{Ti}_3\text{As}(\text{S,Se})_3$

A crystal growth run was made on the composition  $\text{Ti}_3\text{AsS}_{1.5}\text{Se}_{1.5}$  in the solid-solution series. The resultant boule was polycrystalline; moreover, a change in composition occurred as growth proceeded, indicating that the separation of the solidus and liquidus along the pseudobinary join  $\text{Ti}_3\text{AsS}_3$ - $\text{Ti}_3\text{AsSe}_3$  is sufficient so as to seriously interfere with crystal growth.

## 6. OPTICAL PROPERTIES OF Tl-As-Se-S COMPOUNDS

### 6.1 Tl<sub>3</sub>AsSe<sub>3</sub>

The detailed knowledge of phase equilibria in the system Tl-As-Se developed through thermal analysis techniques has led to the growth of large Tl<sub>3</sub>AsSe<sub>3</sub> crystals of excellent optical quality.

Refractive indices were measured from 1.55  $\mu\text{m}$  to 10.6  $\mu\text{m}$  on an oriented prism of Tl<sub>3</sub>AsSe<sub>3</sub> cut from Boule TASE-BR-3, which we estimated to have the best quality. The indices were measured by the method of perpendicular incidence on a Gaertner L-114 spectrometer, using chopped light from a tungsten filament, with calibrated narrow band filters to select wavelengths, and a cooled InSb detector. The estimated accuracy of the measurements is  $\pm 0.003$ . The results of the refractive index measurements are shown in Fig. 19, where they have been fitted with Sellmeier curves of the type

$$n^2 - 1 = \frac{A}{1 - \left(\frac{\lambda_V}{\lambda}\right)^2} + \frac{B}{1 - \left(\frac{\lambda_R}{\lambda}\right)^2}$$

For  $n_o$  and  $n_e$ ,  $\lambda_V = 0.445 \mu\text{m}$ , and  $\lambda_R = 20 \mu\text{m}$ .

For  $n_o$ ,  $A_o = 10.125$ ,  $B_o = 0.10$ .

For  $n_e$ ,  $A_e = 8.96$ ,  $B_e = -0.05$ .

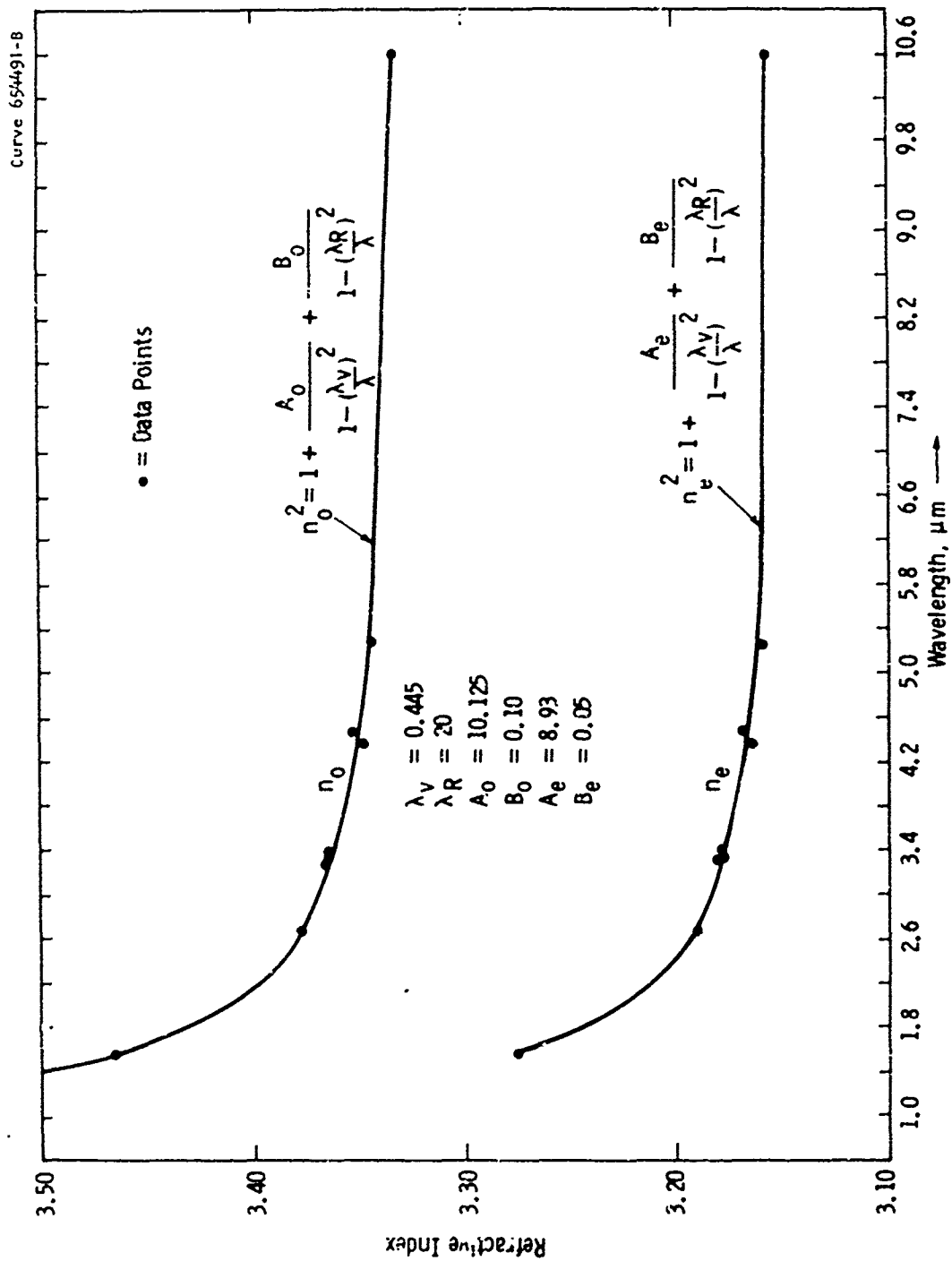


Fig. 19—The refractive indices of  $\text{TL}_3\text{AsSe}_3$  Crystal TASE-BR-3

These indices are slightly larger than those measured on our original  $\text{Ti}_3\text{AsSe}_3$  samples<sup>10</sup>; the birefringence and dispersion have not changed much, however, so there has been little change in the phase-matching conditions.

Using these slightly revised values for the refractive indices, we have recalculated some of the phase matching curves for  $\text{Ti}_3\text{AsSe}_3$ . In Fig. 20, we show the phase match angle,  $\theta_m$ , as a function of wavelength of the fundamental,  $\lambda_0$ , for Type-I phase matched second harmonic generation in  $\text{Ti}_3\text{AsSe}_3$ . We see that  $\theta_m$  ranges from  $48^\circ$  for  $\lambda_0 = 3.0 \mu\text{m}$  to a minimum of about  $14.7^\circ$  at  $11 \mu\text{m}$ . In the  $10.6 \mu\text{m}$  region, the curve is relatively flat, implying that it should be possible to phase match the Type I SHG process for the many rotational-vibrational transitions of a  $\text{CO}_2$  laser at the same angle in the  $\text{Ti}_3\text{AsSe}_3$  crystal. The birefringence angle,  $\rho$ , is large so the walk-off losses will be high.

In Fig. 21 are shown Type I phase matching curves for optical parametric generation, calculated on the basis of the more recent refractive index data. The curves are slightly changed from our original ones<sup>10</sup>; for instance, phase matching for  $2.1 \mu\text{m}$ -pumped degenerate optical parametric oscillation at  $4.2 \mu\text{m}$  is expected to take place at  $\theta_m = 29.7^\circ$ , compared to our originally calculated value of  $\theta_m = 30.2^\circ$ . Curves for pumping at  $1.833 \mu\text{m}$  (Nd:YAG laser) and  $2.795 \mu\text{m}$  (HF laser) are also shown, and the curves have been extended to near the limits of transparency at  $18 \mu\text{m}$ .

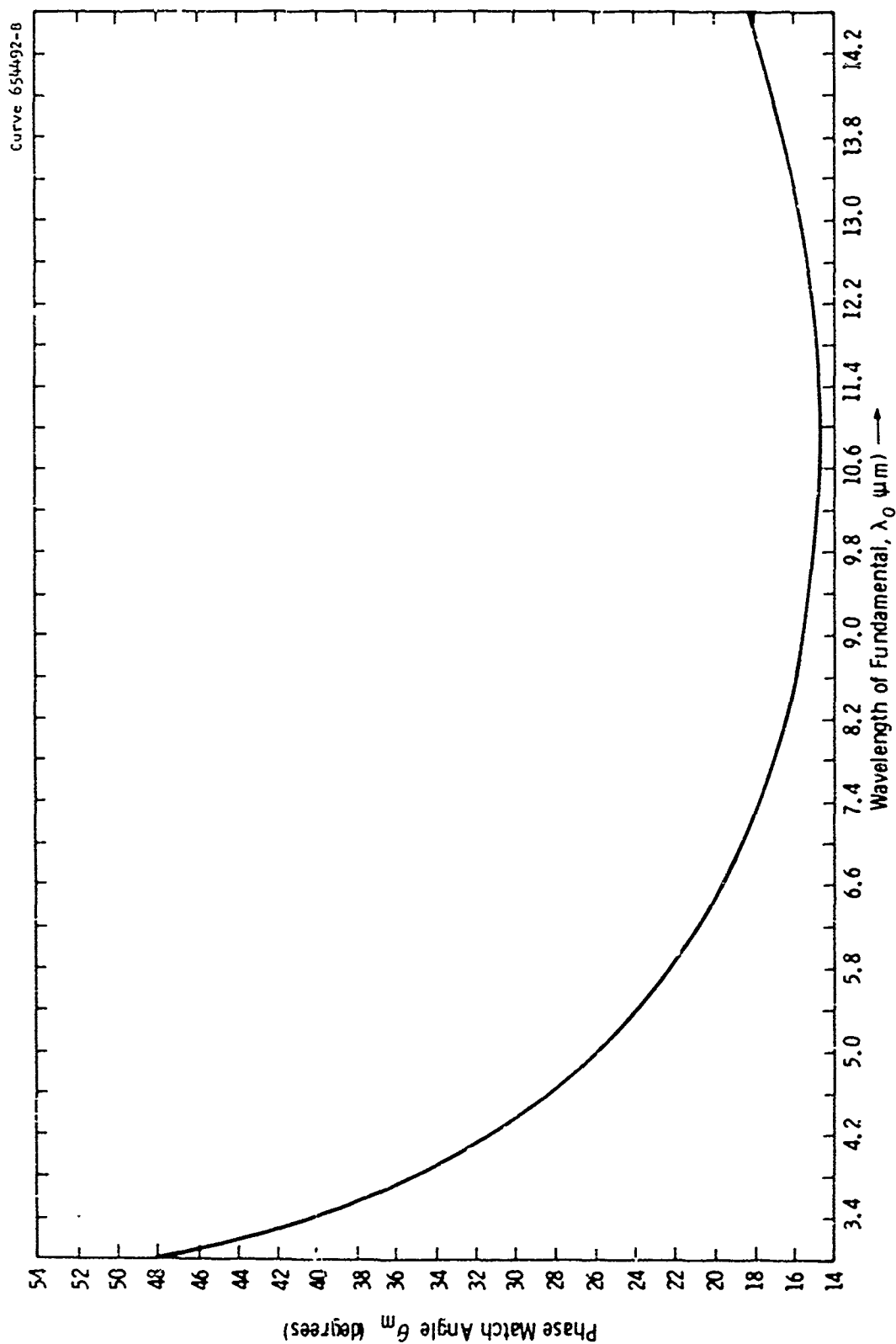


Fig. 20- Calculated phase match angle vs. wavelength of fundamental for Type I Phase-Matched Second Harmonic Generation in  $\text{TeO}_2\text{-As}_2\text{Se}_3$  (Crystal # TASE-BR-3)

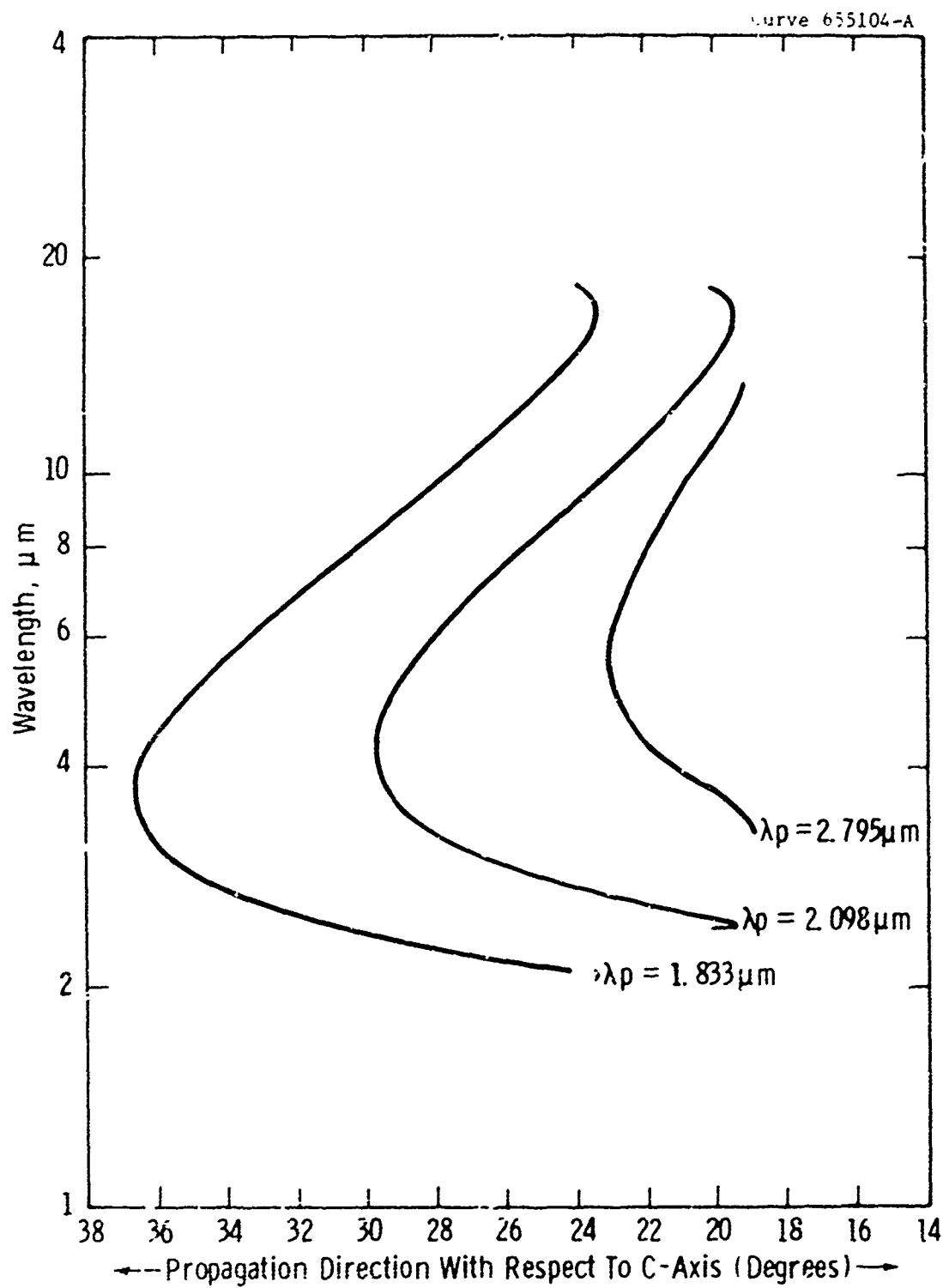


Fig. 21—Phase matching curves (Type I) for optical parametric oscillation in  $\text{Tl}_3\text{AsSe}_3$

## 6.2 $\text{Tl}_3\text{AsSe}_4$

The optical transmission of  $\text{Tl}_3\text{AsSe}_4$  is shown in Fig. 22. The band edge is at about  $1.15\text{ }\mu\text{m}$ , and the transparency range extends to about  $17\text{ }\mu\text{m}$ , although two-phonon absorption peaks at  $11.6\text{ }\mu\text{m}$  and  $12.8\text{ }\mu\text{m}$  reduce transmission in the region beyond  $10\text{ }\mu\text{m}$ .

Since  $\text{Tl}_3\text{AsSe}_4$  is expected to be structurally similar to  $\text{Tl}_3\text{AsS}_4$ , which is centric,  $\text{Tl}_3\text{AsSe}_4$  is not expected to exhibit piezoelectric or second order nonlinear optical behavior. Oriented samples are being prepared for refractive index and acousto-optic measurements.

## 6.3 $\text{Tl}_3\text{AsS}_3$

As indicated in preceding sections, considerable difficulty has been experienced in growing single crystal  $\text{Tl}_3\text{AsS}_3$ , because of the closeness of eutectics to  $\text{Tl}_3\text{AsS}_3$  in the Tl-As-S system. A small section of  $\text{Tl}_3\text{AsS}_3$  boule TASS-BR-5, a  $1.07\text{ cm}$  thick section about  $0.5\text{ cm}$  long near the seed end, as shown in Fig. 23, exhibited reasonable transmission at  $2.1\text{ }\mu\text{m}$ . A  $3.82\text{ mm}$  thick piece of this section was used for optical transmission measurements, with the results shown in Fig. 24. We see that the band edge of  $\text{Tl}_3\text{AsS}_3$  is at about  $0.9\text{ }\mu\text{m}$ , with transmission extending to  $12.5\text{ }\mu\text{m}$ , although absorption losses of  $0.5$  to  $1.0\text{ cm}^{-1}$  can be expected in the  $10$ - $11\text{ }\mu\text{m}$  region because of two-phonon absorption. Another prominent feature is the band tail extending from  $1\text{ }\mu\text{m}$  to about  $4\text{ }\mu\text{m}$ , possibly a result of scattering or absorption in inclusions of other phases of the Tl-As-S system.



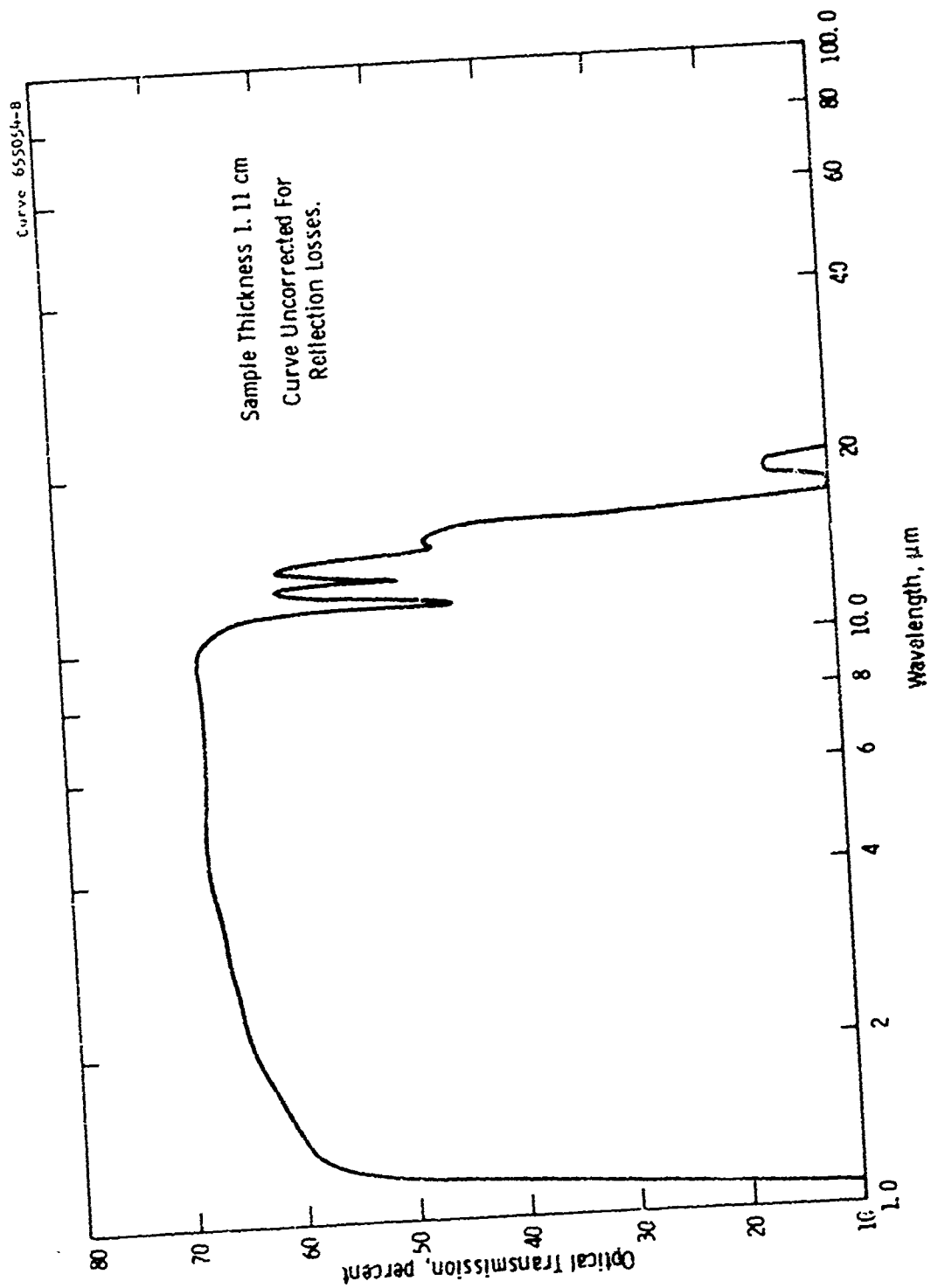


Fig. 22--Optical transmission of  $\text{Tl}_2\text{AsSe}_4$

Curve 653691-8

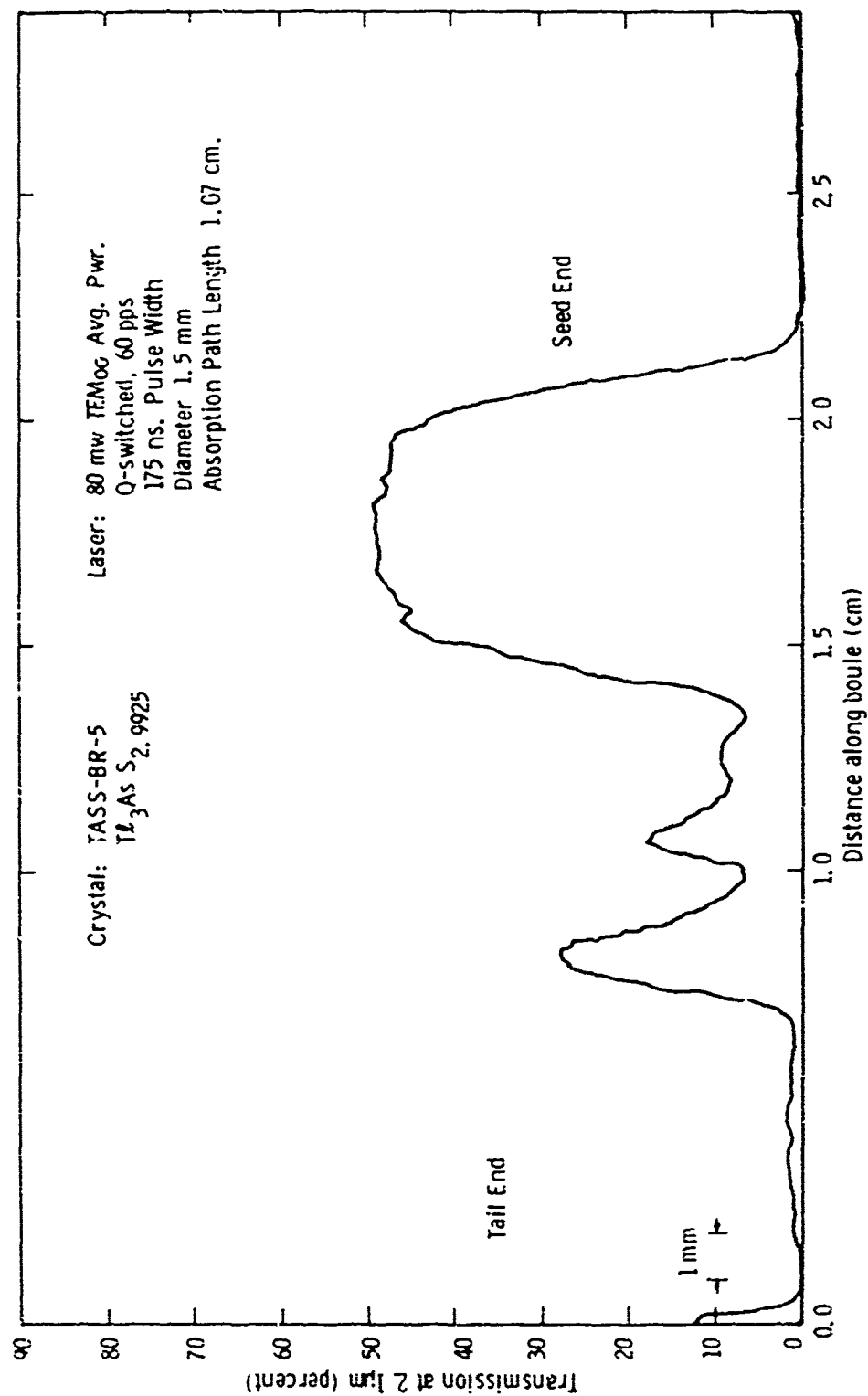


Fig. 23 - Optical transmission at 2.1  $\mu\text{m}$  along an as-grown boule of  $\text{Te}_3\text{AsS}_3$

The position of the band edge at 0.9  $\mu\text{m}$  is a very promising indication for  $\text{Tl}_3\text{AsS}_3$ . It implies the possibility that the refractive indices and hence nonlinear optical coefficient of  $\text{Tl}_3\text{AsS}_3$  lie intermediate between proustite ( $\text{Ag}_3\text{AsS}_3$ ) and  $\text{Tl}_3\text{AsSe}_3$ . For optical frequency up-conversion and mixing experiments, this band edge at 0.9  $\mu\text{m}$  would also allow us access to the region of S-1 photomultiplier sensitivity.

Unfortunately, we were unable to obtain oriented prisms of  $\text{Tl}_3\text{AsS}_3$  from the above "good" section of the boule. Apparently, this section was still polycrystalline, since we could not obtain clear Laue backscatter patterns for x-ray orientation.

#### 6.4 $\text{TlAsS}_2$

We have indicated previously the difficulty in growing single crystal  $\text{TlAsS}_2$  because of its propensity to form a glassy phase. Optical transmission measurements were attempted on some sections of glassy  $\text{TlAsS}_2$ , but the material was opaque in the thicknesses used (2-3 mm).

#### 6.5 $\text{Tl}_3\text{AsS}_4$

The optical transmission of  $\text{Tl}_3\text{AsS}_4$  ranges from about 0.5  $\mu\text{m}$  to 12  $\mu\text{m}$ .<sup>14</sup>

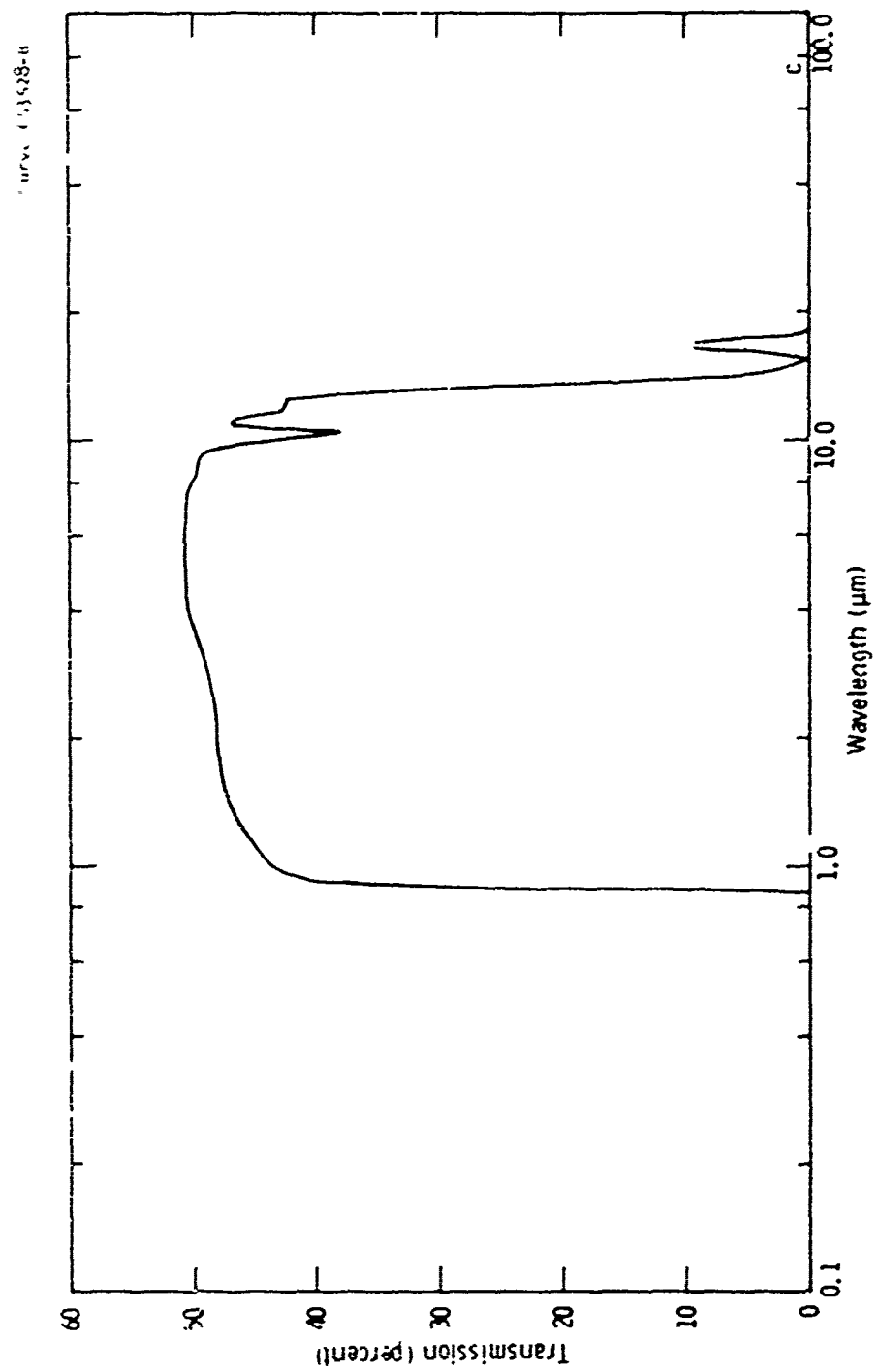


Fig. 24 —Optical transmission vs wavelength for single crystal  $\text{TeAsS}_3$ . Sample thickness 3.82 mm. Curve uncorrected for reflection losses

## 7. PIEZOELECTRIC, ACOUSTIC, AND ACOUSTO-OPTIC PROPERTIES

### 7.1 Tl<sub>3</sub>AsSe<sub>3</sub>

Piezoelectric tests were performed on an oriented sample of Tl<sub>3</sub>AsSe<sub>3</sub> cut from boule TASE-BR-2. The optical quality of this section was not the best; optical losses at 2.1  $\mu$ m were of the order of 0.3 cm<sup>-1</sup>. Silver paste electrodes were placed on a-faces [100] or b-faces [010] and these piezoelectric elements were connected in series with a 100K resistor. A variable frequency RF generator (HP 651A) was connected across the resistor and crystal in series, and variations in RF voltage across the head resistor for constant applied voltage were monitored with an oscilloscope. A frequency counter (GR 1192) was used to measure the crystal resonance and antiresonance frequencies. This technique is not as sensitive as the standard technique (for example, Standard 58 IRE 14.51)<sup>11</sup> which involves the use of an admittance bridge to determine resonance and antiresonance frequencies, but it is sufficiently accurate to provide initial estimates of electromechanical coupling factors.

The electromechanical coupling factor,  $k$ , of a piezoelectric material is a dimensionless factor ranging from zero to one which indicates the efficiency with which mechanical energy is converted into

electrical energy and vice versa.<sup>11</sup> In general,  $k$  depends on mode of vibration and the orientation of the crystal; for an efficient piezoelectric material such as lithium niobate,  $k$  ranges from 0.0 to about 0.7.

For the crystal orientations considered above, the primary modes excited are thickness shear modes, for which the coupling coefficient is  $k_{15}$ . The coupling factor  $k_{15}$  can be determined experimentally by measuring the difference between the frequencies of piezoelectric resonance and antiresonance for an oriented plate or bar driven by an RF field applied to electrodes on the crystal surface.<sup>12</sup> The effective coupling factor is related to the resonance frequency ( $f_r$ ) and antiresonance frequency ( $f_a$ ) of the plate by<sup>13</sup>

$$k_{15}^2 = \left( \frac{\pi}{2} \frac{f_r}{f_a} \right) \cot \left( \frac{\pi}{2} \frac{f_r}{f_a} \right)$$

In Table 5 are given the frequency values as experimentally determined for the strongest modes of an X-cut plate of  $\text{Ti}_3\text{AsSe}_3$ , and the coupling factors and frequency constant,  $N$ , determined from these measurements. The frequency constant  $N$  is defined as the product of series resonant frequency and plate thickness<sup>11</sup>, and is related to an effective elastic modulus,  $\bar{c}$  for the mode, and the crystal density  $\rho$ , by

$$N = f_r t = \frac{F}{2} \sqrt{\frac{\bar{c}}{\rho}}$$

$F$  is a numerical factor related to the eigenvalue of the mode. We can get a numerical value of  $\bar{c}$  from  $N$  and our known value for  $\rho$  ( $= 7.83 \text{ gm/cm}^3$ ).

TABLE 5

Some Piezoelectric and Elastic Constants  
for  $\text{Ti}_3\text{AsSe}_3$  at Room Temperature

Crystal Orientation	$f_r$ (kHz)	$f_a$ (kHz)	$k_{15} = \left[ \frac{1}{2} \frac{f_r}{f_a} \cot \frac{1}{2} \frac{f_r}{f_a} \right] \frac{1}{2}$	$N = f_r t$ (Hz-cm)	$(10^{10} \frac{\text{Nt}}{\text{cm}^2})$
x-cut $\text{Ti}_3\text{AsSe}_3$	148.301	148.718	0.083	524.99	0.216
	154.252	154.565	0.071	546.61	0.234
y-cut $\text{Ti}_3\text{AsSe}_3$	133.609	133.793	0.046	627.83	0.309
$\text{LiNbO}_3$ (typical)			$0 + 0.6$	2000	$1.5 + 25$

The  $Q$ 's ( $\frac{v}{\Delta v}$ ) of the two resonances for the x-cut case were about 300 and 110, respectively.

In comparison with equivalent values for a very efficient piezoelectric such as  $\text{LiNbO}_3$ , the values so far determined for  $\text{Ti}_3\text{AsSe}_3$  indicate that it is not a highly efficient piezoelectric material; if  $\text{Ti}_3\text{AsSe}_3$  is considered for use as an ultrasonic transducer, for instance, we could expect efficiencies of perhaps 5 to 16%, compared to 60% in  $\text{LiNbO}_3$ . The coupling factors for  $\text{Ti}_3\text{AsSe}_3$  are thus of the same order of magnitude as those of quartz.

Acoustic velocity and loss measurements were made on a sample of single crystal  $\text{Ti}_3\text{AsSe}_3$  using conventional pulse-echo techniques, with the results shown in Table 6. Longitudinal wave velocities are of the order of  $2 \times 10^5$  cm/sec, and shear wave velocities are of the order of  $1 \times 10^5$  cm/sec, with a very slight dependence on shear wave polarization.

TABLE 6

Measured Acoustic Properties of  $\text{Ti}_3\text{AsSe}_3$ 

Propagation Direction	Velocities (in cm/sec)		
	Longitudinal	Shear	Shear Polarization
a-Axis[100]	$1.98 \times 10^5$	$1.05 \times 10^5$	b
		$1.05 \times 10^5$	c
b-Axis[010]	$2.13 \times 10^5$	$1.05 \times 10^5$	a
		$1.00 \times 10^5$	c
c-Axis[001]	$2.14 \times 10^5$	$1.01 \times 10^5$	a
		$1.01 \times 10^5$	b

Acoustic losses are fairly low; for longitudinal waves at 30 MHz, the loss is 0.18 db/ $\mu$ sec, while for shear waves at 20 MHz, the loss is 0.057 db/ $\mu$ sec.

Using the measured values of refractive index, density, and acoustic velocities, we may estimate acousto-optic figures of merit for  $\text{Ti}_3\text{AsSe}_3$ . A figure of merit which indicates the efficiency of a material as an acousto-optic modulator is  $M_2 = \frac{n^6 p}{\rho v^3}$ , where  $n$  is the refractive index,  $p$  the photoelastic coefficient,  $\rho$  the density, and  $v$  the acoustic velocity. In Table 7, we compare estimated and measured values for the  $M_2$ 's of  $\text{Ti}_3\text{AsSe}_3$  relative to those of  $\text{SiO}_2$ , at 3.39  $\mu$ m. We assume for the theoretical estimates that the photoelastic coefficients,  $p$ , in the two materials are equal, so that



TABLE 7  
Calculated and Measured Acousto-Optic Figures of Merit,  $M_2$

Material	Long Waves Down c-axis				Shear Waves Down c-axis			
	n(3.39 μm)	v(cm/sec)	M <sub>2</sub> (calc.)	M <sub>2</sub> (meas.)	n(3.39 μm)	v(cm/sec)	M <sub>2</sub> (calc.)	M <sub>2</sub> (meas)
Tl <sub>3</sub> AsSe <sub>3</sub> (ρ = 7.83 gm/cm <sup>3</sup> )	3.24	2.14 x 10 <sup>5</sup>	871	150	3.24	1.01 x 10 <sup>5</sup>	8300	510
	1.41	5.9 x 10 <sup>5</sup>	1	1	1.41	5.9 x 10 <sup>5</sup>	1	1
Te <sub>2</sub> S <sub>2</sub> (ρ = 2.202 gm/cm <sup>3</sup> )								

$$\frac{M_2(Tl_3AsSe_3)}{M_2(SiO_2)} = \frac{n_{Tl_3AsSe_3}^6}{n_{SiO_2}^6} \cdot \frac{(\rho v^3)_{SiO_2}}{(\rho v^3)_{Tl_3AsSe_3}}$$

The ratio by which the measured values of the above  $M_2$ 's depart from the theoretical values is in itself a determination of the relative values of the corresponding photoelastic coefficients; thus,

$$\frac{p_{23}(Tl_3AsSe_3)}{p_{31}(SiO_2)} = \sqrt{\frac{150}{871}} = 0.41 ;$$

$$\frac{p_{44}(Tl_3AsSe_3)}{p_{31}(SiO_2)} = \sqrt{\frac{510}{3300}} = 0.25 .$$

The  $M_2$  value of 510 measured for shear waves is very high. Of presently available infrared materials, only Germanium ( $M_2 = 540$ ),  $As_2S_3$  glass ( $M_2 = 200-300$ ) and  $Tl_3AsS_4$  ( $M_2 = 338$ ) are as efficient as acousto-optic modulators.

## 7.2 $Tl_3AsS_3$

Tests run on an unoriented 3.62 mm thick plate of  $Tl_3AsS_3$  indicated strong resonances at 161 kHz and 168 kHz. This corresponds to sound velocities of about  $1.2 \times 10^5$  cm/sec, which is typical for shear waves in sulfosalt materials. Coupling factors were not measured at the time.

This indication of piezoelectric behavior also implies that the structure of  $\text{Tl}_3\text{AsS}_3$  is acentric, and hence it possesses non-zero second order optical nonlinear susceptibilities. As indicated previously, crystal growth problems have prevented us from obtaining an oriented single crystal section of  $\text{Tl}_3\text{AsS}_3$  for refractive index and nonlinear optical measurements.

### 7.3 $\text{Tl}_3\text{AsS}_4$

Acoustic velocities and acousto-optic figures of merit for  $\text{Tl}_3\text{AsS}_4$  have been reported previously in the literature.<sup>14</sup> Longitudinal mode velocities are of the order of  $2.2 \times 10^5$  cm/sec, and shear mode velocities are about  $1.2 \times 10^5$  cm/sec. Acousto-optic figures of merit,  $M_2$ , range from 166 to 295 at 3.39  $\mu\text{m}$ .

## 8. USEFULNESS OF Tl-As-S-Se COMPOUNDS IN OPTICAL AND ACOUSTO-OPTICAL DEVICES

### 8.1 Introduction

Conclusions are drawn in this section relative to the usefulness of the compounds studied during this contract for optical and acousto-optical devices. Two main types of device application are treated --

- optical parametric oscillation
- acousto-optical applications.

### 8.2 Optical Parametric Oscillation

#### 8.2.1 Desirability of a 2 $\mu$ m-Pumped Optical Parametric Oscillator System

At present, tunable coherent optical sources in the 3 to 5  $\mu$ m spectral region are limited in number, and their output powers and efficiencies are very low. With the frequency-doubled Nd:YAG laser-pumped OPO operating with LiNbO<sub>3</sub> as the nonlinear material,<sup>15</sup> the 3.0 - 3.5  $\mu$ m spectral range can be covered, with average power output of about 5 to 10 mW, and output pulse peak powers of the order of 80 to 150 watts. The ultimate efficiency of this system is limited; the pump wavelength is 0.532  $\mu$ m, so that the best overall conversion efficiency to 4  $\mu$ m to be expected for a singly resonant system is

$$\eta = \frac{\lambda_p}{\lambda_s} = \frac{0.532}{4} = 13\%, \text{ because the idler output at } 1.063 \mu\text{m is not}$$

in the 3 to 5  $\mu\text{m}$  region. Operation of this system at wavelengths longer than 3.5  $\mu\text{m}$  is impossible because of the onset of intrinsic absorption in  $\text{LiNbO}_3$  in that spectral region. In a dye laser mixing experiment in which a ruby laser-pumped dye laser and the ruby laser itself were mixed in a  $\text{LiIO}_3$  crystal, Meltzer and Goldberg<sup>16</sup> generated outputs tunable through the 4.1 to 5.2  $\mu\text{m}$  region, with peak powers of the order of 100 W. The efficiency of this system is very low because of the low inherent efficiency of both the ruby and dye lasers. Goldberg<sup>17</sup> has also attained tunable outputs in the 3.8 to 4.2  $\mu\text{m}$  region in a singly resonant OPO on  $\text{LiIO}_3$ , using a Nd:YAG laser at 1.06  $\mu\text{m}$  as the pump. In that system, however, the output at 4  $\mu\text{m}$  was erratic because  $\text{LiIO}_3$  is lossy at 4  $\mu\text{m}$ , and pump pulse energies high enough to cause thermal defocusing and damage in the  $\text{LiIO}_3$  crystal were required. Most recently, Hanna and his colleagues at the University of Southampton in England have successfully operated an OPO tunable laser from 1.22 to 8.5  $\mu\text{m}$ , using proustite ( $\text{Ag}_3\text{AsS}_3$ ) as the nonlinear crystal, pumped at 1.06  $\mu\text{m}$  by a Nd:YAG laser.<sup>18</sup> Peak powers of about 100 W were obtained in a bandwidth of about  $1\text{ cm}^{-1}$  at 4.5  $\mu\text{m}$ . In this oscillator, the ultimate attainable conversion efficiency would be  $\eta \approx 1.06/4.0 \approx 2\%$ , provided it is operated in a singly resonant configuration. The threshold power density is quoted by Hanna et al. as about  $5\text{ MW/cm}^2$ ; this seems to be unusually low, even though they experienced a round-trip signal loss of only 20% and used a very short optical cavity. This power density, if correct, is well below the reported damage threshold for  $\text{Ag}_3\text{AsS}_3$ , which is about  $20\text{ MW/cm}^2$  at 1.06  $\mu\text{m}$ .

The threshold power densities observed by Hanna et al. at 1.06  $\mu\text{m}$  in  $\text{Ag}_3\text{AsS}_3$  can immediately be used to show that attempts to develop a proustite ( $\text{Ag}_3\text{AsS}_3$ ) oscillator at 2.1  $\mu\text{m}$  would not be very successful. For confocal focusing, the parametric gain coefficient is inversely proportional to the cube of the pump wavelength:  $\Gamma^2 \propto 1/\lambda_p^3$ . Thus, the gain would be  $(2.1 \mu\text{m}/1.06 \mu\text{m})^3 = 7.7$  times lower in the 2.1  $\mu\text{m}$ -pumped system, bringing the required threshold at 2.1  $\mu\text{m}$  above the damage threshold of 20  $\text{MW}/\text{cm}^2$ . The existing evidence thus indicates that a 2.1  $\mu\text{m}$ -pumped OPO based on  $\text{Ag}_3\text{AsS}_3$  would operate only erratically and be severely limited by optical damage problems. A nonlinear optical materials with higher nonlinear susceptibility and higher damage threshold than proustite is thus needed for a 2.1  $\mu\text{m}$ -pumped oscillator. In a subsequent section, we will discuss the applicability of the higher susceptibility nonlinear optical materials available, including  $\text{Tl}_3\text{AsSe}_3$ .

Other techniques for attaining tunable outputs in the 3 to 5  $\mu\text{m}$  region may include various pump-tuned parametric oscillators or the mixing in an infrared nonlinear crystal of an infrared pump with the tuned output of an infrared OPO,<sup>19</sup> and dye laser mixing in proustite.<sup>20</sup> While such systems are still relatively inefficient, mixing efficiencies in some cases can be good.

## 8.2.2 Comparison of Materials for 2 $\mu\text{m}$ -Pumped OPO Action: Advantages of $\text{Tl}_3\text{AsSe}_3$

### 8.2.2.1 Requirements

Nonlinear optical materials for parametric oscillator applications must meet many requirements, among which are:

- A. Transparency throughout a wavelength region including pump, signal, and idler wavelengths.
- B. Reasonably high nonlinear optical susceptibilities.
- C. Capability of being phase-matched for the wavelength range of parametric operation desired.
- D. Optical damage thresholds higher than the power densities needed for efficient parametric conversion.
- E. Availability as reasonably large single crystals of good optical quality.

A convenient method of comparing nonlinear materials on the basis of requirements A and B above was discussed by Harris,<sup>21</sup> who noted that in a parametric oscillator the conversion efficiency is proportional to a certain combination of materials parameters,  $d^2/n^3$ , where  $d$  is the effective nonlinear optical susceptibility of the materials for the particular parametric process, and  $n$  is roughly an average refractive index. Strictly speaking,  $d$  may vary considerably even for the same material, depending on the process considered and the wavelength regions involved; nevertheless, the "figure of merit"  $d^2/n^3$  gives a rough comparison of the effectiveness of various materials in parametric processes. Harris plotted  $d^2/n^3$  for materials versus their useful transparency region, as shown in Fig. 25. We have added to Harris' figure the parameters for some recently developed materials, and included some recent corrections to previously measured susceptibilities. If we concentrate first on materials with a 2 to 5  $\mu\text{m}$  region of transparency, we see that of those materials listed, this

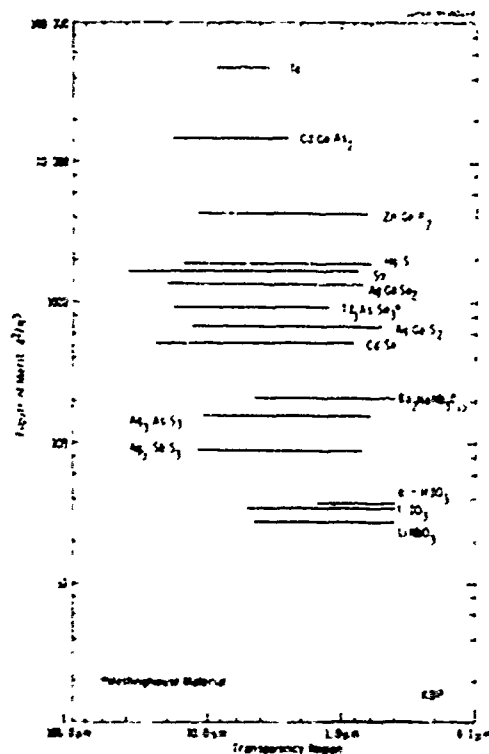


Fig. 25 — Optical parametric figure of merit,  $d^2/n^3$ , and transparency region for nonlinear optical materials.

transparency requirement eliminates KDP,  $\text{LiNbO}_3$ ,  $\alpha\text{-HIO}_3$ ,  $\text{Ba}_2\text{NaNb}_5\text{O}_{15}$ ,  $\text{CdGeAs}_2$  and Te.  $\text{LiNbO}_3$  and  $\text{Ba}_2\text{NaNb}_5\text{O}_{15}$  actually are transparent to about  $5\text{ }\mu\text{m}$ ; however, they are too lossy in the region above  $4.5\text{ }\mu\text{m}$  to be considered for parametric applications in the entire  $4\text{ to }5\text{ }\mu\text{m}$  region. In addition,  $\text{LiNbO}_3$  of normal composition cannot be phase matched for a  $2.1\text{ }\mu\text{m}$  Ho:YAG pumped oscillator; the  $d$ -coefficients of these two materials are also considerably lower than those of some of the other materials.



Of the remaining materials, we see that the chalcopyrites  $\text{ZnGeP}_2$  and  $\text{AgGaS}_2$  appear to have reasonably large figures of merit, although we have calculated the figure of merit for  $\text{AgGaS}_2$  on the basis of the initially reported measurement<sup>22</sup> of  $d(\text{AgGaS}_2) \approx 0.42 d(\text{GaAs})$ , which later evidence indicates might be too high by a factor of three.<sup>23</sup> We will see below that  $\text{ZnGeP}_2$  is not phase matchable over the entire 4 to 5  $\mu\text{m}$  region for 2.1  $\mu\text{m}$  pumping, while  $\text{AgGaS}_2$  is phase matchable for that process.

Recent work by Boyd and his colleagues<sup>24</sup> indicated that the chalcopyrite  $\text{AgGaSe}_2$  has considerable promise as a nonlinear optical material. It should allow phase-matched 2.1  $\mu\text{m} \rightarrow 4.1 \mu\text{m}$  conversion at about  $48^\circ$  to the optic axis,<sup>24</sup> and has a high figure of merit (See Fig. 28). As is the case with many of the chalcopyrites,  $\text{AgGaSe}_2$  is difficult to grow in useful crystal sizes of good optical quality. Boyd et al. reported losses of the order of  $4$  to  $5 \text{ cm}^{-1}$  over the entire transparency range of the crystal.<sup>23</sup> Recently, we have been able to grow  $\text{AgGaSe}_2$  as reasonably large ( $0.04 \times 0.4 \times 0.6 \text{ cm}$ ) single crystals of lower loss ( $\alpha \approx 0.5 \text{ cm}^{-1}$  at 2.1  $\mu\text{m}$ ). This loss is still too high for use in a parametric oscillator.

$\text{HgS}$  and  $\text{Se}$  have attractively high figures of merit; we have calculated phase matching conditions for  $\text{HgS}$  (positive uniaxial, Type II phase matching) and find that it does not phase match for 2  $\mu\text{m}$ -pumped degenerate oscillator operation ( $\lambda_p = 2 \mu\text{m} \rightarrow \lambda_s = \lambda_1 = 4 \mu\text{m}$ ) at any angle. Although we have not calculated phase matching conditions for  $\text{Se}$ , it is positive birefringent and the birefringence ( $\sim 0.81$ )

appears to be too large to allow phase matching in the 2 to 5  $\mu\text{m}$  region. Se and HgS have also been extremely hard to grow as usable size crystals of good optical quality.

CdSe is an attractive material from the point of view of the nonlinear figure of merit  $d^2/n^3$ , and availability in crystals of good quality and size; unfortunately, as we shall see, it does not phase match properly for 2.1  $\mu\text{m}$ -pumped oscillation in the 4 to 5  $\mu\text{m}$  region, although it has been useful for oscillation in the 2.0 to 2.3  $\mu\text{m}$  and 9 to 13  $\mu\text{m}$  regions when pumped with a 1.833  $\mu\text{m}$  source.<sup>25</sup>

The sulfosalt materials  $\text{Ti}_3\text{AsSe}_3$ ,  $\text{Ag}_3\text{AsS}_3$ , and  $\text{Ag}_3\text{SbS}_3$  all appear to be phase matchable, as we will see below.  $\text{Ti}_3\text{AsSe}_3$  has the highest figure of merit and should provide the lowest threshold of all of the materials considered in this discussion.

$\text{LiIO}_3$  is also phase matchable for the 2.1  $\mu\text{m}$  pumped parametric oscillator process, and its transparency region extends to 5  $\mu\text{m}$ , although there is a small absorption band for the ordinary ray near 4.2  $\mu\text{m}$  which could cause some difficulty. The fact that the nonlinear susceptibility of  $\text{LiIO}_3$  is much lower than the above materials means that very high pump power densities will be required to reach the oscillator threshold if  $\text{LiIO}_3$  is used.

Details of the phase matching considerations are given in Section 8.2.2.2; in Section 8.2.2.3 we will summarize all of the materials considerations.

#### 8.2.2.2 Phase Matching Considerations

##### (i) Chalcopyrites

$\text{ZnGeP}_2$  is very attractive from the point of view of its transparency and high nonlinear optical figure of merit, but unfortunately the refractive index data of Boyd<sup>26</sup> indicate that a 2.1  $\mu\text{m}$  pump cannot be phase-matched efficiently to parametrically generate radiation anywhere between 3.4  $\mu\text{m}$  and 5.8  $\mu\text{m}$ , although the 2.1 to 3.4  $\mu\text{m}$  and 5.8 to 12  $\mu\text{m}$  regions should be accessible with a 2.1  $\mu\text{m}$  pump (Fig. 26). In addition to this problem, the state of the art in growing  $\text{ZnGeP}_2$  is not very satisfactory; for some as yet unknown reason, the band edge extends into the 2  $\mu\text{m}$  region, producing unacceptable loss (as high as a few  $\text{cm}^{-1}$ ) for the pump radiation.<sup>26</sup>

$\text{AgGaS}_2$ , according to recent measurements of Boyd et al.,<sup>23</sup> is phase matchable (Type I,  $0 + 0 \rightarrow e$ ) for 2.1  $\mu\text{m}$  pumped oscillation into the 4 to 5  $\mu\text{m}$  region, at about  $30.5^\circ$  to the optic axis (Fig. 27). Unfortunately,  $\text{AgGaS}_2$  in its present state of development also exhibits large losses ( $\approx 1.0 \text{ cm}^{-1}$ ) at 2.1  $\mu\text{m}$  and about  $1 \text{ cm}^{-1}$  in the 4 to 5  $\mu\text{m}$  region. The losses are partly due to absorption and partly due to scattering in cracks and voids in the material.

$\text{AgGaSe}_2$  should be phase matchable for 2.1  $\mu\text{m} \rightarrow 4.1 \mu\text{m}$  frequency conversion, as we may see from Figs. 28 and 29, which are reproduced from the paper of Boyd et al. on ternary selenides.<sup>24</sup>

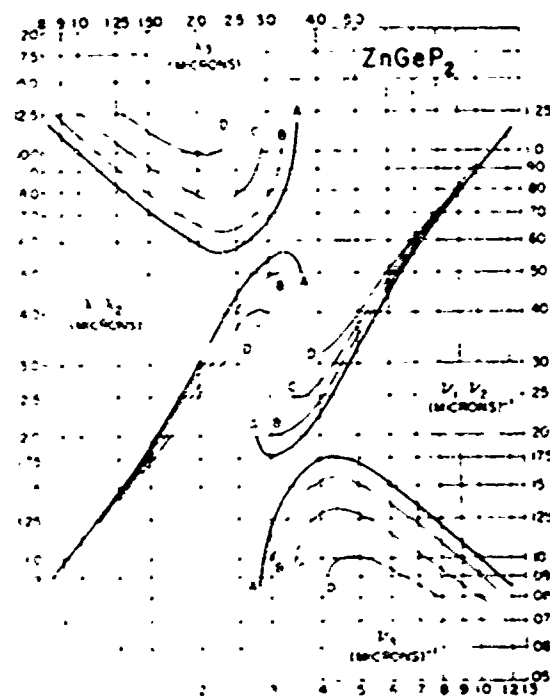


Figure 26 -- Three-frequency phase matching for ZnGeP<sub>2</sub> indicating  $v_1$  and  $v_2$  (or wavelength  $\lambda_1$  and  $\lambda_2$ ) vs the pump frequency  $v_3$  (or wavelength  $\lambda_3$ ). (Ref. 26).

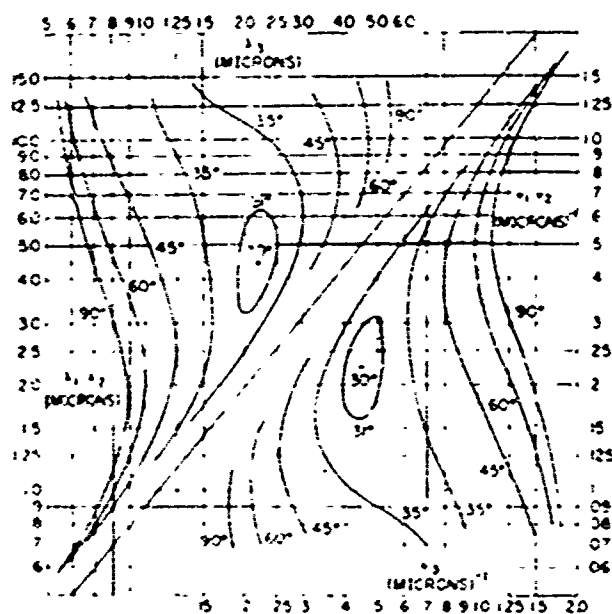


Figure 27 -- Type-1 (o + o - e) three-frequency phase matching for AgGaS<sub>2</sub>, indicating  $v_1$  and  $\lambda_2$  versus pump frequency  $v_3$  (lower right) or  $\lambda_1$  and  $\lambda_2$  versus  $\lambda_3$  (upper left). (Ref. 23).

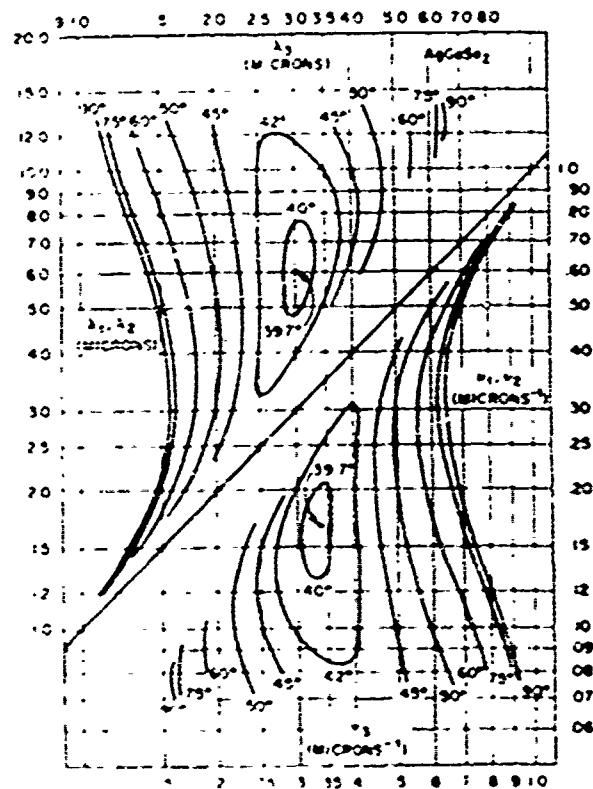


Figure 28 -- Type-1 (o + o + e) three-frequency phase matching for  $\text{AgGaSe}_2$ , indicating  $\nu_1$  and  $\nu_2$  versus pump frequency  $\nu_3$  (lower right) or  $\lambda_1$  and  $\lambda_2$  versus  $\lambda_3$  (upper left). (Ref. 24).

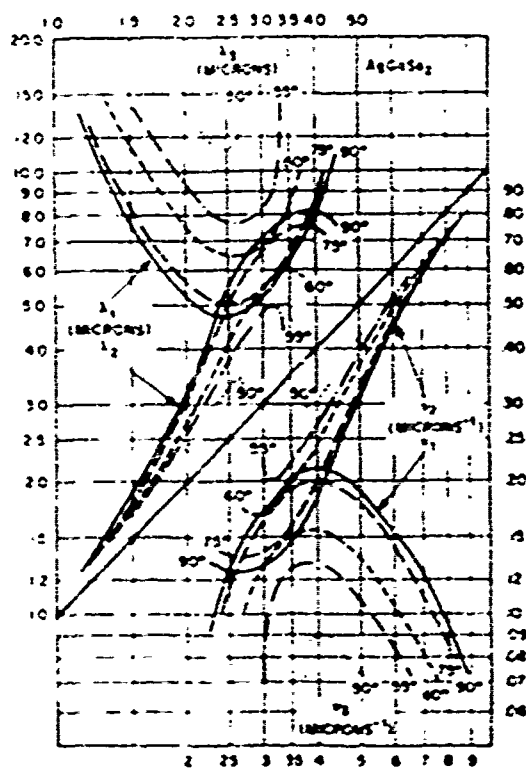


Figure 29 — Type-2 ( $e + o + o$ ) three-frequency phase matching for AgGaSe<sub>2</sub>, indicating  $\nu_1$  and  $\nu_2$  versus pump frequency  $\nu_3$  (lower right) or  $\nu_1$  and  $\nu_2$  versus  $\nu_3$  (upper left). (Ref. 24).

(ii) CdSe

A phase matching curve for CdSe pumped at 2.06  $\mu\text{m}$  is shown in Fig. 30.<sup>27</sup> The curve was calculated with pumping by Ho:SOAP ( $\lambda_p = 2.06 \mu\text{m}$ ) in mind, but the general features will not be much different for Ho:YAG pumping ( $\lambda_p = 2.098 \mu\text{m}$ ). The 3.1 to 6.4  $\mu\text{m}$  region is completely inaccessible for phase-matched parametric conversion. An interesting feature is that 90 deg phase matching of conversion of 2.1  $\mu\text{m}$  radiation to 3.05  $\mu\text{m}$  and 6.40  $\mu\text{m}$  radiation should be possible, which implies very low thresholds for this process. Also note that large angle phase matching for conversion and continuous tuning in the 2.5 to 3.0  $\mu\text{m}$  and 6.4 to 13  $\mu\text{m}$  regions is possible in CdSe pumped at 2  $\mu\text{m}$ . Since  $n_e - n_o > 0$  (positive birefringence), Type II ( $e \rightarrow o + e$ ) phase matching is required.

Byer and Herbst<sup>25</sup> have made use of these excellent properties of CdSe by constructing a tunable CdSe oscillator with outputs in the 2.2 to 2.3  $\mu\text{m}$  and 9 to 13  $\mu\text{m}$  region.

(iii) The Sulfosalt Materials

Figures 31 and 21 show phase matching curves for proustite<sup>27</sup> ( $\text{Ag}_3\text{AsS}_3$ ) and thallium arsenic selenide<sup>27</sup> ( $\text{Tl}_3\text{AsSe}_3$ ). We have not calculated curves for  $\text{Ag}_3\text{SbS}_3$  but we expect them to be somewhat like those of  $\text{Ag}_3\text{AsS}_3$  (the refractive index data indicate that phase-matched degenerate operation with  $\lambda_p = 2.1 \mu\text{m}$  will occur in  $\text{Ag}_3\text{SbS}_3$  at an angle of about 27 deg to the crystal c-axis).<sup>28</sup>

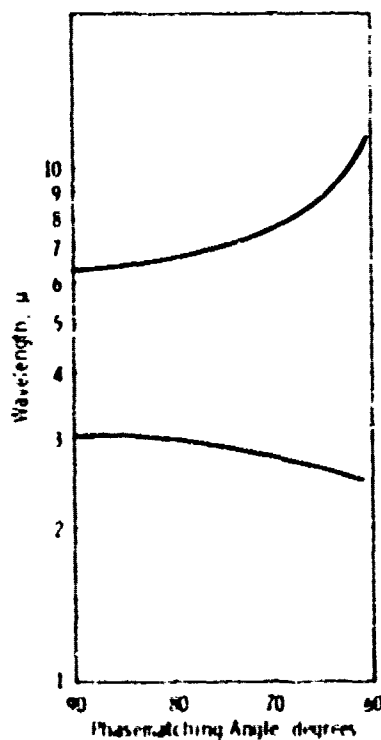


Figure 30 -- Theoretical tuning curve for optical parametric oscillation in CdSe, for a pump wavelength  $\lambda_p = 2.06 \mu\text{m}$ . (Ref. 27)

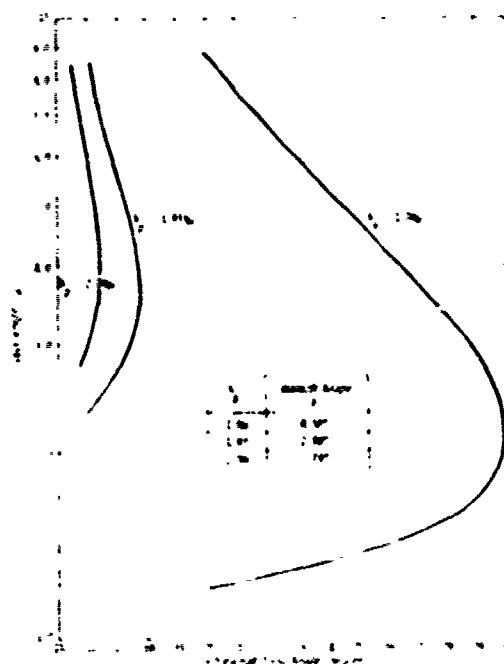


Figure 31 -- Theoretical tuning curves for optical parametric oscillation in proustite ( $\text{Ag}_3\text{AsS}_3$ ), pump wavelength  $\lambda_p$  a parameter. (Ref. 27).



Figure 31 illustrates that phase-matched tunable oscillation for a 2.1  $\mu\text{m}$  pump in  $\text{Ag}_3\text{AsS}_3$  will occur at phase match angles of 16.5 to 15.5 deg; the steepness of the curve also indicates that the tuning with angle will be very rapid. The birefringence angle  $\phi$ , which limits the effective length of the crystal for a given beam spot size, is 2.89 deg at 2.1  $\mu\text{m}$ .

Phase matching curves for  $\text{Tl}_3\text{AsSe}_3$  (Fig. 21) indicate that phase matching should occur for 2.1  $\mu\text{m}$  pumping at angles of 30 to 24 deg. The birefringence angle,  $\phi$ , is about the same as for  $\text{Ag}_3\text{AsS}_3$ . Again, the steepness of the tuning curve for 2.1  $\mu\text{m}$  pumping implies that rapid tuning with angular displacement will be possible. However, this also implies that a large oscillator bandwidth will result.

#### (iv) $\text{LiIO}_3$

Figure 32 shows tuning curves<sup>27</sup> calculated for  $\text{LiIO}_3$ .  $\text{LiIO}_3$  is matchable for a 2.1  $\mu\text{m}$  pumped oscillator, but the idler wavelength comes close to the absorption edge; this may present problems in the 4.5 to 5.0  $\mu\text{m}$  region. The tuning curve is also very steep, as was the case for  $\text{Tl}_3\text{AsSe}_3$  and  $\text{Ag}_3\text{AsS}_3$ . The birefringence angle  $\phi$  is also larger for  $\text{LiIO}_3$  than for  $\text{Tl}_3\text{AsSe}_3$ , 3.74 deg as against 2.98 deg. The parametric gain is roughly proportional to  $1/c^2$  for a wide range of focusing conditions, thus the parametric gain in  $\text{Tl}_3\text{AsSe}_3$  will be over 50% greater than in  $\text{LiIO}_3$  due to this factor alone. An even greater advantage of  $\text{Tl}_3\text{AsSe}_3$  over  $\text{LiIO}_3$  is the fact that the nonlinear optical coefficient,  $d$ , of  $\text{Tl}_3\text{AsSe}_3$  is about seven times larger than that of

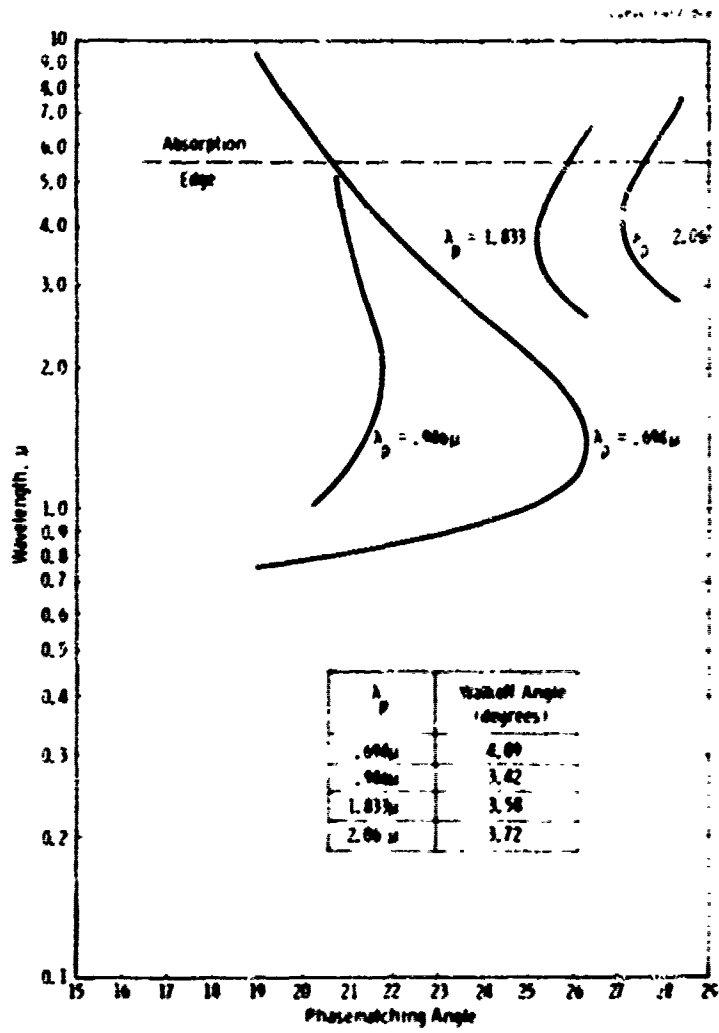


Figure 32 -- Theoretical tuning curves for optical parametric oscillation in  $\text{LiIO}_3$ , pump wavelength  $\lambda_p$  a parameter (Ref. 27).

Table 3 -- Properties of Candidate Nonlinear Optical Materials for  
2.1  $\mu$ m Pumped Parametric Oscillation in the 4 to 5  $\mu$ m Region

Material	Phase Matchable for 2.1 $\mu$ m - 4-5 $\mu$ m?	Relative OPO Figure of Merit $d^2/n^3$ (KDP=1)	Single Crystal Sizes Available (cm)	Optical Damage Threshold
LiNbO <sub>3</sub>	No Also lossy at 4.5 $\mu$ m	28	2 x 2 x 10	40 MW/cm <sup>2</sup> (Long Pulse) 100 MW/cm <sup>2</sup> (ns Pulse)
LiIO <sub>3</sub>	Yes	35	5 x 5 x 10	125 MW/cm <sup>2</sup>
Ag <sub>3</sub> AsS <sub>3</sub>	Yes	160	1 x 1 x 5	12-40 MW/cm <sup>2</sup> ?
Ag <sub>3</sub> ShS <sub>3</sub>	Yes	170	1 x 1 x 5	14-30 MW/cm <sup>2</sup>
Ba <sub>2</sub> NbNb <sub>5</sub> O <sub>15</sub>	? Lossy at 4.5 $\mu$ m	210	0.5 x 0.5 x 0.5	1 MW/cm <sup>2</sup>
CdSe	No	520	1 x 1 x 5	60 MW/cm <sup>2</sup>
AgGaS <sub>2</sub>	Yes	680* (-70?)	0.3 x 0.3 x 0.3	12-26 MW/cm <sup>2</sup>
Tl <sub>3</sub> AsSe <sub>3</sub> **	Yes	930	0.8 x 0.8 x 2	32 MW/cm <sup>2</sup>
Se	? (Probably Not)	1700	0.2 x 0.2 x 1	?
HgS	No	1900	0.2 x 0.2 x 1	?
ZnInP <sub>2</sub>	No	4300	0.3 x 0.3 x 0.3	>3 MW/cm <sup>2</sup>
AgGaSe <sub>2</sub>	Yes	1350	0.4 x 0.4 x 0.6	>10 MW/cm <sup>2</sup>

\* Assumes  $d(\text{AgGaS}_2) = 0.42 d(\text{GaAs})$ , which may be a factor of 3 too high.

\*\* Westinghouse material.

$\text{LiIO}_3$ ; the data of Fig. 32 imply that the gain per unit pump power in  $\text{Ti}_3\text{AsSe}_3$  should be at least 30 times higher than that in a sample of  $\text{LiIO}_3$  of the same length, not even including the  $1/\rho^2$  factor above.

#### 8.2.2.3 Summary of Survey Results

Table 8 summarizes the results of the preceding surveys, including only those materials exhibiting reasonable transparency throughout the entire 2 to 5  $\mu\text{m}$  region. The summary shows that, of the phase matchable materials,  $\text{Ti}_3\text{AsSe}_3$  and  $\text{AgGaSe}_2$  possess by far the largest figures of merit. Of these two potentially useful materials, only  $\text{Ti}_3\text{AsSe}_3$  is available as good quality single crystals of large size. Its most serious rival is probably  $\text{LiIO}_3$ , which is a factor of 30 worse in figure of merit, but better by the same factor of 30 from point of view of damage threshold;  $\text{LiIO}_3$ , however, may also be somewhat lossy near 5  $\mu\text{m}$ , which would degrade oscillator performance.

### 8.3 Acousto-Optic Devices

#### 8.3.1 Acousto-Optic Modulators

The high acousto-optic figure of merit and relatively low optical and acoustic losses observed in  $\text{Ti-As-S,Se}$  compounds all indicate that these materials should be very useful as low-drive power acousto-optic modulators and beam scanners for infrared sources. In the following, we calculate some acoustic drive power requirements and other system characteristics for such applications.

##### 8.3.1.1 External Modulation at 1.06 $\mu\text{m}$

The fraction  $I/I_0$  of incident light intensity  $I_0$  which is deflected by a grating generated by an acoustic wave is given by<sup>28</sup>

$$\frac{I}{I_0} = \sin^2 \frac{\Delta\phi}{2}, \quad (1)$$

where  $\Delta\phi$  is the amplitude of the grating, and is related to the applied acoustic power  $P_{AC}$  by

$$\Delta\phi = \pi \sqrt{\frac{2}{\lambda} \frac{L}{H} M_2 P_{AC}}. \quad (2)$$

Here,  $L/H$  is the ratio of the acoustic beam length to its height, and is usually close to unity. The figure of merit, as we have previously noted, is

$$M_2 = \frac{n^3 p}{\rho v^3},$$

where  $n$  is the refractive index at the vacuum wavelength of the incident optical beam,  $p$  is the relevant photoelastic coefficient,  $\rho$  the density, and  $v$  the sound velocity in the material. For fused  $\text{SiO}_2$ ,  $M_2 = 1.51 \times 10^{-18} \text{ sec}^3/\text{gm}$ .

For the case of external modulation of a 1.06  $\mu\text{m}$  beam, we may use the above results to calculate the acoustic drive power requirement. We consider the requirement for deflecting all of the incident power out of the beam, i.e., 100% modulation. Then,

$$\begin{aligned} \frac{\Delta\phi}{2} &= \frac{\pi}{2} \\ P_{AC} &= \frac{\lambda^2}{2M_2} \frac{H}{L}, \quad \text{or} \\ P_{AC} &= \frac{\lambda^2}{2M_2} \quad \text{for } H = L, \text{ which is the usual case.} \end{aligned} \quad (3)$$

With the value of  $M_2$  for fused  $\text{SiO}_2$  given above, Eq. (3) yields a drive power requirement of 372 watts. External modulation at 100% at  $1.06 \mu\text{m}$  using  $\text{SiO}_2$  is therefore out of the question. With  $\text{Ti}_3\text{AsS}_4$  as the modulator material, however, the drive power requirement will be reduced from this by a factor of 200 to 300, since the figure of merit of  $\text{Ti}_3\text{AsS}_4$  is this much larger than that of  $\text{SiO}_2$  near  $1 \mu\text{m}$ .<sup>29</sup> The required acoustic drive power with  $\text{Ti}_3\text{AsS}_4$  will thus be only about 1 to 2 watts, depending on which photoelastic coefficient is used; such acoustic powers are readily generated in sulfosalt crystals by conventional techniques. For modulation at wavelengths longer than about  $1.3 \mu\text{m}$ , interaction with shear waves in  $\text{Ti}_3\text{AsSe}_3$  becomes the configuration of choice, since the figure of merit  $M_2$  is, as seen in Sec. 7.1, about 500, which is even larger than that of  $\text{Ti}_3\text{AsS}_4$ . Germanium, another competitor, does not transmit below  $2 \mu\text{m}$ .

#### 8.3.1.2 Internal Modulation and Q-Switching at $1.06 \mu\text{m}$

For Q-switching, the considerations are the same as those above, except that the amount of light deflected by the modulator now only needs to equal the amount by which single-pass gain in the laser rod exceeds its threshold value. For a typical Nd:YAG system operating with up to a few watts output, the gain per single pass ranges from 5% to 15%. Let us assume that the modulator must deflect about 10% of the incident light. Again, from Eqs. (1) and (2), we find, for the required acoustic power to Q-switch a Nd:YAG laser.

$$P_{AC} = 15.5 \text{ watts for } \text{SiO}_2$$

$$P_{AC} = 0.05 \text{ to } 0.08 \text{ watts for } \text{Ti}_3\text{AsS}_4.$$

Taking into account the coupling efficiencies of the acoustic transducers which would be needed, a  $\text{LiNbO}_3$  transducer should provide coupling efficiencies ranging from 20% to 50%, depending on the mode desired. A reasonable estimate for the range of total power required from the RF generator to provide high data rate Q-switching would be 100 milliwatts to 400 milliwatts, if  $\text{Ti}_3\text{AsS}_4$  were used as the modulator material. Since the acoustic loss in  $\text{Ti}_3\text{AsS}_4$  is only about 1 dB/ $\mu$ sec at 400 MHz, Q-switched pulse data rates of at least 500 MB/sec should be readily attainable with less than 0.5 watts average of RF drive power. Mode-locking of a continuous Nd:YAG laser will also be possible using this technique; even lower RF drive powers will be needed for that application, because when the modulation frequency is set close to the laser cavity longitudinal mode frequency interval, a much smaller loss perturbation than 100% is sufficient to cause mode locking.

Similarly, modulation of the laser with an internal  $\text{Ti}_3\text{AsS}_4$  acousto-optic modulator would require much less power than the 1 to 2 watts calculated above for external modulation.

### 8.3.2 Electronically Tunable Infrared Acousto-Optic Filters

For crystals of the triclinic and monoclinic systems, as well as for those in point groups 4,  $\bar{4}$ , 4/m, 3,  $\bar{3}$ , 3c,  $\bar{3}m$  and 6,  $\bar{6}$ , 6/m, an acoustic wave traveling collinearly with a light wave can diffract a portion of the light from its original polarization into an orthogonal

polarization. This scattering process is cumulative along the path of the beams in the crystal only provided that the acoustic frequency is adjusted so that the magnitude of the acoustic wave vector,  $|\hat{k}_a|$ , equals the magnitude of the difference between the wave vectors corresponding to the optical e-ray and o-ray, i.e.,

$$|\hat{k}_a| = |\hat{k}_e - \hat{k}_o|.$$

There is thus a one-to-one correspondence between the frequency of the light which experiences this cumulative polarization rotation and the frequency of the applied acoustic wave. This effect was used successfully by Harris and his co-workers to construct electronically tunable narrow band filters using  $\text{LiNbO}_3$ <sup>30</sup> and  $\text{CaMoO}_4$ .<sup>31</sup>

It can be shown<sup>32</sup> that the acoustic power density  $P_A/A$  required to obtain theoretical 100% peak transmittance of a filter of length  $L$  is given by

$$\frac{P_A}{A} = \frac{c^3 v^3}{3 n_o^3 n_e^3 P_{1j}^2} \cdot \frac{\lambda_o^2}{2L^2} = \frac{\lambda_o^2}{2M_2 L^2}, \quad (4)$$

where  $\lambda_o$  is the optical wavelength at the peak of the filter transmission, and  $M_2 = \frac{6P^2}{3c^3 v^3}$  is the acousto-optic figure of merit which we have discussed previously. The important things to note in Eq. (4) are that the required acoustic power density increases rapidly, as the square of the optical wavelength, and that this required power density decreases as the material acousto-optic figure of merit increases.

With presently available acousto-optic materials such as  $\text{PbMoO}_4$ ,<sup>33</sup>  $\text{CaMoO}_4$  and  $\text{LiNbO}_3$ , the use of such filters is restricted to wavelengths



shorter than about  $3 \mu\text{m}$  by two materials problems; the first is the fact that these oxides transmit only out to about  $4.5 \mu\text{m}$ , and the second is the fact that their acousto-optic figures of merit are still so small that enormously high acoustic power densities are required at the longer wavelength. As an example, let us consider comparing  $\text{Ti}_3\text{AsSe}_3$  and one of these new oxide materials,  $\text{CaMoO}_4$ , in this application, assuming we wish to achieve tuning in the  $3\text{-}5 \mu\text{m}$  region.  $\text{CaMoO}_4$  exhibits considerable absorption loss in the region  $4\text{-}5 \mu\text{m}$ , while  $\text{Ti}_3\text{AsSe}_3$  losses are only about  $0.02 \text{ cm}^{-1}$  in this region, but the power density requirement is even a more severe limitation for  $\text{CaMoO}_4$ , as we will see. The figure of merit  $M_2$  of  $\text{CaMoO}_4$  is  $M_2 = 33.3 \times 10^{-18} \text{ sec}^3/\text{gm}$ . Assuming that we have  $2 \text{ cm}$  long crystals, Eq. (4) above yields for the required acoustic power densities for 100% transmission at a peak wavelength of  $4 \mu\text{m}$ ,

$$\frac{P}{A} (\text{CaMoO}_4) = 660 \text{ watts/cm}^2 ; \text{ for } \text{Ti}_3\text{AsSe}_3 \text{ we find}$$

$$\frac{P}{A} (\text{Ti}_3\text{AsSe}_3) = 8.8 \text{ watts/cm}^2 . \text{ This assumes}$$

$$M_2(\text{Ti}_3\text{AsSe}_3) = 150 M_2(\text{SiO}_2) \text{ as in Table 6.}$$

The  $\text{Ti}_3\text{AsSe}_3$  collinear acousto-optic filter at  $4 \mu\text{m}$  would thus require seventy times lower power density than the  $\text{CaMoO}_4$  filter at  $4 \mu\text{m}$ . Using the theory first worked out by Harris, one can show that this  $2 \text{ cm}$  long  $\text{Ti}_3\text{AsSe}_3$  filter would have an acceptance angle of about 200 milliradians, a bandwidth of about  $40 \text{ \AA}$ , and would require an acoustic drive frequency of about 100 MHz at  $4 \mu\text{m}$ . Acoustic losses at 100 MHz in

$\text{Ti}_3\text{AsSe}_3$  are equal to or less than 0.5 dB/ $\mu\text{sec}$  for longitudinal waves, which would be used for this filter configuration. Since the velocity of longitudinal waves is about  $2 \times 10^5$  cm/sec, the total acoustic loss down the 2 cm long filter will be only about 5 dB, which should be quite tolerable.

$\text{Ti}_3\text{AsSe}_3$  is thus a very attractive candidate as a material for use in infrared tunable acousto-optic filters.

Materials which do not belong to the proper point group to be used as collinear acousto-optic filters can nevertheless be used in a "noncollinear" filter configuration,<sup>34</sup> with somewhat greater restrictions on the acceptance angle. The high acousto-optic figures of merit of  $\text{Ti}_3\text{AsS}_2$  and other new and promising sulfosalt single crystals such as  $\text{Ti}_3\text{PSe}_4$  and  $\text{Ti}_3\text{AsSe}_4$  will make them very useful in such noncollinear acousto-optic filter applications, even though they do not possess the proper symmetry to be used in the collinear configuration.

## 9. CONCLUSIONS

Two important conclusions have been reached on the basis of work performed during this program. These are as follows.

1. Phase diagram studies are essential to understand observed features of the crystal growth of complicated ternary compounds such as the Tl-As-S-Se compounds investigated during this contract. We have demonstrated that dramatically improved crystal quality results from systematic phase diagram studies conducted within the context of crystal growth.

2. The ternary compounds in Tl-As-S and Tl-As-Se chemical systems represent a class of compounds that show considerable potential as single-crystal materials for optical and acousto-optical devices. The work performed during this contract represents an essential foundation for future studies of these materials in devices.

#### REFERENCES

1. G. W. Roland and R. G. Seidensticker, "A Coprecipitation Mechanism to Explain  $\text{Ag}_7\text{AsS}_6$  Inclusions in Proustite ( $\text{Ag}_3\text{AsS}_3$ ) Crystals," *J. Crystal Growth*, 10:213 (1971).
2. W. Nowacki, "Zur Classifikation und Kristallchemie der Sulfosalz," *Schweiz. Min. u. Pet. Mitt.*, Band 49, Heft 1:109 (1969).
3. M. Hansen and K. Anderko, "Constitution of Binary Alloys," McGraw Hill Book Company, 1305 pp. (1958).
4. R. P. Elliott, "Constitution of Binary Alloys, First Supplement," McGraw Hill Book Company, 877 pp. (1965).
5. F. A. Shunk, "Constitution of Binary Alloys, Second Supplement," McGraw Hill Book Company, New York, 720 pp. (1969).
6. C. Palache, H. Berman and C. Frondel, "Dana's System of Mineralogy, Seventh Edition," Vol. I, John Wiley and Sons, Inc., New York, 834 pp (1944).
7. J. J. Skinner, F. D. Luce and E. Makovicky, "Studies of the Sulfosalts of Copper III. Phases and Phase Relations in the System Cu-Sb-S," *Econ. Geol.* 67:924 (1972).
8. G. Canneri and L. Fernandes, *Atti reale accad. Lincei, Sez. I*, 1, 674 (1925).

9. S. A. Dembovskii, V. V. Kirilenko and S. A. Khvorostenko, "The  $\text{As}_2\text{Se}_3\text{-Tl}_2\text{Se}$  System," Russian Journal of Inorganic Chemistry 14:1346 (1969).
10. J. D. Feichtner and G. W. Roland, "Optical Properties of a New Nonlinear Optical Material:  $\text{Tl}_3\text{AsSe}_3$ ," Appl. Opt. 11, 993 (1972).
11. IRE Standards on Piezoelectric Crystals, 1958 Proc. IRE 46, 764 (1958).
12. W. G. Cady, "Piezoelectricity," Dover Publications, New York, 1964.
13. A. W. Warner, M. Onoe, and G. A. Coquin, "Determination of Elastic and Piezoelectric Constants for Crystals in Class (3m)," J. Acoust. Soc. Am. 42, 1223 (1967).
14. G. W. Roland, M. Gottlieb, and J. D. Feichtner, "Opto-Acoustic Properties of Thallium Arsenic Sulphide,  $\text{Tl}_3\text{AsS}_4$ ," Appl. Phys. Lett. 21, 52 (1972).
15. Model 1020 Optical Parametric Oscillator, Chromatix Corp., Mountain View, California 94040.
16. D. W. Meltzer and L. S. Goldberg, "Tunable IR Difference Frequency Generation in  $\text{LiIO}_3$ ," Optics Communications, 5:209 (1972).
17. L. S. Goldberg, "Optical Parametric Oscillation in Lithium Iodate," Appl. Phys. Lett. 17:489 (1970).
18. D. C. Hanna, B. Luther-Davies, and R. C. Smith, "Singly Resonant Proustite Parametric Oscillator Tuned from 1.22 to 8.5  $\mu\text{m}$ ," Appl. Phys. Lett., 22:440 (1973).

19. C. D. Decker and F. R. Tittel, "High Power Broadly Tunable Difference Frequency Generation in Proustite," Appl. Phys. Lett. 22:411 (1973).
20. R. L. Byer, "Optical Parametric Oscillators," Stanford University, Microwave Lab. Report 2140 (January 1973).
21. S. E. Harris, "Tunable Optical Parametric Oscillators," Proc. IEEE, 57:2096 (1969).
22. D. S. Chemla, P. J. Dupecek, D. S. Robertson, and R. C. Smith, "Silver Thiogallate, A New Material with Potential for Infrared Devices", Optics Communications, 3:29 (1971).
23. G. D. Boyd, H. Kasper, and J. H. McFee, "Linear and Nonlinear Optical Properties of  $\text{AgGaS}_2$ ,  $\text{CuGaS}_2$ , and  $\text{CuInS}_2$ , and Theory of the Wedge Technique for the Measurement of Nonlinear Coefficients," IEEE J. of Quantum Electronics, QE7:563 (1971).
24. G. D. Boyd, H. M. Kasper, J. H. McFee and F. G. Storz, "Linear and Nonlinear Optical Properties of Some Ternary Selenides," IEEE J. of Quantum Electronics, QE-8:900 (1972).
25. R. L. Herbst and R. L. Byer, "CdSe Infrared Parametric Oscillator," Appl. Phys. Lett., 21:189 (1972).
26. G. D. Boyd, E. Buehler, and F. G. Storz, "Linear and Nonlinear Optical Properties of  $\text{ZnGeP}_2$  and CdSe," Appl. Phys. Lett., 18:301 (1971).
27. R. L. Byer, Stanford University (Private Communication).

28. D. A. Pinnow, "Guidelines for the Selection of Acousto-Optic Materials," IEEE J. of Quant. Electron. QE-6, 223 (1970).
29. G. W. Roland, M. Gottlieb, and J. D. Feichtner, "Optoacoustic Properties of Thallium Arsenic Sulphide,  $Tl_3AsS_4$ ," Appl. Phys. Lett. 21, 52 (1972).
30. S. E. Harris, S. T. K. Nieh, and D. K. Winslow, "Electronically Tunable Acousto-Optic Filter," Appl. Phys. Lett. 15, 325 (1969).
31. S. E. Harris, S. T. K. Nieh, and R. S. Feigeison, " $CaMoO_4$  Electronically Tunable Optical Filter," Appl. Phys. Lett. 17, 223 (1970).
32. S. E. Harris and R. W. Wallace, "Acousto-Optic Tunable Filter," J. Opt. Soc. Am. 59, 744 (1968).
33. D. A. Pinnow, L. G. Van Uitert, A. W. Warner, and W. A. Bonner, "Lead Molybdate: A Melt-Grown Crystal with a High Figure of Merit for Acousto-Optic Device Applications," Appl. Phys. Lett. 15, 83 (1969).
34. I. C. Chang, "Noncollinear Acousto-Optic Filters," Paper 7.4, 1973 IEEE Conference on Laser Engineering and Applications, Washington, DC, May 30-June 1, 1973.